Title
Multiferroics for Future Cell Sorting Devices

Author
Kundu, Auni Aunnoyee

Publication Date
2019

Peer reviewed|Thesis/dissertation

UNIVERSITY OF CALIFORNIA

Los Angeles

Multiferroics for Future Cell Sorting Devices

A dissertation submitted in partial satisfaction of the

requirements for the degree Doctor of Philosophy

in Mechanical Engineering

by

Auni Aunnoyee Kundu

2019

ABSTRACT OF THE DISSERTATION

Multiferroics for Future Cell Sorting Devices

by

Auni Aunnoyee Kundu

Doctor of Philosophy in Mechanical Engineering

University of California, Los Angeles, 2019

Professor Gregory P. Carman, Co-Chair

Professor Christopher S. Lynch, Co-Chair

The development of cell sorting technologies in the late 1960s has allowed for enhanced diagnostic tools advancing the field of biotechnology. Among the various sorting mechanisms, magnetic cell sorting is desirable for its rapid analysis capabilities and compatibility with biological samples. However, the use of a permanent magnet required for magnetic sorting mechanisms presents a challenge when scaling these devices to the nanoscale. In this work, the prospective of strain-mediated multiferroic composite structures for use in magnetic cell sorting is presented. In a multiferroic composite structure, a ferromagnetic material is layered on top of a ferroelectric substrate. By applying a voltage to the ferroelectric substrate, the substrate generates an in-plane strain. Through mechanical coupling of the two layers, the magnetization of the ferromagnetic material is rotated. As a result, magnetization can be changed without the use of a

permanent magnet allowing for scalable control of magnetism. Key concepts are discussed for the successful implementation of strain-mediated multiferroic cell sorting devices. First, a new device is simulated and demonstrated to be capable of 360^{o} magnetization rotation of an elliptical magnetic element using a simple voltage pulse. This design is an improvement over the currently available structures capable of similar magnetization dynamics. Next, the limitations of a dynamic voltage input in a multiferroic composite structure are discussed. This work offers new information about how successful performance of cell sorting devices may be impeded due to changing input voltage and fabricated defects in the structure. Additionally, a new finite element model is developed to better incorporate the material behavior of the ferroelectric substrate and its corresponding effects on magnetization in a single domain ferromagnetic material. The results of these studies are a stepping stone towards better understanding the discrepancies between the existing models of strain-mediated multiferroic structures and experimental observations of these fabricated devices. The last contribution of this work is understanding how magnetic beads used in cell sorting applications might respond to the force generated by the magnetic field in strain-mediated structures. This work lays the groundwork for better understanding the design of future strain-mediated multiferroic cell sorting devices.

The dissertation of Auni Aunnoyee Kundu is approved.

Dino Di Carlo

Robert N. Candler

Dennis W. Hong

Gregory P. Carman, Committee Co-Chair

Christopher S. Lynch, Committee Co-Chair

University of California, Los Angeles

2019

To my parents and sister, your love

and support made this possible.

Table of Contents

List of Figures

List of Tables

ACKNOWLEDGEMENTS

This work has been accomplished with the support and encouragement of many inspiring people. Professor Lynch, thank you for always allowing me to explore topics I was interested in and encouraging me to think critically about innovate solutions. I am so fortunate to have an adviser who is easy to converse with and understanding of the challenges in life outside of work. Professor Carman, thank you for giving me the opportunity to participate in a collaborative research environment. Being a part of the TANMS family has been one of the most rewarding aspects of my time at UCLA. I would also like to thank the members of my committee, Professors Rob Candler and Dino Di Carlo for their enthusiasm for the 3D Thrust and willingness to review my work; and Professor Hong, thank you for always finding solutions to problems that may arise throughout the PhD journey.

To my lab family, Andres, Tony and Devin, you three have made every day in lab an absolute joy! I could write a dissertation about each of you and it would not be enough to recount all the memories and laughs we have shared over the years. Andres and Tony, you two have been next to me since day one and I could not be more fortunate to have entered this program with such brilliant and fun-loving guys. Andres, our midnight runs, cupcake adventures, museum visits and city exploring have allowed me to maintain a proper research and life balance, as much balance as I am capable of at least. Thanks for being my adventure buddy throughout this journey and for always making me feel like I have family here in LA. Thanks for being the Winnie to my piglet and staying awake to keep me company! Tony, from spending nights laughing on the floor until we cried, watching Top Gear videos to introducing me to all the “must see” movies even though I fell asleep, thanks for always teaching me to take breaks in life and not stress so much. You have always been there for me and supported me through some of the toughest nights in grad

school. You have taught me to be a stronger individual and for that I cannot thank you enough. Despite the distance these last few months, I know you are always just a phone call away no matter how far apart we are. I cannot imagine being in this position without your help and words of encouragement. Devin (aka Ron Swanson), I am so glad my first impression of you did not deter me from spending more time with you. You are one of the kindest individuals I have ever met. Our food adventures and animal shelter trips have consisted of some of my best memories in LA. Your childlike sense of humor has always kept me laughing, and snorting, throughout the years and I cannot imagine how different lab would be if you were not here with me. Thank you for being an exceptional friend and putting up with me when I doubted myself. Words will never truly express how grateful I am to you three for being pillars of support during my time in this program.

To all lab friends, past and present, thank you for making lab a fun place to work and for teaching me the qualities of a good researcher. Yu-Ching, you are the most genuine person I have ever met. You are not afraid to be yourself and stand up for what you believe in. I am so fortunate to have you in my life as you are one of the friendliest people I have ever met. Thank you for being such a supportive friend throughout my time as a grad student. Chris, you are a great friend and mentor and I can always turn to you when I need help. You have helped me navigate the tough waters of grad school and I know I can turn to you for help in the real world. Li and QC, you both are extraordinary individuals, such brilliant scientists but so humble and kind, I am really happy our paths crossed in grad school. Jizhai, Peng, Chuck, and Chen Cai thank you for making time to answer all the research questions I had and never getting frustrated. To Keller and Kyle, thank you for being my technical support team when “COMSOL was being COMSOL”. Paul, thanks for always being so friendly and easy to talk to; your easy-going nature

and willingness to take people on food adventures made adjusting to life in LA so easy. To John D., thanks for always being the professor of the group and offering to help explain any physics or engineering topic, and for keeping the pen! Scott, thanks for being safety officer in lab. To John N., thank you for always being willing to participate in lab outings even as the new member in lab. Paymon, thank you for always keeping me company and being the most optimistic person in lab. To members of the TANMS Family, Jackie, Maggie, Reem, Kevin and Sidhant, thank you for the insightful research discussions through the years and all the laughs at the annual review and meetings. I have been so fortunate working with such incredible people who make work an exciting part of each day.

To my friends outside of lab, thank you for being a breath of fresh air from multiferroics. Kelly, I am so lucky to have a friend like you! From painting murals, happy hour, acapella nights and our shared love of all desserts, my life in LA was more colorful with your presence. I am thankful for your friendship and our shared inner grandma tendencies. Despite the distance, your words have continued to encourage me throughout the last years in the program. To Taylor, my stalker since kindergarten, you are a true gem! It has been so comforting to have a familiar face in LA. From Vegas, Disneyland, the awful singing, and Santana on repeat, every moment with you has been filled with laughter. Thanks for being a friend I could turn to whenever grad school and life would get too overwhelming. Carlos, you are such a great friend! Thank you for letting me be your sous chef when you worked magic in the kitchen. From the movie nights, Disneyland, Kygo, to the puzzles and music videos, you have always been a relaxing presence in my life. Josh, despite not hearing me during the orientation in first year, I am glad you finally took out your headphones to talk to me in our second year. You are always willing to help others even if it inconveniences you, making you one of the nicest people I have ever met. Thanks for always

demonstrating your robots whenever I needed help for my outreach events. I am glad we managed to get our coffee breaks to vent and destress from the work. Alex, despite our busy schedules, I am glad we have managed to find time for quick lunch and coffee breaks, you are such a supportive and encouraging friend. I am lucky to know such kind, intelligent and high-spirited individuals who have been an integral part of making life at UCLA so enjoyable.

My time at UCLA was not limited to just my peers, but also the supportive staff in the department and TANMS. Angie, you have made every obstacle in grad school more approachable by knowing exactly who I could talk to. Thank you for always having your door open and being willing to help me solve any problem. To Tsai-Tsai, thank you for always being supportive during my early days in TANMS and throughout my entire graduate career. Pilar, your enthusiasm to help diverse students find joy in STEM fields is admirable and has added to my experiences of being a graduate student mentor. Michelle, our lunch and coffee breaks have been wonderful to chat about the center. Your smiling face has always been a welcome sight when attending the many weekly meetings of the center. It has been a pleasure getting to know such wonderful, supportive and caring women.

Finally, to the group of people who had no choice but to deal with me throughout this journey, my family, thank you for everything. Baba, your passion for your work and enthusiasm for engineering first sparked my interest in the field in high school. Through the years, whenever I would struggle with a problem, you taught me to never give up, that if you try and are willing to learn, you can achieve anything. I am always appreciative of your wise words during times of stress and the support you have provided through the many years of being your pacha. Mommy, thank you for all the sacrifices you have made through the years. As hard as the PhD has felt at times, it is nothing compared to the tough job of being a mother. You have constantly taught me

to be a better person and have never failed in making all aspects of life easier for me. You have the biggest heart and are a role model for the type of woman I strive to be every day. I am so blessed to have such wonderful, energetic and weird parents, I made it through this program because of your constant love and support and will never be able to properly thank you both enough for all you have done.

To Ina, there is no one who understands the journey over the last few years better than you. Having gone through a PhD program yourself, you were always there to provide helpful advice when I needed it, when you were not sick that is. Watching you overcome so many obstacles and refusing to let anything stop you from achieving your goals has made you the strong, independent and driven woman you are today. I am so lucky to have a sister who, I not only look up to, but also have fun with by practicing our ridiculous dance moves and sharing baby goat (or sheep?) pictures. Rishon, thank you for taking care of Ina through the years, it was comforting to know she had someone looking after her when my parents and I were across the country. Although you are a man of few words, you always manage to crack a joke at the perfect moment, constantly making us laugh. I am so thrilled you and Alex joined that family and have cherished having brothers I have always wanted when I was growing up.

And finally, to Gary, thank you for making the last few months of the program so much less stressful, yes, this was the less stressed version of me. Thank you for always reassuring me that everything will be okay despite how many times I said, “You don’t know that.” From walking 0.09 miles, roller coasters, breaking rules, and lunar eclipses, you have brought non-stop laughter into my world. As this chapter of my life comes to an end, I am looking forward to the next chapter where we spend many adventures together full of laughter, coffee and dark chocolates.

Thank you for being the perfect ying to my yang. I am so lucky to be walking into the real world with you, and your vest, by my side.

VITA

Education

2016 M.S., Mechanical Engineering

University of California, Los Angeles, CA, USA

2014 B.S., Mechanical Engineering

University of Arizona, Tucson, AZ, USA

Employment History

2014-2019 Graduate Student Researcher and Teaching Assistant

University of California, Los Angeles, CA, USA

SELECTED PUBLICATIONS AND CONFERENCE PRESENTATIONS

Hsiao, Y., […], Kundu, A, et al. (2019). Capturing Magnetic Bead-based Arrays Using Perpendicular Magnetic Anisotropy (PMA). *Applied Physics Letters*. Under Review.

Kundu, A., et al. (2019). Combined Ferroelectric and Micromagnetics Finite Element Model for Strain-Mediated Multiferroic Single Domain Element. Manuscript under preparation.

Kundu, A., et al. (2019). Modeling the Effects of Ferroelectric Domain Wall Motion on Magnetic Nano-Islands in Strain-Mediated Heterostructures. Oral presentation at Joint MMM-Intermag Conference, Washington, D.C. USA.

Kundu, A. A., et al. (2018). 360° deterministic magnetization rotation in a three-ellipse magnetoelectric heterostructure. *Journal of Applied Physics, 123*(10), 104105.

Chavez, A. C., Kundu, A. A., Lynch, et al. (2018, March). Modeling the effects of strain profiles and defects on precessional magnetic switching in multiferroic heterostructures. In *Behavior and Mechanics of Multifunctional Materials and Composites XII* (Vol. 10596, p. 1059622). International Society for Optics and Photonics.

Kundu, A., et al. (2017). 360° deterministic magnetization rotation in a three-ellipse magnetoelectric heterostructure. Poster presented at the MMM Conference, Pittsburgh, PA USA.

Kundu, A., et al. (2016). Deterministic magnetization control of single domain magnetic elements in multiferroic heterostructures. Poster presented at the Joint MMM – Intermag Conference, San Diego, CA USA.

I. Introduction

1.1 Motivation

Since the first cell sorter was introduced in 1960's by Leonard Herzenberg, it has changed the field of modern medicine[1]. Claimed to be one of the "most important medical devices ever developed[2]," cell sorting technologies have advanced the fields of immunology, stem cell research and provided valuable insights for the treatment of HIV/AIDS and cancer among other infectious diseases[2]–[5]. Cell sorting has been an important tool for diagnostics and monitoring of diseases in both research and academia[6]. Furthermore, cell sorting technologies have led to better understanding of cell and protein engineering to further the knowledge of the functionalities of the human body[7]. Among the variety of sorting techniques -- including fluorescent[5], [8]–[10], and acoustic methods[11]–[14] -- magnetic bead based cell sorting is attractive due to the simplified processing steps which allows for rapid analysis and diagnosis[6].

In current magnetic cell sorting systems, a large permanent magnet is used to produce magnetic forces on superparamagnetic (SPM) beads tagged to cells traveling through a channel. Miltenyi et al.[15] first introduced Magnetic Activated Cell Separation (MACS) using a large external field and a steel wool column. Cells labeled with a magnetic beads were trapped in the steel wool in the presence of the field while unmarked cells filtered through separating the different cell groups. This separation technique has since been widely applied to microchip devices where tagged cells are separated from untagged cells using an external magnet and a microfluidic channel[16]–[18]. More complex systems have been demonstrated to sort various cells by using different sized beads which would produce different capture forces in the presence of an external permanent magnet[19], [20].

The advantage of using a permanent magnet is that the gradient of the magnetic field produced is higher than that typically produced by a coil, resulting in larger forces with the ability to strongly trap SPM beads [21]. Two disadvantages remain with this method of cell sorting: 1) the ability to locally control cells tagged with SPM beads is limited, which makes imaging of cells a challenge and 2) the use of the external permanent magnets to trap cells means there is not a path to scalability of magnetic sorting techniques to the nanoscale. Local control of beads at the nano to micron scale implies that each tagged cell could be controlled individually in a channel and the cells would not aggregate together in the channel. This single cell analysis is preferred for small volume, detailed analysis of a cell sample[21]–[28]. Scalability of magnetic sorting devices remains a challenge since generating magnetic fields at the nanoscale requires the use of a current-carrying wire. However, as the wire reduces in the diameter, more losses due to heat (ohmic losses) are expected, reducing the overall device efficiency. To create the next generation of magnetic cell sorting and transportation of cells, novel methods to switch magnetism at the small scale are being explored.

Multiferroic materials provide a pathway towards magnetization control without the use of any electric current[29]. Multiferroic materials are materials which display two or more ferroic orders (ferroelectric, ferromagnetic or ferroelastic). The coupling of these order parameters can result in the magnetoelectric (ME) effect. The ME effect produces a change in the electrical response of a material (polarization) due to an applied magnetic field. The converse ME effect also exists and is represented by a change in magnetization of a material due to an applied electric field. In 1961 Astrov[30] experimentally demonstrated the existence of the magnetoelectric effect in a chromium oxide generating an interest in the research and applications of multiferroic materials. There are two common classes of multiferroic materials: 1) single-phase multiferroic materials and 2) multiferroic composites[31]. Extensive work has been done to study the behavior of single-phase

multiferroic materials [32]–[37]. The ME effect in single phase materials is only observed at very low temperatures[32]–[37] and therefore not practical for use in most device applications. Multiferroic composites however offer an alternative approach for the ME effect at room temperature with higher ME response[38].

In multiferroic composite structures the ME effect results from layering a magnetostrictive material with a piezoelectric material[31]. A magnetostrictive material will strain, undergo a shape change, in response to a magnetic field. Analogously, a ferroelectric material will accumulate electric charge, causing a change in polarization, in the presence of an applied stress[39]. The direct and converse ME effect in composite structures is described by Eqs. 1.1 and 1.2[31]:

$$ME_H\ effect = \frac{magnetic}{mechanical} \times \frac{mechanical}{electric} \tag{1.1}$$

$$ME_E\ effect = \frac{electric}{mechanical} \times \frac{mechanical}{magnetic} \tag{1.2}$$

The ME effect can result from a magnetic field applied to the magnetostrictive layer causing a strain which results in a change of polarization in the ferroelectric material. Additionally, it can arise from an applied electric field on the ferroelectric material causing strain changes in the magnetostrictive material. In both scenarios, the coupling effect is a result of strain transfer at the interface of the materials leading to the name strain-mediated multiferroic heterostructure.

The field of composite multiferroic structures had its start in the 1970s when van Suchtelen suggested the existence of elastic coupling between two phases of different properties[38]. Experimental demonstration by the Phillips Laboratory suggested strong ME coupling coefficients existed in Barium Titanate and Cobalt Iron Oxide ($BaTiO_3$ – $CoFe_2O_4$) ceramic composites which were almost a hundred times larger than single-phase multiferroic materials[38], [40]–[43].

Stronger ME coupling coefficients were theoretically predicted using the Green's Function approach suggesting a Giant Magnetoelectric Effect (GME) in composite structures was possible and useful for magnetic sensors and other applications[44]–[46]. GME was first experimentally demonstrated by Ryu et al.[47]–[49] in a Terfenol-D/Lead Zirconate Titanate (PZT) laminate and also by Mori and Wuttig in a Terfenol-D/Polyvinylidene Fluoride (PVDF) laminate[50]. Further work was done to study this GME interaction with various magnetostrictive and piezoelectric bulk composite structures[51]–[53] and provided the groundwork to develop these structures for nanoscale device applications.

Much of the pioneering work on nanoscale strain-mediated multiferroic composites focused on the magnetization behavior in thin film magnetic materials[54], [55], [64], [56]–[63]. The results of these large magnetization changes in response to an applied voltage, even at the nanoscale, allowed for the exploration of strain-mediated multiferroic composites as potential memory and spintronic devices. Buzzi et al.[65] experimentally demonstrated 90^{o} magnetization rotations of patterned Nickel (Ni) islands on PMN-PT ($PbMg_{1/3}Nb_{2/3}O_3$-$PbTiO_3$) substrates further supporting the possibility of magnetoresistive memory devices. In these devices one magnetic state would represent the bit "1" and the rotated state after application of voltage would indicate the bit "0". Further research to study the switching behavior of different magnetic geometries on ferrooelectric substrates demonstrated one major challenge with these devices was that the substrate clamping of the magnetic material caused a drastic reduction in the strain transfer between the materials. This resulted in lowered magnetization rotations than the thin film counterpart[65]–[67]. A major breakthrough by Cui et al.[66] came with the implementation of patterned electrodes on the ferroelectric substrate to rotate magnetic islands in strain-mediated multiferroic heterostructures.

The experimental efforts by Cui et al.[66] on patterned electrodes were supported by strain-mediated magnetoelectric material models implemented in a finite element code by Liang et al.[68], [69]. Previous simulation attempts had primarily focused on modeling the interactions of magnetostrictive and ferroelectric films[70], [71], [80], [81], [72]–[79], however Liang et al.[69] was the first to study the non-uniform piezoelectric strain response on patterned magnetic Ni islands. This model has been shown to better predict the magnetization dynamics of strain-mediated multiferroic composites than other open source magnetization dynamics software[82], [83]. The promising simulation and experimental results by Liang et al.[68] and Cui et al.[66] paved the way for exploring the possibility of new technologies for multiferroic nanocomposites[84]–[88].

Since multiferroic composite nanostructures have demonstrated efficient performance at the nanoscale in the memory and spintronics communities, Sohn et al.[84] considered the potential for these devices in lab-on-chip technologies. By using patterned Ni rings on a PMN-PT substrate, 360^{o} rotation of a magnetic domain was achieved. The ability to locally control the rotation of magnetic domains without the use of external magnetic fields leads to the potential of strain-mediated multiferroic composites for cell sorting applications. Still some challenges remain with using multiferroic structures with cell sorting. Deterministic magnetization switching is desired for both memory and spintronic devices as well as cell sorting techniques, but limited methods of deterministic switching are available using strain control of magnetization. Additionally, since these devices are designed so that many magnetic elements are patterned on the ferroelectric substrate, it remains a challenge for all magnetic elements to have the same dynamics under the same applied electric field. To use multiferroic nanostructures for the next generation of cell sorting devices, these challenges must be addressed to design better structures.

1.2 Dissertation Overview

In this dissertation, the key challenges of using strain-mediated multiferroic nanostructures for cell sorting applications are addressed through different simulation work. In Chapter 2, the underlying principles of magnetism and ferroelectricity are presented. Additionally, the weak form of the equations used for the finite element model are developed. In Chapter 3, a new design to achieve 360^{o} deterministic switching in magnetic islands is introduced. The advantages of this new switching method is discussed and compared to previous designs. In Chapter 4, some of the limitations of the new proof of concept device is addressed. This chapter explores the potential shortcomings of using some existing voltage actuation methods for strain-mediated devices. In Chapter 5, a new model is developed to address some material challenges that may impede the ideal device performance in an array of magnetic nanostructures on a ferroelectric substrate. This model is developed to try to understand the origin of inhomogeneous magnetization switching of magnetic elements across a ferroelectric substrate. Chapter 6 presents a model that can be used to assess the possible forces that may be involved with capturing magnetic beads in cell sorting applications. A final summary and future outlook for the work in this dissertation is given in Chapter 7.

II. Background

2.1 Magnetic Structure

When children are first introduced to magnets, they learn about the north and south poles of the magnets and how like poles repel each other while opposite poles attract. However, further inspection of a regular refrigerator magnet reveals the complex structure of magnetic materials. A millimeter sized magnet is typically composed of multiple crystalline magnetic grains. In each grain, multiple magnetic domains can be found. A single domain of magnetization is one in which all the magnetization is aligned the same direction, typically along an easy axis of the structure. When a magnetic material is magnetized creating the traditional north and south poles of a magnet, the volume average of the magnetic domains gives a net magnetization. Zones of transition between two different single domains of magnetization are called domain walls and can be found in magnetic multidomain structures. Figure 2.1 represents the approximate length scales associated with bulk, multidomain, and single domain magnetic materials[67]. This dissertation is primarily focused on the magnetization dynamics of single domain magnetic elements within strain-mediated multiferroic structures and will thus focus on magnetic elements below 500 nm.

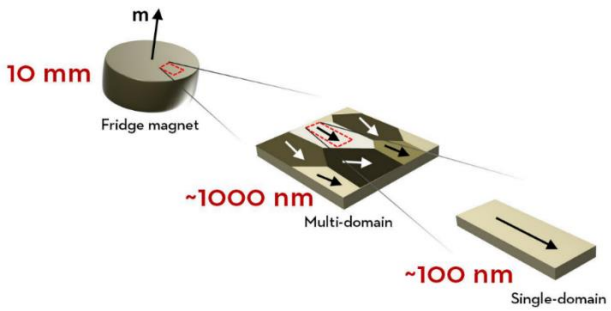

Figure 2.1 Approximate visual representation of the magnetic structure within magnetic materials[67].

2.2 Micromagnetics

The total free energy, E, of a ferromagnetic body under constant temperature and applied field can be written as a function of magnetization of the body, M, and the applied field, H_a[89]:

$$E(M, H_a) = E_{ex} + E_{MCA} + E_{zeeman} + E_{demag} + E_{me} \tag{2.1}$$

The total energy is the sum of the exchange energy(E_{ex}), magnetocrystalline anisotropy energy(E_{MCA}), Zeeman energy(E_{zeeman}), magnetostatic energy(E_{demag}), and the magnetoelastic energy(E_{me}). Details of these energies are presented next.

a. Exchange Energy

The exchange energy arises from two neighboring magnetic spins tending to align themselves in the same direction. This exchange interaction is what produces small uniformly magnetized single domain magnetic regions. This interaction energy is given as by the Heisenberg Hamiltonian as[90]:

$$W = -2J \sum \boldsymbol{S_i} \cdot \boldsymbol{S_j} \tag{2.2}$$

Here, J represents the nearest neighbor exchange integral. And $\boldsymbol{S_i}$ and $\boldsymbol{S_j}$ are neighboring spins. If it is assumed that $\boldsymbol{m_i}$ is the unit vector in the $-S_i$ direction, then $\boldsymbol{S_i} = -S\boldsymbol{m_i}$ where S is just the spin magnitude. Equation 2.2 can be rewritten as:

$$W = -2JS^2 \sum cos\theta_{i,j} \tag{2.3}$$

$\theta_{i,j}$ is the small angle between the spins $\boldsymbol{m_i}$ and $\boldsymbol{m_j}$. Using small angle approximations, the Hamiltonian is rewritten as follows:

$$W = -2JS^2 \sum \left(1 - \frac{1}{2}\theta_{i,j}^2\right) = constant + JS^2 \sum \left(\boldsymbol{m_j} - \boldsymbol{m_i}\right)^2 \tag{2.4}$$

The difference vector $\boldsymbol{m_j} - \boldsymbol{m_i}$ can be written in terms of a continuous function $\boldsymbol{m}$ and the position vector, $\Delta \boldsymbol{r}_j = \boldsymbol{r}_j - \boldsymbol{r}_i$ as indicated below:

$$\boldsymbol{m_j} - \boldsymbol{m_i} = \Delta \boldsymbol{r}_j \cdot \nabla \boldsymbol{m} \tag{2.5}$$

If $\boldsymbol{m} = m_x \boldsymbol{e_x} + m_y \boldsymbol{e_y} + m_z \boldsymbol{e_z}$ then the Hamiltonian can be expanded to Equation 2.6:

$$W = constant + JS^2 \sum \left[\left(\Delta \boldsymbol{r}_j \cdot \nabla m_x\right)^2 + \left(\Delta \boldsymbol{r}_j \cdot \nabla m_y\right)^2 + \left(\Delta \boldsymbol{r}_j \cdot \nabla m_z\right)^2\right] \tag{2.6}$$

Using symmetry properties and multiplying the number of spins per unit volume, n, the energy per unit volume is obtained and given in Equation 2.7.

$$f_{ex} = A\left[(\nabla m_x)^2 + \left(\nabla m_y\right)^2 + (\nabla m_z)^2\right] \tag{2.7}$$

Here, A represents the exchange constant which is dependent on the material of the ferromagnetic body and given by:

$$A = \frac{1}{6} nJS^2 \sum \Delta \boldsymbol{r}_j^2 \tag{2.8}$$

The total exchange energy of the system is found by integrating over the volume, V, of the magnetic material to obtain:

$$E_{ex} = \int A\left[(\nabla m_x)^2 + \left(\nabla m_y\right)^2 + (\nabla m_z)^2\right] dV \tag{2.9}$$

b. Magnetocrystalline Anisotropy Energy

The magnetocrystalline anisotropy energy arises from the preferential (easy) directions of magnetization as a result of the crystal lattice of the magnetic material. The general anisotropy energy density is given as

$$E_{MCA} = \int f_{MCA}(\boldsymbol{m}) dV \tag{2.10}$$

Where $f_{MCA}(\boldsymbol{m})$ is the energy per unit volume. Many magnetic materials are described by two types of magnetocrystalline anisotropies 1) uniaxial anisotropy and 2) cubic anisotropy.

When uniaxial anisotropy exists in a material, there is only one easy axis. In this case, the anisotropy energy depends only on the relative orientation of $\boldsymbol{m}$ to the easy axis. Consider the easy axis along the z-direction, the anisotropy energy can be written as a function of $m_z = \cos\theta$ and expanded such that

$$f_{MCA}(m) = K_0 + K_1 \sin^2\theta + K_2 \sin^4\theta + K_3 \sin^6\theta + \cdots \tag{2.11}$$

Here, K_1, K_2, K_3, ... are the anisotropy constants with units $[J/m^3]$. Truncating the above expression after the $\sin^2\theta$ term can provide some physical insight to the magnetization behavior in response to the magnetocrystalline anisotropy energy. If $K_1 > 0$, the energy is reduced when $\theta = 0$ or $\theta = \pi$. This implies that the energy is minimized when the magnetization lies along the easy axis in a parallel or antiparallel orientation and known as the easy axis anisotropy. If, however, $K_1 < 0$, the energy is minimized when $\theta = \frac{\pi}{2}$. This implies the magnetization prefers to lie on the plane perpendicular to the uniaxial anisotropy, in this case, the xy plane, and is known as the easy plane anisotropy. A visual representation of the uniaxial anisotropy energies is seen in Figure 2.2.

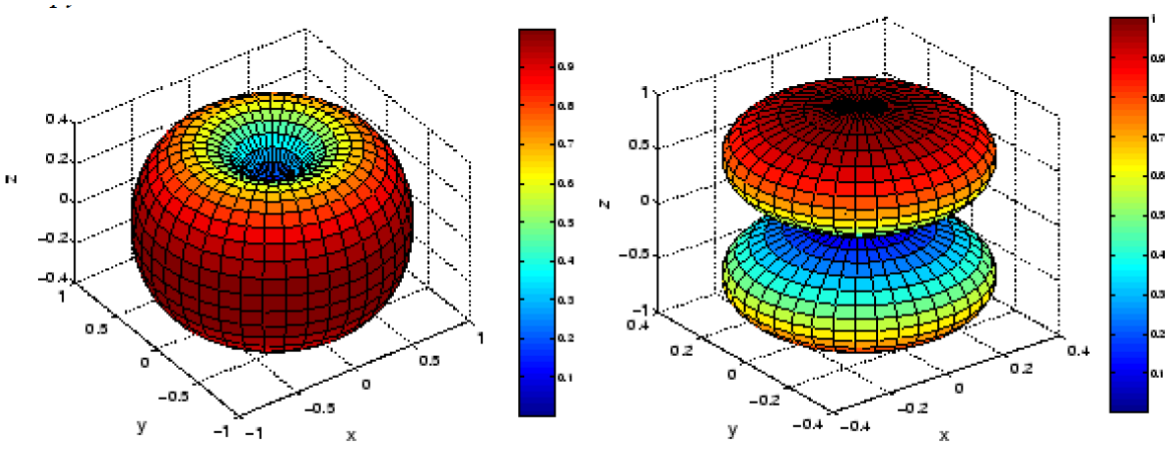

Figure 2.2 Visual representation of the uniaxial anisotropy energy density. When $K_1 > 0$ an easy axis anisotropy is created as seen in the left image. If $K_1 < 0$ an easy plane anisotropy is formed as seen in the right image[89].

Due to spin-lattice coupling in cubic crystals, many magnetic materials will experience cubic anisotropy energy, meaning there are three preferential axis of magnetization. The expansion of the energy per unit volume for cubic anisotropy energy is given as:

$$f_{MCA}(\boldsymbol{m}) = K_0 + K_1\left(m_x^2 m_y^2 + m_y^2 m_z^2 + m_z^2 m_x^2\right) + K_2 m_x^2 m_y^2 m_z^2 + \cdots \qquad (2.12)$$

Once again, only considering the anisotropy constants K_0 and K_1, it is possible to gain physical understanding of the magnetization behavior in the presence of cubic anisotropy. When $K_1 > 0$, there are a total of six easy axes of magnetization. These six axes correspond to the x, y, and z directions and consider both parallel and antiparallel alignment along these axes as an energetically minimum state. Considering when $K_1 < 0$, the minimum energy axes are defined along the vertices of the cube, for example along the [111], resulting in a total of 8 minimum energy states. The visual representation of the energy plots for cubic anisotropy is displayed in Figure 2.3.

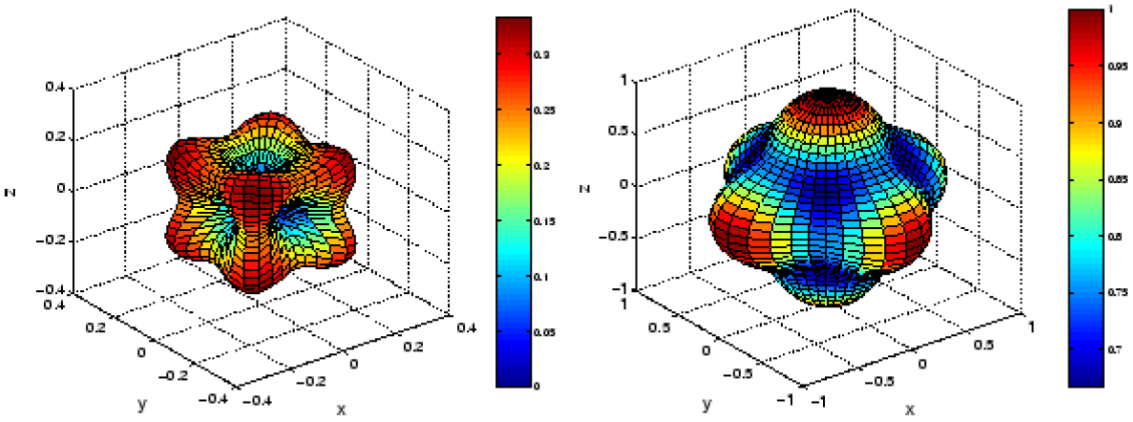

Figure 2.3 Visual representation of cubic anisotropy energy surfaces. When $K_2 > 0$ the coordinate axes, [100], [010], and [001] are the easy axes of magnetization as seen in the left image. If $K_2 < 0$, the easy axes of magnetization are along the diagonal axes, e.g. [111] as seen in the right image[89].

c. Zeeman Energy

The Zeeman energy is the energy introduced to the system in response to an externally applied magnetic field. This energy is considered a potential energy of continuous magnetic moments distribution subject to an external field H_a given in Equation 2.13.

$$E_{zeeman} = -\int \mu_0 \boldsymbol{M} \cdot \boldsymbol{H}_a \tag{2.13}$$

d. Magnetostatic Energy

The magnetostatic energy is a result of any magnetization distribution within a magnetic material. This magnetization distribution of the material will result in fictitious surface "poles" at the ends of the material. Flux closing pathways of least energy between these "poles" is through the material, opposite the direction of magnetization. This internal field in the material is known as the magnetostatic field, or more commonly, the demagnetization field, H_d [91]. A visual representation of the demagnetization field is produced below.

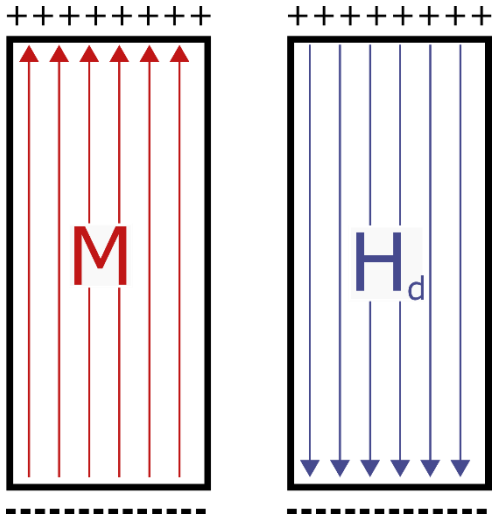

Figure 2.4 When magnetization, M, exists within a material, surface poles are formed on the surface of the material which results in an internal magnetic field. This field termed the demagnetization field, H_d, which reduces the effects of any applied magnetic field to the sample.

The demagnetization field, $H_d = -NM$, is proportional to the magnetization in the material, M, by the proportionality constant N, called the demagnetization factor[90]. This constant is a tensor function which is dependent on the sample shape, thus the demagnetization field is related to the shape anisotropy of the material. To understand how the demagnetization field is related to the shape of the object, consider a spherical magnet. When a field is applied to the magnet, the resulting internal field will be the same in all directions within the magnet. If instead the magnet is an ellipsoid, with one long axis and one short axis, the demagnetization field will be lower along the longer axis since this axis is easier to magnetize. This implies a larger field is required along the shorter axis to achieve the same degree of magnetization[92].

The mathematical representation of the demagnetization field stems from magnetostatic interactions in the body. Using Gauss's Law for Magnetism (Eq. 2.14) and Ampere's Law (Eq. 2.15):

$$\nabla \cdot \underline{B} = 0 \tag{2.14}$$

$$\nabla \times \underline{H} = \underline{J} \tag{2.15}$$

Where $\nabla \cdot$ respresents the divergence of the magnetic flux density, $\underline{B}$, and $\nabla \times$ represents the curl of the magnetic field intensity, $\underline{H}$, and $\underline{J}$ is the current density. When current density is zero, as in the case of a magnetized medium, Equation 2.15 can be rewritten as:

$$\nabla \times \underline{H} = 0 \tag{2.16}$$

The magnetic flux density and the magnetic field intensity can be related using magnetization, $\underline{M}$, and the permeability of free space, μ_0 as follows:

$$\underline{B} = \mu_0(\underline{M} + \underline{H}) \tag{2.17}$$

The energy density of the magnetostatic field is given in Equation 2.18.

$$E_{ms} = \int_{\Omega_\infty} \frac{1}{2} \mu_0 \underline{H}_m^2 dV \tag{2.18}$$

The magnetostatic energy is defined over the whole space Ω_∞. Using Equation 2.17, the magnetostatic field can be rewritten as

$$\underline{H}_m = \frac{\underline{B}_m}{\mu_0} - \underline{M} \tag{2.19}$$

By substituting the above equation into the magnetostatic energy term, the energy is rewritten as

$$E_{ms} = \int_{\Omega_\infty} \frac{1}{2} \mu_0 \underline{H}_m \cdot \left(\frac{\underline{B}_m}{\mu_0} - \underline{M} \right) dV \tag{2.20}$$

The first terms will vanish due to the integral orthogonality of $\underline{B_m}$ and $\underline{H_m}$ leaving the magnetostatic energy resulting of the magnetization of the body to be

$$E_{demag} = -\int \frac{1}{2}\mu_0 \underline{M} \cdot \underline{H_m}\, dV \tag{2.21}$$

e. Magnetoelastic Energy

The last energy considered for the ferromagnetic body is the magnetoelastic energy. This energy is a result of a change in magnetization causing a stress within a material leading to mechanical deformation or strain (Figure 2.5). To describe the strain within the material, the magnetostrictive constant, λ_s, is used. The corresponding stresses observed in the body can be represented using the magnetoelastic coupling coefficient B_{ij}. The inverse effects also exist in the body such that when a stress or strain is applied, the ferromagnetic body will change in magnetization[90].

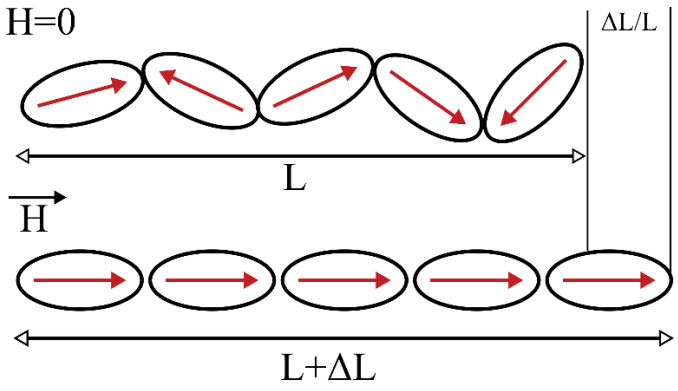

Figure 2.5 Visual representation of magnetostriction where the magnetic moments (arrows) are randomly distributed with no applied external field H and the materials has length L (top). In the presence of a field, the magnetic moments realign causing the material to change length and strain (bottom).

This phenomena is referred to as stress induced magnetic anisotropy. When $\lambda_s > 0$ then the material is easier to magnetize in the presence of tensile strain. Conversely, when $\lambda_s < 0$ the

material prefers to magnetize along the compressive axis of strain. For a cubic crystal the magnetoelastic energy is defined as:

$$E_{me} = K_1(\alpha_1^2\alpha_2^2 + \alpha_2^2\alpha_3^2 + \alpha_3^2\alpha_1^2) - \frac{3}{2}\lambda_{100}\sigma(\alpha_1^2\gamma_1^2 + \alpha_2^2\gamma_2^2 + \alpha_3^2\gamma_3^2) - 3\lambda_{111}\sigma(\alpha_1\alpha_2\gamma_1\gamma_2 + \alpha_2\alpha_3\gamma_2\gamma_3 + \alpha_3\alpha_1\gamma_3\gamma_1) \quad (2.22)$$

Where K_1 is the anisotropy constant, λ_{100} and λ_{111} are the magnetostriction constants in the [100] and [111] axis respectively, σ is the applied stress, $\alpha_1, \alpha_2, \alpha_3$are the direction cosines of magnetization, and $\gamma_1, \gamma_2, \gamma_3$ are the direction cosines of the applied stress.

f. Brown's Equations

The total free energy of the body can now be written as the sum of all the energy terms from the previous paragraphs to obtain Equation 2.23.

$$E_{total} = E_{ex} + E_{MCA} + E_{zeeman} + E_{demag} + E_{me} \quad (2.23)$$

Integrating the total energy over the volume of the magnetic material and substituting the corresponding energy expressions (excluding the magnetoelastic and magnetocrystalline terms) leads to the following integral:

$$E_{total} = \int_V \left\{A\left[(\nabla m_x)^2 + \left(\nabla m_y\right)^2 + (\nabla m_z)^2\right] + E_{MCA} - \frac{1}{2}\mu_0 \boldsymbol{M}\cdot\boldsymbol{H_d} - \mu_0\boldsymbol{M}\cdot\boldsymbol{H_a} + E_{me}\right\} dV \quad (2.24)$$

The exchange energy can be rewritten in compact form so the simplified energy expression becomes:

$$E_{total} = \int_V \left\{A(\nabla \boldsymbol{m})^2 + E_{MCA} - \frac{1}{2}\mu_0 \boldsymbol{M}\cdot\boldsymbol{H_d} - \mu_0\boldsymbol{M}\cdot\boldsymbol{H_a} + E_{me}\right\} dV \quad (2.25)$$

Taking the first variation of the energy and setting it equal to zero will find the minimum energy magnetization state in the ferromagnetic body. The first variation of the exchange, Zeeman and magnetostatic energies can be computed individually.

$$\delta E_{ex} = \int_V 2A\nabla \boldsymbol{m} \cdot \nabla \delta \boldsymbol{m}\, dV \tag{2.26}$$

Recall that $\nabla \boldsymbol{m} \cdot \nabla \delta \boldsymbol{m} = \nabla m_x \cdot \nabla \delta m_x + \nabla m_y \cdot \nabla \delta m_y + \nabla m_z \cdot \nabla \delta m_z$ and we can use the vector identity $v \cdot \nabla f = \nabla \cdot (fv) - f\nabla \cdot v$ to define the relationship of two scalars. For ease of understanding, only the x- component of the variation will be considered but can be applied to the y- and z- components in a similar form. Define $f = \delta m_x$ and $v = \nabla m_x$ then the exchange integral can be rewritten as Equation 2.27.

$$\int_V \nabla m_x \cdot \nabla \delta m_x\, dV = \int_V [\nabla \cdot (\delta m_x \nabla m_x) - \delta m_x \nabla \cdot (\nabla m_x)] dV \tag{2.27}$$

Using the divergence theorem, the first term in the integral above is rewritten as a surface integral.

$$\int_V \nabla \cdot (\delta m_x \nabla m_x) dV = \int_S \delta m_x \left(\frac{\partial m_x}{\partial n}\right) dS \tag{2.28}$$

The first variation of the x- component of the exchange integral is the sum of a surface and volume integral given in Equation 2.29.

$$\int_V \nabla m_x \cdot \nabla \delta m_x\, dV = \int_S \delta m_x \left(\frac{\partial m_x}{\partial n}\right) dS - \int_V \delta m_x \nabla \cdot (\nabla m_x)\, dV \tag{2.29}$$

The expression for first variation of the exchange energy in terms of x-, y-, and z- components and exchange constants in its final form is given in Equation 2.30.

$$\delta E_{ex} = -\int_V [2\nabla \cdot (A\nabla \boldsymbol{m}) \cdot \delta \boldsymbol{m}] dV + \int_S \left[2A\left(\frac{\partial \boldsymbol{m}}{\partial n}\right) \cdot \delta \boldsymbol{m}\right] dS \tag{2.30}$$

The first variation of the magnetostatic energy is

$$\delta E_{demag} = -\int_V \frac{1}{2}\mu_0 M_s \delta \boldsymbol{m} \cdot \boldsymbol{H_d}\, dV - \int_V \frac{1}{2} M_s \boldsymbol{m} \cdot \delta \boldsymbol{H_d}\, dV \tag{2.31}$$

which by reciprocity theorem as stated by Brown[93] can be reduced to the following form:

$$\delta E_{demag} = -\int_V \mu_0 M_s \boldsymbol{H_d} \cdot \delta \boldsymbol{m}\, dV \tag{2.32}$$

Similarly, the first variation of the Zeeman energy resulting from the applied field is simply

$$\delta E_{zeeman} = \int_V \mu_0 M_s \boldsymbol{H}_a \cdot \delta \boldsymbol{m} \tag{2.33}$$

Taking the first variation of the magnetocrystalline anisotropy energy and the magnetoelastic energy is equivalent to writing the first variations in the simplified forms:

$$\delta E_{MCA} = \int_V \frac{\partial E_{MCA}}{\partial \boldsymbol{m}} \cdot \delta \boldsymbol{m}\, dV \tag{2.34}$$

$$\delta E_{me} = \int_V \frac{\partial E_{me}}{\partial \boldsymbol{m}} \cdot \delta \boldsymbol{m}\, dV \tag{2.35}$$

Finally, taking the sum of all first variations of all the energy terms and setting it equal to zero yields equation 2.36:

$$\delta E_{total} = -\int_V \left[2\nabla \cdot (A\nabla \boldsymbol{m}) + \mu_0 M_s \boldsymbol{H_d} + \mu_0 M_s \boldsymbol{H}_a - \frac{\partial E_{MCA}}{\partial \boldsymbol{m}} - \frac{\partial E_{me}}{\partial \boldsymbol{m}}\right] \cdot \delta \boldsymbol{m} dV + \int_S \left[2A\left(\frac{\partial \boldsymbol{m}}{\partial n}\right) \cdot \delta \boldsymbol{m}\right] dS = 0 \tag{2.36}$$

The most general variation of the vector field $\boldsymbol{m}$ can be represented as a small angle rotation of magnitude $\delta\theta$ so the variation $\delta \boldsymbol{m} = \boldsymbol{m} \times \delta \boldsymbol{\theta}$. Using this definition of $\delta \boldsymbol{m}$ and the vector property

$\vec{v} \cdot (\vec{w} \times \vec{u}) = \vec{u} \cdot (\vec{v} \times \vec{w}) = -\vec{u} \cdot (\vec{w} \times \vec{v})$, the first variation can be rewritten in terms of the angle rotation.

$$\delta E_{total} = \int_V \boldsymbol{m} \times \left[2\nabla \cdot (A\nabla \boldsymbol{m}) + \mu_0 M_s \boldsymbol{H_d} + \mu_0 M_s \boldsymbol{H_a} - \frac{\partial E_{MCA}}{\partial \boldsymbol{m}} - \frac{\partial E_{me}}{\partial \boldsymbol{m}}\right] \cdot \delta \boldsymbol{\theta}\, dV + \int_S \left[2A \frac{\partial \boldsymbol{m}}{\partial \boldsymbol{n}} \times \boldsymbol{m}\right] \cdot \delta \boldsymbol{\theta}\, dS \tag{2.37}$$

Assuming small angle rotations can be approximated to be zero, the two equations are found to describe the minimum energy of magnetization.

$$\begin{cases} \boldsymbol{m} \times \left[2\nabla \cdot (A\nabla \boldsymbol{m}) + \mu_0 M_s \boldsymbol{H_d} + \mu_0 M_s \boldsymbol{H_a} - \frac{\partial E_{MCA}}{\partial \boldsymbol{m}} - \frac{\partial E_{me}}{\partial \boldsymbol{m}}\right] = 0 \\ \left[2A \frac{\partial \boldsymbol{m}}{\partial \boldsymbol{n}} \times \boldsymbol{m}\right]_s = 0 \end{cases} \tag{2.38}$$

The above equations can be simplified by noting that the cross product of two vectors are zero if either or both vectors are zero and $\boldsymbol{m} \neq 0$, $\frac{\partial \boldsymbol{m}}{\partial \boldsymbol{n}} = 0$. The equations are further simplified by introducing an effective field to redefine Equation 2.38.

$$\boldsymbol{H_{eff}} = \frac{2}{\mu_0 Ms} \nabla \cdot (A\nabla \boldsymbol{m}) + \boldsymbol{H_d} + \boldsymbol{H_a} - \frac{1}{\mu_0 M_s} \frac{\partial E_{MCA}}{\partial \boldsymbol{m}} - \frac{1}{\mu_0 M_s} \frac{\partial E_{me}}{\partial \boldsymbol{m}} \tag{2.39}$$

From Equation 2.39, it is evident that the general definition for the effective field can be defined as:

$$\boldsymbol{H_{eff}} = -\frac{1}{\mu_0 M_s} \frac{\partial E_{total}}{\partial \boldsymbol{m}} \tag{2.40}$$

The simplifications above allow Equation 2.38 to be rewritten as the recognizable form of Brown's Equations[93] presented here:

$$\begin{cases} \mu_0 M_s \boldsymbol{m} \times \boldsymbol{H_{eff}} = 0 \\ \left.\frac{\partial \boldsymbol{m}}{\partial \boldsymbol{n}}\right|_s = 0 \end{cases} \tag{2.41}$$

These equations when solved will produce the final magnetization configuration expected at equilibrium state for a ferromagnetic body. However, no information is provided on the magnetization dynamics before equilibrium is reached.

g. Landau-Lifshitz-Gilbert (LLG) Equation

To address the dynamic motion of magnetization, Landau and Lifshitz proposed a model in 1935 based on the continuum precession equation[94]. This model considers both quantum mechanical and any anisotropy effects to govern the magnetic behavior. In order to preserve the magnitude of magnetization and for an improved dynamic response of the system, Gilbert introduced an additional damping term in 1955 to develop the governing equation for magnetization dynamics known as the Landau-Lifshitz-Gilbert (LLG) Equation[95].

$$\frac{\partial \boldsymbol{M}}{\partial t} = -\gamma \boldsymbol{M} \times \boldsymbol{H}_{eff} + \frac{\alpha}{M_s} \boldsymbol{M} \times \frac{\partial \boldsymbol{M}}{\partial t} \tag{2.42}$$

Where $\boldsymbol{M}$ is the magnetization, $\boldsymbol{H}_{eff}$ is the effective field, $\gamma = 2.21 \times 10^5 \frac{m}{A \cdot s}$ is the gyromagnetic ratio, M_s and α are the saturation magnetization and gilbert damping respectively, which are properties of the magnetic material. The first term, $\boldsymbol{M} \times \boldsymbol{H}_{eff}$, describes the precessional motion of the magnetization vectors as they align along the direction of the effective field. The second term, $\boldsymbol{M} \times \frac{\partial \boldsymbol{M}}{\partial t}$, describes the damping motion of the magnetization. For materials with higher gilbert damping constants, the magnetization will reach equilibrium faster. A visual representation of the dynamic magnetization is given in Figure 2.6.

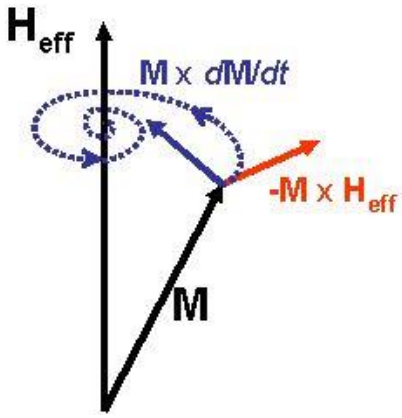

Figure 2.6 Visual representation of damped magnetization behavior where the red solid line represents the magnetization precessional motion and the blue dashed lines represents the damped behavior of magnetization around the effective field acting on the system.

2.3 Development of LLG Weak Form

In order to study the magnetization response of a multiferroic system, the micromagnetics governing equation must be coupled to mechanics. This is necessary to duplicate device behavior in response to voltage generated strains in the ferroelectric substrate. Liang et al.[68] was the first to implement this strain-coupled behavior in a finite element platform. The complete derivation of weak form for the governing equation of magnetization dynamics is outlined in the following sections.

a. Energy Terms

As previously noted, the total energy of the system has contributions from the exchange(E_{ex}), magnetocrystalline(E_{cubic}), Zeeman(E_{ext}), magnetostatic(E_d) and the magnetoelastic interactions. It is worth noting that each energy term boils down to some form of the dot product of the normalized magnetization, $\underline{m}$ and the corresponding magnetic field. Here, it will be assumed that the crystal structure is cubic. The energy terms are then given by the following equations:

$$E_{ex} = A_{ex}\left(\nabla \underline{m}\right)^2 \tag{2.43}$$

$$E_{cubic} = K_1(m_1^2m_2^2 + m_1^2m_3^2 + m_2^2m_3^2) + K_2(m_1^2m_2^2m_3^2) \tag{2.44}$$

$$E_{ext} = -\mu_0 M_s(\underline{m} \cdot \underline{H}_{ext}) \tag{2.45}$$

$$E_d = -\frac{\mu_0 M_s}{2}(\underline{m} \cdot \underline{H}_d) \tag{2.46}$$

$$E_{me} = \frac{1}{2}\underline{\underline{\varepsilon}}^{el} : \underline{\underline{\underline{\underline{C}}}} : \underline{\underline{\varepsilon}}^{el} \tag{2.47}$$

where M_s is the saturation magnetization of the material, A_{ex} is the exchange stiffness of the material, the K_i are anisotropy constants determined from experiment, ε^{el} is the elastic strain tensor, and C is the elastic stiffness tensor of the material. In a magnetoelastic material, the magnetic moments and displacements of the material are coupled such that the total strain $\left(\underline{\underline{\varepsilon}}\right)$ is a summation of magnetic$\left(\underline{\underline{\varepsilon}}^{m}\right)$ and mechanical/elastic $\left(\underline{\underline{\varepsilon}}^{el}\right)$components. In component form, the strain associated with a cubic crystal is

$$\varepsilon_{ij}^{m} = \begin{cases} \frac{3}{2}\lambda_{100}\left(m_i m_j - \frac{1}{3}\right), & for\ i = j \\ \frac{3}{2}\lambda_{111} m_i m_j, & for\ i \neq j \end{cases} \tag{2.48}$$

b. Effective Field

Since the LLG equation is determined by both the magnetization and effective field, it is important to convert each of the energy terms to an equivalent magnetic field. Using Equation 2.40, the fields can be obtained by taking the derivatives of the corresponding energy terms with respect to the normalized magnetization. The corresponding fields to each of the energy terms are presented below. The Zeeman energy is a result of the applied external field.

$$\underline{H}_{ext} = \underline{H}_{app} \tag{2.49}$$

Taking the derivative of the magnetoelastic term with respect to the magnetization vector and substituting the expression for the elastic strains in terms of the magnetostrictive strains yields

$$\underline{H}_{me} = -\frac{1}{\mu_0 M_s}\frac{\partial}{\partial \underline{m}}\left(\frac{1}{2}\underline{\underline{\underline{\underline{C}}}}\left(\underline{\underline{\varepsilon}}^{el}\right)^2\right) = -\frac{1}{\mu_0 M_s}\frac{\partial}{\partial \underline{m}}\left(\frac{1}{2}\underline{\underline{\underline{\underline{C}}}}\left(\underline{\underline{\varepsilon}} - \underline{\underline{\varepsilon}}^{m}\right)^2\right) = -\frac{1}{\mu_0 M_s}\underline{\underline{\underline{\underline{C}}}}\left(\underline{\underline{\varepsilon}} - \underline{\underline{\varepsilon}}^{m}\right)\cdot\frac{\partial \varepsilon^m}{\partial \underline{m}} \tag{2.50}$$

The effective field due to the cubic anisotropy is given in component form.

$$\underline{H}^i_{cubic} = -\frac{2m_i}{\mu_0 M_s}\left[K_1\left(m_j^2 + m_k^2\right) + K_2\left(m_j^2 m_k^2\right)\right] \tag{2.51}$$

The effective field due to magnetostatic energy is the demagnetization field. However, it is advantageous to write the demagnetization field in terms of a scalar potential. From Ampere's Law ($\nabla \times H_d = 0$), Gauss' Law ($\nabla \cdot B = 0$), and the relationship between the magnetic induction and magnetization ($B = H_d + M_s\underline{m}$), the demagnetization field can be expressed in terms of a magnetic scalar potential (ϕ) by using the property $\nabla \times (\nabla scalar) = 0$. The corresponding field of the magnetostatic energy is given below.

$$\underline{H}_d = -\nabla\phi \tag{2.52}$$

Before deriving the effective exchange field, some preliminary calculations are performed. Starting with expanding $\nabla\underline{m}$:

$$\nabla\underline{m} = \left(\hat{e}_x\frac{\partial}{\partial x} + \hat{e}_y\frac{\partial}{\partial y} + \hat{e}_z\frac{\partial}{\partial z}\right)\left(m_1\hat{e}_x + m_2\hat{e}_y + m_3\hat{e}_z\right) = m_{1,x}\hat{e}_x\hat{e}_x + m_{1,y}\hat{e}_y\hat{e}_x + m_{1,z}\hat{e}_z\hat{e}_x +$$
$$m_{2,x}\hat{e}_x\hat{e}_y + m_{2,y}\hat{e}_y\hat{e}_y + m_{2,z}\hat{e}_z\hat{e}_y + m_{3,x}\hat{e}_x\hat{e}_z + m_{3,y}\hat{e}_y\hat{e}_z + m_{3,z}\hat{e}_z\hat{e}_z \tag{2.53}$$

The above expression is equivalent to the matrix

$$\nabla \underline{m} = \begin{pmatrix} m_{1,x} & m_{1,y} & m_{1,z} \\ m_{2,x} & m_{2,y} & m_{2,z} \\ m_{3,x} & m_{3,y} & m_{3,z} \end{pmatrix} \tag{2.54}$$

Note that $\left(\nabla \underline{m}\right)^2 = \left(\nabla \underline{m}\right) : \left(\nabla \underline{m}\right)$ is the double dot product (dot product of matrices), expanding the expression:

$$\left(\nabla \underline{m}\right)^2 = \left(\nabla \underline{m}\right) : \left(\nabla \underline{m}\right) = \begin{pmatrix} m_{1,x} & m_{1,y} & m_{1,z} \\ m_{2,x} & m_{2,y} & m_{2,z} \\ m_{3,x} & m_{3,y} & m_{3,z} \end{pmatrix} : \begin{pmatrix} m_{1,x} & m_{1,y} & m_{1,z} \\ m_{2,x} & m_{2,y} & m_{2,z} \\ m_{3,x} & m_{3,y} & m_{3,z} \end{pmatrix}$$

$$= m_{1,x}^2 + m_{1,y}^2 + m_{1,z}^2 + m_{2,x}^2 + m_{2,y}^2 + m_{2,z}^2 + m_{3,x}^2 + m_{3,y}^2 + m_{3,z}^2 \tag{2.55}$$

Recall, in order to find the effective field, a derivative of the energy taken with respect to the magnetization vector must be computed. Specifically, for the exchange energy, the first variation is taken such that

$$\int [\delta E_{ex}] dV = \int \left[A_{ex} \delta \left(\nabla \underline{m}\right)^2 \right] dV = A_{ex} \int \left[\underline{H}_{eff} \cdot \delta \underline{m} \right] dV \tag{2.57}$$

The first variation is

$$\int A_{ex} \delta \left(\nabla \underline{m}\right)^2 dV$$

$$= A_{ex} \int \delta \left(m_{1x}^2 + m_{1,y}^2 + m_{1,z}^2 + m_{2,x}^2 + m_{2,y}^2 + m_{2,z}^2 + m_{3,x}^2 + m_{3,y}^2 + m_{3,z}^2 \right) dV$$

$$= A_{ex} \int \delta \left(m_{i,j} m_{i,j} \right) dV = A_{ex} \int 2 m_{i,j} \delta m_{i,j} \, dV \tag{2.58}$$

Integrating by parts allows the integrand to be separated into a volume and a surface integral.

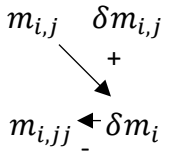

$$A_{ex} = \int 2m_{i,j}\delta m_{i,j}\, dV = 2A_{ex}\int\left[-m_{i,jj}\delta m_i\right] dV + 2A_{ex}\int\left[m_{i,j}\delta m_i\right] dS \qquad (2.59)$$

From the boundary conditions we have $m_{i,j}\delta m_i \rightarrow 0$. Now consider the following calculation:

$$\nabla^2\underline{m} = \nabla\left(\nabla\cdot\underline{m}\right) - \nabla\times\left(\nabla\times\underline{m}\right) = \partial_k\hat{e}_k(\partial_m\hat{e}_m\cdot m_n\hat{e}_n) - \partial_j\hat{e}_j\times\left(\epsilon_{lin}m_{n,i}\hat{e}_l\right)$$

$$= \partial_k\hat{e}_k\left(m_{n,m}\delta_{mn}\right) - \left(m_{n,ij}\epsilon_{lin}\epsilon_{rjl}\hat{e}_r\right) = m_{n,nk}\hat{e}_k - \left[m_{n,ij}\left(\delta_{ir}\delta_{nj} - \delta_{ij}\delta_{nr}\right)\hat{e}_r\right]$$

$$= m_{n,nk}\hat{e}_k - m_{n,nr}\hat{e}_r + m_{r,jj}\hat{e}_r = m_{k,jj}\hat{e}_k \qquad (2.60)$$

Therefore,

$$\int A_{ex}\delta\left(\nabla\underline{m}\right)^2 dV = 2A_{ex}\int\left[\nabla^2\underline{m}\cdot\delta\underline{m}\right] dV \qquad (2.61)$$

Using the above equation, it is possible to define the effective exchange field as

$$H_{ex} = \frac{2A_{ex}}{\mu_0 M_s}\nabla^2\underline{m} \qquad (2.62)$$

c. Weak formulation

In order to implement LLG in a multiphysics finite element software, it is necessary to express the LLG equation in a weak form. The weak form requires an order reduction of the governing differential equation. The normalized LLG equation is given in Equation 2.63.

$$\frac{\partial\underline{m}}{\partial t} = -\mu_0\gamma\left(\underline{m}\times\underline{H}_{eff}\right) + \alpha\left(\underline{m}\times\frac{\partial\underline{m}}{\partial t}\right) \qquad (2.63)$$

Here $\underline{m}$ is the normalized magnetization vector, μ_0 is the permeability of free space, γ is the gyromagnetic ratio, and α is the Gilbert damping constant. Thermal fluctuations are neglected and room temperature material properties are used. Recall the effective magnetic field (H_{eff}) of the system is the sum of the fields derived in the previous section. Specifically, the effective field is given by:

$$\underline{H}_{eff} = \underline{H}_{ex} + \underline{H}_{cubic} + \underline{H}_{ext} + \underline{H}_{d} + \underline{H}_{me} \tag{2.64}$$

Weakening the governing equation involves rewriting it in the form of a volume integral multiplied by a test function ψ.

$$\int \left(\left[\frac{\partial \underline{m}}{\partial t} - \alpha \left(\underline{m} \times \frac{\partial \underline{m}}{\partial t} \right) \right] \cdot \psi + \mu_0 \gamma \left(\underline{m} \times \underline{H}_{eff} \right) \cdot \psi \right) dV = 0 \tag{2.65}$$

From the definition of the effective field, the third term becomes

$$\int \mu_0 \gamma \left(\underline{m} \times \underline{H}_{eff} \right) \cdot \psi \, dV = \int \mu_0 \gamma \left(\underline{m} \times \left[\underline{H}_{ex} + \underline{H}_{cubic} + \underline{H}_{ext} + \underline{H}_{d} + \underline{H}_{me} \right] \right) \cdot \psi \, dV \tag{2.66}$$

Since the effective field due to the exchange interaction involves second order derivatives, it must be weakened through integration by parts. Noting that the cross product is distributive, the following integral is obtained

$$\int \mu_0 \gamma \left(\underline{m} \times \underline{H}_{ex} \right) \cdot \psi \, dV = \frac{2A_{ex}\gamma}{M_s} \int \left(\underline{m} \times \nabla^2 \underline{m} \right) \cdot \psi \, dV$$

$$= \frac{2A_{ex}\gamma}{M_s} \int \left[m_n \hat{e}_n \times \left(m_{i,jj} \hat{e}_i \right) \right] \cdot \left(\psi_s \, \hat{e}_s \right) dV$$

$$= \frac{2A_{ex}\gamma}{M_s} \int \left(m_n m_{i,jj} \epsilon_{lni} \hat{e}_l \right) \cdot \left(\psi_s \hat{e}_s \right) dV$$

$$= \frac{2A_{ex}\gamma}{M_s} \int \epsilon_{sni} \psi_s m_n m_{i,jj} \, dV \tag{2.67}$$

In order to weaken the equation, it is necessary to "share" derivatives from the $m_{i,jj}$ term with the remaining terms. This is accomplished through integration by parts:

$$\frac{2A_{ex}\gamma}{M_s} \int \epsilon_{sni} \psi_s m_n m_{i,jj} \, dV = \frac{2A_{ex}\gamma}{M_s} \left(\int (\psi_s m_n)_{,j} m_{i,j} \epsilon_{sni} \, dV + \int (\psi_s m_n m_{i,j}) n_j \epsilon_{sni} dS \right) \tag{2.68}$$

The boundary conditions from above indicate $\psi_s m_{i,j} m_n \to 0$, implies

$$\frac{2A_{ex}\gamma}{M_s} \int \epsilon_{sni} \psi_s m_n m_{i,jj} \, dV = -\frac{2A_{ex}\gamma}{M_s} \int \left(\psi_{s,j} m_n + \psi_s m_{n,j} \right) m_{i,j} \epsilon_{sni} \, dV \tag{2.69}$$

Note that $\psi_s m_{i,j} m_{n,j} \epsilon_{sni} = 0$ so the exchange term reduces to

$$-\frac{2A_{ex}\gamma}{M_s} \int \left(\psi_{s,j} m_n + \psi_s m_{n,j} \right) m_{i,j} \epsilon_{sni} \, dV = -\frac{2A_{ex}\gamma}{M_s} \int m_{i,j} \psi_{s,j} m_n \epsilon_{sni} \, dV \tag{2.70}$$

Observe that $m_{i,j} \psi_{s,j} m_n \epsilon_{sni} = \epsilon_{sni} m_n m_{i,j} \psi_{s,j}$ which is the cross product between the magnetization vector and its spatial derivative dotted with the spatial derivative of the test function, this implied the integral can be rewritten as

$$-\frac{2A_{ex}\gamma}{M_s} \int m_{i,j} \psi_{s,j} m_n \epsilon_{sni} \, dV \to -\frac{2A_{ex}\gamma}{M_s} \sum_S \int \left[\left(\underline{m} \times \frac{\partial \underline{m}}{\partial x_s} \right) \cdot \frac{\partial \psi_s}{\partial x_s} \right] dV \tag{2.71}$$

Finally, using the above equations, the weak form of the LLG equation is found to be

$$\int \left\{ \left[\frac{\partial \underline{m}}{\partial t} - \alpha \left(\underline{m} \times \frac{\partial \underline{m}}{\partial t} \right) \right] \right\} \cdot \psi \, dV = \int \mu_0 \gamma (\underline{m}) \times \left[\underline{H}_{cubic} + \underline{H}_{ext} + \underline{H}_d + \underline{H}_{me} \right] \cdot \psi \, dV + \frac{2A_{ex}\gamma}{M_s} \sum_S \int \left[\left(\underline{m} \times \frac{\partial \underline{m}}{\partial x_s} \right) \cdot \frac{\partial \psi_s}{\partial x_s} \right] dV \tag{2.72}$$

2.4 Piezoelectricity Basics

Piezoelectricity was first described by Pierre and Paul-Jacques Curie in 1880 when they noted that materials can exhibit an electric charge when subject to an applied stress (direct piezoelectric effect)[39]. The origin of this effect can be found in the unit cell of these materials. The unit cell of piezoelectric materials are not symmetric despite the net neutral charge of the unit cell. As a result, in the unstressed arrangement, the placement of charges (electric dipole moments) are perfectly balanced. When the unit cell is deformed as a result of the applied external stress, the distance between charges are changed, creating unbalanced charges and a net dipole moment in the unit cell. This rearrangement of charges can appear as net surface charges on the material. The reverse piezoelectric effect also exists which occurs due to the application of a voltage on the material. The applied voltages cause the charges within the material to change positions changing the shape of the unit cell. Thus in the inverse piezoelectric effect, a voltage on the material results in mechanical deformation[96], [97]. Figure 2.7 illustrates the piezoelectric effect.

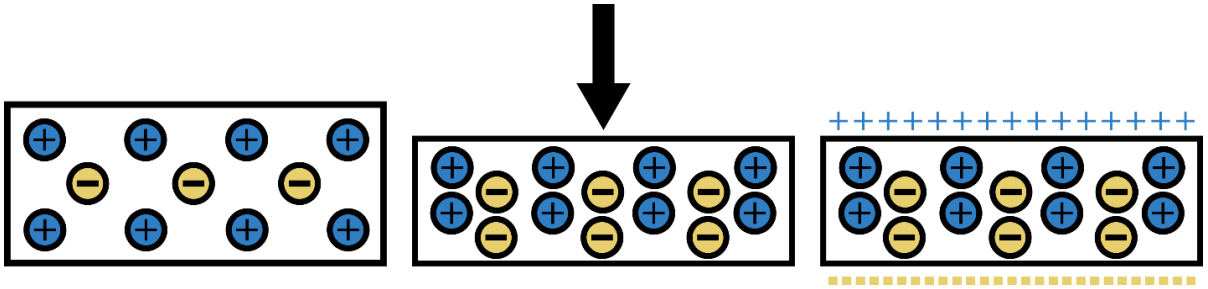

Figure 2.7 Visual representation of the direct piezoelectric effect. Initial distribution of charges within a material is arranged such that all dipole moments are equally balanced resulting in a net neutral charge of the material (left). When an external stress is applied to the material, the charges are rearranged (middle). This rearrangement causes a resultant surface charge to be generated on the surface of the material (right).

The piezoelectric behavior can be summarized by a set of constitutive equations developed from the electric enthalpy function. These equations are valid for the linear response of a piezoelectric

material when the applied electric field or stress to the material is low. The electromechanical equations for a linear piezoelectric material can be written as[97]:

$$\varepsilon_i = S_{ij}^E \sigma_j + d_{ij} E_m \tag{2.73}$$

$$D_m = d_{mi} \sigma_i + e_i^\sigma E_k \tag{2.74}$$

Here the indices refer to $i, j = 1,2, \ldots 6$ and $m, k = 1,2,3$ referring to the material coordinates illustrated in Figure 2.8.

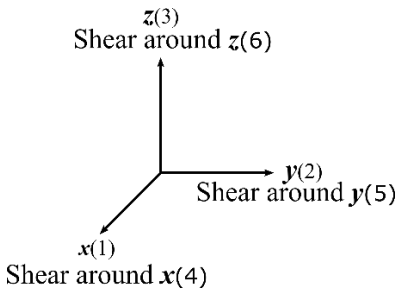

Figure 2.8 Indices representation of piezoelectric constitutive equations

The variables in Equations 2.73 and 2.74 are summarized in Table 2.1.

Table 2.1 Definitions of piezoelectric constitutive variables.

Variable	Definition
ε	Strain vector (m/m)
S	Matrix of compliance coefficients (m^2/N)
σ	Stress vector (N/m^2)
d	Matrix of piezoelectric strain constants (m/V)
E	Vector of applied electric field (V/m)
D	Vector of electric displacement (C/m^2)
e	Vector of dielectric coefficients (C/V)

The superscripts in Equations 2.73 and 2.74 correspond to measurements taken at constant electric field(E) and stress(σ). The physical interpretation of the elastic compliance matrix, S_{ij} , can be

thought of as the ratio of the strain in the i-direction to the stress in the j-direction. The piezoelectric strain constant, d_{ij}, is thought of as the ratio of the strain in the j-direction in response to the electric field applied in the i-direction. Lastly the dielectric constant, e_{ij}, is a measure of the charge per unit area in the i-axis which accumulates due to the electric field applied along the j-axis.

To reiterate, the equations discussed apply to the material response of piezoelectric materials where there exists a linear relationship between the applied stress/electric field and the corresponding surface charge/strain. A special class of piezoelectric materials, called ferroelectric materials, already have a net dipole moment, or polarization existing within the material in the absence of an electric field (spontaneous polarization). As a result, an application of an external field will cause a change in polarization and this material response is governed by a different set of equations discussed in Chapter 5.

2.5 Summary

This chapter focuses on the development of the magnetization dynamics equation, LLG, used in the projects covered throughout this dissertation. The individual energy terms contributing to the dynamics equations were discussed briefly. Additionally, mathematical steps to obtain the weak formulation of the LLG equation were outlined to implement the equation into a finite element platform. Lastly the constitutive relationships of a piezoelectric material was provided to understand the substrate response in multiferroic materials when an electric field is applied.

III. 360 Degree Deterministic Magnetization Rotation in a Three Ellipse Magnetoelectric Heterostructure

3.1 Introduction

Magnetoelectric heterostructures with deterministic magnetization reorientation offer a new approach to nanoscale devices such as memory, logic, and nanomotors[98]–[100]. Deterministic control refers to controlling the direction of magnetization rotation in a repeatable manner. This requires the breaking of symmetry in the magnetic energy profile together with a mechanism to control the magnetization energy landscape. There are multiple mechanisms that can be used to drive magnetization reorientation in magnetic heterostructures. These include application of an external magnetic field, injection of spin current, changing the magnetic dipole interactions with neighboring structures, and using strain to change the magnetostrictive energy[29], [101]. Among these the latter, in the form of strain-coupled magnetoelectric heterostructures, has been shown to be the most energy efficient[102]. Strain-coupled magnetoelectric heterostructures are composite structures with thin magnetostrictive materials on top of piezoelectric substrates. When voltage is applied to the piezoelectric substrate, an in-plane strain is generated. This strain couples to the magnetostrictive material, driving magnetization reorientation.

The design of magnetoelectric heterostructures with deterministic switching behavior requires control of the various contributions to the magnetic energy. These include the magnetocrystalline anisotropy, external magnetic field (Zeeman), magnetization gradient (exchange), magnetoelastic, and shape (magnetostatic) anisotropy[90]. The magnetocrystalline anisotropy energy is associated with the crystal structure, with some materials displaying an easy axis and a hard axis of magnetization associated with various crystallographic directions. The Zeeman Energy is

associated with the energy produced from an external magnetic field of any origin. The exchange energy is associated with the interaction energy between two magnetic moments within a material. Exchange energy is a quantum effect that acts over short distances (equivalent to the exchange length of the material) between neighboring magnetic spins. The magnetoelastic energy is associated with magnetostriction where strain modifies the magnetic energy profile, inducing easy and hard directions of magnetization. The shape anisotropy (demagnetization energy) is the energy associated with the internal magnetic field opposing the direction of magnetization within the magnetic element. Shape anisotropy can also induce easy and hard directions. The effective magnetic field at a point is found by taking the partial derivative of the magnetic energy with respect to magnetization. This effective field produces a torque on the local magnetic moments, driving them to rotate toward the direction that minimizes their energy in the effective field.

The symmetric shape anisotropy of an ellipse, with an easy direction along the major axis and hard direction along the minor axis, can be changed with applications of anisotropic energies of different origins. The application of in-plane strain to a magnetostrictive ellipse can rotate the easy direction away from the major axis. If the magnetostrictive constant of a material, λ_s, is positive, the direction of a uniaxial tensile stress component becomes easier to magnetize. Similarly, if λ_s is negative, the direction of a uniaxial compressive stress component becomes easier to magnetize[90]. This effect is enhanced when the stress state is biaxial with orthogonal tensile and compressive stress components. In a magnetoelectric heterostructure, this stress is induced by coupling to the strain produced by an electric field in a piezoelectric. When the principal strain components align with the major and minor axes of the ellipse, and are of sufficient magnitude and have the correct sign to make the minor axis become the easy axis, the magnetization will rotate a full 90^o in either a clockwise or counter-clockwise direction[103]. To

achieve deterministic switching, the symmetry of the magnetic energy must be broken. Several methods have been proposed to accomplish this in strain-mediated multiferroic heterostructures, generally leading to complex nanomagnet geometries and electrode configurations. Among these are a four-fold-symmetry nanomagnet[99] and a "cat-eye" geometry[104]. Fabrication of these structures with complicated geometries and patterned electrodes with multiple leads can be more difficult than fabrication of the proposed three nanoellipse structure and requires a complex control strategy to drive the magnetization reorientation.

Several methods have been developed to obtain deterministic control of magnetization rotation. Patterned electrodes can be used to sequentially rotate the strain for deterministic control. This requires a complicated control mechanism since each pair of electrode must be actuated in sequence[98], [104], [105]. A simpler control mechanism was proposed by Li et al. [106] for 180^o out-of-plane magnetization switching. This method, known as strain-mediated ballistic switching, takes advantage of magnetization dynamics. Magnetization has angular momentum, and thus undergoes damped precession about the direction of an effective magnetic field when the field undergoes a sudden change. Ballistic switching was extended by Peng et al.[107] to in-plane 180^o magnetization switching using two electrodes and a single short voltage pulse. A finite element simulation was used to demonstrate strain-mediated ballistic switching in a single Cobalt Iron Boron (CoFeB) ellipse on a PZT thin film. The magnetization in the ellipse was initially aligned with the positive x-axis ($m_x = 1$) parallel to the major axis of the ellipse with the y-axis aligned with the minor axis. Two electrodes perpendicular to the x-axis were actuated and produced approximately 1100 ppm in-plane tensile strain along the ellipse y-axis. The y-axis, with tensile strain large enough to overcome the demagnetization energy, became the new easy axis of magnetization for the CoFeB element. The tensile strain drove the magnetization to precess about

the y-axis. The voltage induced strain was released when m_x was between the 0 and -1. With the strain removed, damped precession began with the magnetization moving about the negative x-direction and damped to 180° from its original configuration. A visual representation of the ballistic switching method is given in Figure 3.1. This simpler control mechanism requiring only a single voltage pulse is implemented in the three-ellipse geometry discussed below.

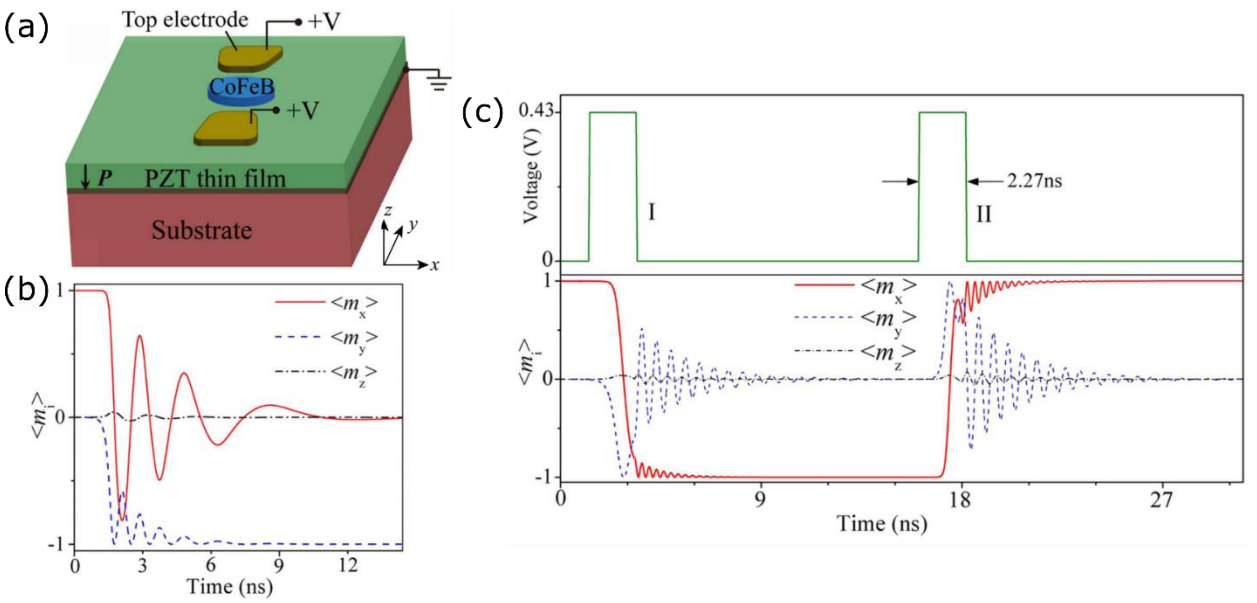

Figure 3.1 (a) The multiferroic heterostructure proposed by Peng et al.[107] to achieve 180° switching in a single nanoellipse. **(b)** The magnetization dynamics response of the three magnetic components, m_x, m_y and m_z with application of a static voltage applied to the patterned electrodes demonstrates 90° switching behavior. If the applied voltage is turned off when the m_x (red) component is between 0 and 1, then **(c)** the magnetization successfully rotates 180° in the x- direction as seen in the bottom panel. The corresponding voltage pulse is show in the green curve in the top panel.

3.2 Design Approach

Design of the geometry to enable control of the magnetization dynamics of the three ellipse configuration was performed in two steps. First, simulations were performed using a conventional micromagnetics finite difference code without strain coupling. The conventional micromagnetics

simulation was used to create the initial geometry of the three ellipse structure. The uncoupled micromagnetics model assumes uniform strain, therefore neglecting the strain variations present in the magnetostrictive material[82]. Next, simulations were performed using a finite element code with coupled micromagnetics, elastodynamics, and linear piezoelectric constitutive behavior to assess the magnetization dynamics associated with the geometry and effects of strain gradients across the structure.

a. Micromagnetics Theory Overview

Micromagnetics theory is used to obtain the spatial distribution of magnetization within magnetic materials at submicron length scales[108]. The motion of the unit magnetic moment vectors ($\underline{m}$) are governed by the Landau-Lifshitz-Gilbert (LLG) Equation, Equation 3.1,

$$\frac{\partial \underline{m}}{\partial t} = -\mu_0 \gamma \left(\underline{m} \times \underline{H}_{eff}\right) + \alpha \left(\underline{m} \times \frac{\partial \underline{m}}{\partial t}\right) \tag{3.1}$$

where μ_0 is the permeability of free space, γ is the gyromagnetic ratio, and α is the Gilbert damping constant. The effective magnetic field ($\underline{H}_{eff}$) is the partial derivative of the magnetization energy with respect to magnetic moment. This results in the summation of contributions from the externally applied field ($\underline{H}_{ext}$), the field due to the exchange interaction ($\underline{H}_{ex}$), the demagnetization field ($\underline{H}_{d}$) and the magnetoelastic field ($\underline{H}_{me}$). The demagnetization field can be found from the magnetic potential, φ, where $\underline{H}_{d} = -\nabla\varphi$. The magnetic scalar potential is the mathematical construct that describes the path independent spatial distribution of magnetic potential energies referenced to zero in free space. The CoFeB elements are assumed to be amorphous based on experimental observations of thin film, amorphous CoFeB that indicate insignificant MCA contributions[109], [110], so a magnetocrystalline anisotropy (MCA) field is not considered. The

LLG equation is solved within the domain of the magnetic material. The effective magnetic field contributions are derived from their corresponding magnetization energy densities using Equation 3.2a,

$$\underline{H}_{eff} = -\frac{1}{\mu_0 M_s}\left(\frac{\partial E_{tot}}{\partial \underline{m}}\right) \tag{3.2a}$$

$$= \underline{H}_{ext} + \underline{H}_{ex} + \underline{H}_{d} + \underline{H}_{me} \tag{3.2b}$$

where M_s is the magnetic saturation of the material, and E_{tot} is the sum of the external energy, exchange energy (a continuum approximation of the energy between two spins), demagnetization energy and the elastic energy terms (the latter contributes to the magnetoelastic field). These terms are summarized in Equations 3.3-3.6,

$$E_{ext} = -\mu_0 M_s(\underline{m} \cdot \underline{H}_{ext}) \tag{3.3}$$

$$E_{ex} = A_{ex}\left(\nabla \underline{m}\right)^2 \tag{3.4}$$

$$E_d = -\frac{\mu_0 M_s}{2}(\underline{m} \cdot \underline{H}_d) \tag{3.5}$$

$$E_{el} = \frac{1}{2}\underline{\underline{\varepsilon}}^{el} : \underline{\underline{\underline{\underline{C}}}} : \underline{\underline{\varepsilon}}^{el} \tag{3.6}$$

where A_{ex} is the exchange stiffness of the material, $\underline{\underline{\varepsilon}}^{el}$ is the elastic strain tensor, and C is the elastic stiffness tensor of the material. In a magnetoelastic material, the elastic strain tensor can be written as the difference of the total strain $\left(\underline{\underline{\varepsilon}}\right)$ and the magnetic strain $\left(\underline{\underline{\varepsilon}}^{m}\right)$ components such that $\underline{\underline{\varepsilon}}^{el} = \underline{\underline{\varepsilon}} - \underline{\underline{\varepsilon}}^{m}$ since the magnetic moments and the displacements are coupled. The magnetic strain components are given by Equation 3.7 for isotropic materials,

$$\left(\varepsilon_{ij}\right)^m = \begin{pmatrix} \frac{-B_1}{c_{11}-c_{12}}\left(m_1^2-\frac{1}{3}\right) & \frac{-B_2}{c_{44}}m_1m_2 & \frac{-B_2}{c_{44}}m_1m_3 \\ \frac{-B_2}{c_{44}}m_1m_2 & \frac{-B_1}{c_{11}-c_{12}}\left(m_2^2-\frac{1}{3}\right) & \frac{-B_2}{c_{44}}m_2m_3 \\ \frac{-B_2}{c_{44}}m_1m_3 & \frac{-B_2}{c_{44}}m_2m_3 & \frac{-B_1}{c_{11}-c_{12}}\left(m_3^2-\frac{1}{3}\right) \end{pmatrix} \quad (3.7)$$

where B_1 and B_2 are the magnetoelastic coefficients of the magnetostrictive material[90]. If the elastic stiffness constants of a material are not given, they can be related to the Young's Modulus (E) and Poisson's Ratio (ν) of that material as summarized in Equations 3.8-3.10[111],

$$c_{11} = \frac{E(1-\nu)}{(1+\nu)(1-2\nu)} \quad (3.8)$$

$$c_{12} = \frac{E\nu}{(1+\nu)(1-2\nu)} \quad (3.9)$$

$$c_{44} = \frac{c_{11}-c_{12}}{2} = \frac{E}{2(1+\nu)} \quad (3.10)$$

b. Micromagnetics Simulations to Obtain Preliminary Designs

Previous simulations of a magnetic tunnel junction described in the literature indicated that positioning side magnetic elements can help reduce the energy needed to produce magnetization reorientation in the central element; however, no size ranges were provided[112].

Here, initial values of geometric parameters for a three-ellipse design were obtained using the conventional micromagnetics code MuMax. The geometry is defined in Figure 3.2a. The major and minor axes of the three ellipses, a_0, b_0, a_1 and b_1 and the angles φ and θ were varied to obtain geometries in which the magnetization of the outer ellipses would drive magnetization rotation in the inner ellipse. In our geometry sweep, the aspect ratio (AR) of the outer ellipses was fixed at 1.5 since prior simulation experience indicated that ellipses of this AR can be reoriented using

ballistic switching. A smaller AR of 1.3 was selected for the inner ellipse in hopes of increasing the possibility of rotation with successful magnetization switching of the outer ellipses. With these fixed ARs of each ellipse, simulations were run in which a_0 varied between 75nm to 115nm at increments of 10 nm and a_1 varied between 55 nm to 85 nm, also with increments of 10 nm. The angles φ and θ were varied between 20° to 80° in increments of 10° and 30° to 75° in increments of 15°, respectively. Figure 3.1 displays results from one of these simulations in which the magnetization of the outer ellipses was able to drive reorientation of the magnetization of the inner ellipse. For this simulation, the magnetization in the inner ellipse was initialized in the positive y-direction and the magnetizations in the outer ellipses were initialized along their major axes at 45°. The micromagnetics code was then run to obtain the stable magnetization state. The equilibrium magnetization state of this system is shown in Figure 3.2b. The magnetization in the outer ellipses was then reinitialized and held fixed at -45° (3.2c) and the micromagnetics code was run again to obtain the stable equilibrium state. The desired result was the 180° magnetization rotation in the central ellipse shown (3.2d).

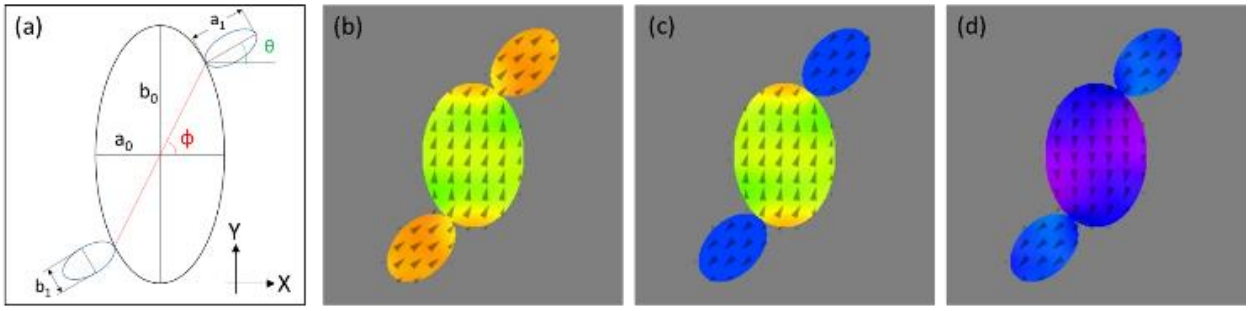

Figure 3.2 (a) Example geometry of the three-ellipse design **(b)** Magnetization configuration of the three-ellipse design after 1 ns using a conventional micromagnetics code. **(c)** Magnetization in the outer ellipses was switched 180°. **(d)** The final configuration indicates 180° magnetization switching in the inner ellipse.

The desired 180^o rotation of the inner ellipse was achieved with the parameters listed above when φ was between 30^o and 70^o and θ was between 30^o and 60^o. Only one geometry was selected to study ballistic switching effects in this three ellipse design to simplify the computation time. This geometry was selected based on fabrication capabilities of electron beam (e-beam) lithography processes as opposed to an optimized geometry. Ellipses with a short axis of 50 nm with a tolerance of ±5 nm can be achieved with e-beam patterning. For this reason, the shortest axis (b_1) was selected to be 50 nm. Since the success of magnetization reorientation also depends on single domain magnetization states, the largest CoFeB dimension was chosen to be approximately 130 nm. Above 130nm, CoFeB disks have the potential to break into multiple domains or form a magnetic vortex. With these considerations, the final dimensions of the inner and outer ellipses were a_0 = 95 nm, b_0 = 125 nm, a_1 = 75 nm, and b_1 = 50 nm. Each ellipse was 4nm thick to produce in-plane magnetization of each CoFeB ellipse. The angles φ = 70^o and θ = 45^o for the outer ellipses were selected to allow ample space to position electrodes needed to generate strain for future fabrication of the device.

Another challenging aspect of the design to achieve with current fabrication capabilities is three ellipses in contact. E-beam lithography resolutions as low as 10 nm with a tolerance of ±2 nm can be achieved with further processing steps, these include processing at low temperatures (~2^{o}C)[113], [114]. For this reason, a separation distance of 15 nm between any two ellipses was incorporated into the design to account for fabrication tolerances. Only 15 nm spacing was considered for modeling purposes to allow for the smallest geometry in the model and to reduce the run time of each simulation.

Next, strain-mediated ballistic switching was simulated using the conventional micromagnetics code that does not directly include magnetoelastic energy terms. The effects of mechanical strains were modeled indirectly by applying time varying uniaxial anisotropies within each ellipse. Strains were converted to magnetic anisotropies using $K_u = 1.5\lambda_s E(\varepsilon_x - \varepsilon_y)$ for implementation in the micromagnetics software[103]. K_u is the uniaxial anisotropy constant, E is the Young's Modulus of the material, and $(\varepsilon_x - \varepsilon_y)$ represents the average in-plane strain of each ellipse. The Young's Modulus of CoFeB used in this simulation was E = 160 GPa[115]. In previous models of Ni/PZT multiferroic heterostructures with perpendicular magnetization reversal, large and unrealistic biaxial strains of up 13,000 ppm in the 100 nm PZT substrate were used to drive magnetization reorientation[116]. In this study, we applied strains as high as 5000 ppm along the minor axis of each outer ellipse to induce ballistic switching in these ellipses. This will need to be further reduced if PZT is used as the piezoelectric layer, but this strain level can be achieved with single crystal PMN-PT[117]. This preliminary geometry was next assessed using the fully coupled finite element model.

c. Fully-Coupled Finite Element Simulations

The fully-coupled model, implemented in COMSOL Multiphysics, was used to assess the effects of strain and magnetization gradients on magnetization dynamics. The model was developed by Liang et al. and has been used to design various multiferroic devices[66], [98], [106], [108], [115]. To ensure the magnetization dynamics behavior was properly captured in this model implementation, a test case from the conventional micromagnetics software was considered. In this simple test case, a magnetic rectangular bar is initialized in its equilibrium state by applying and slowly reducing a saturating field to zero. Fields of magnitude sufficient to reverse the

magnetization of the rectangle are applied to this state and the time evolution of the magnetization as the system moves towards a new equilibrium. A comparison of the magnetization dynamics from the micromagnetics software and the in-house developed finite element model using the weak form found in Chapter 2 is given in Figure 3.3. The magnetization dynamics between the two models demonstrates good agreement ensuring that this finite element model can accurately predict magnetization behavior in a ferromagnetic material.

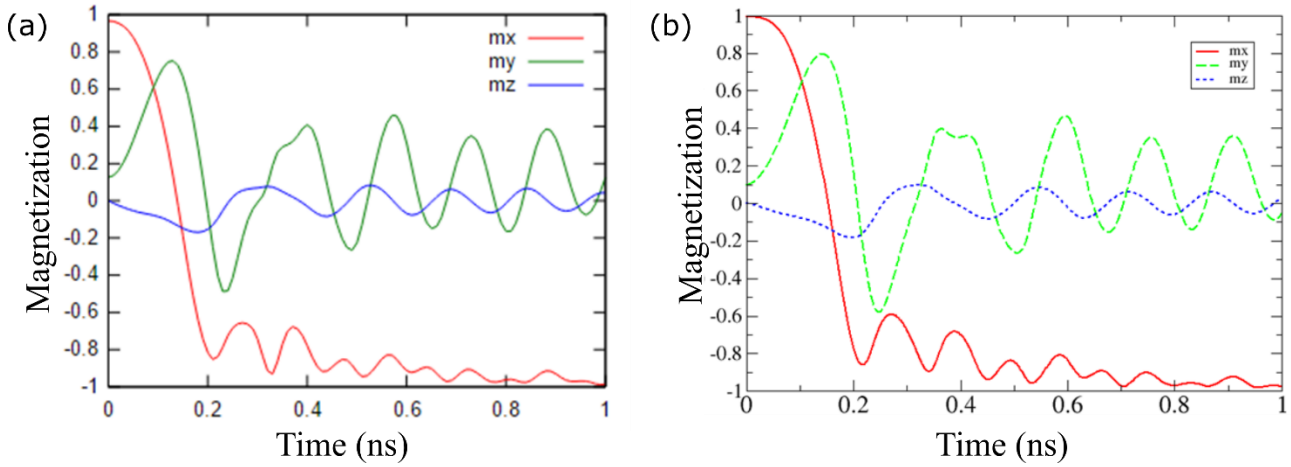

Figure 3.3 (a) Magnetization dynamics of test case generated for the conventional micromagnetics software and **(b)** corresponding magnetization dynamics predicted from weak form implementation in finite element model demonstrates nearly identical response.

The comparison of the two models suggests the finite element implementation can calculate proper magnetization dynamics and coupled models can be built with confidence in predicting the behavior of devices. Simulations were performed with a geometry that included the piezoelectric substrate and the electrodes. In this geometry, the three CoFeB ellipses were positioned on a 700nm x 700nm x 500nm PZT-5H substrate. The Gilbert damping constant, magnetic saturation, exchange constant, elastic constants, and magnetostrictive coefficient of CoFeB used in the model

were: α = 0.01[118]–[120], M_s = 1e6 [A/m][107], A_{ex} = 1.5e-11 [J/m][107], c_{11} = 2.8e11 [N/m^2][107], c_{12} = 1.4e11 [N/m^2][107], c_{44} = 0.7e11 [N/m^2][107], λ_s = 110e-6[121], [122].

A pair of electrodes was placed on either side of each smaller ellipse, with 250 nm separation between each electrode. The only requirement for each electrode is that the side adjacent to the ellipse must be of roughly equal dimension of the ellipse to allow for uniform strain distribution on the bottom surface of the ellipse. Previous fabrication experience suggests trapezoidal electrodes are better suited for device patterning[123]. The final electrode geometry selected were trapezoids of dimensions l_1 = 75 nm, l_2 = 150 nm, and h = 50 nm. Figure 3.4b is a top view of the geometry used in the fully-coupled finite element model.

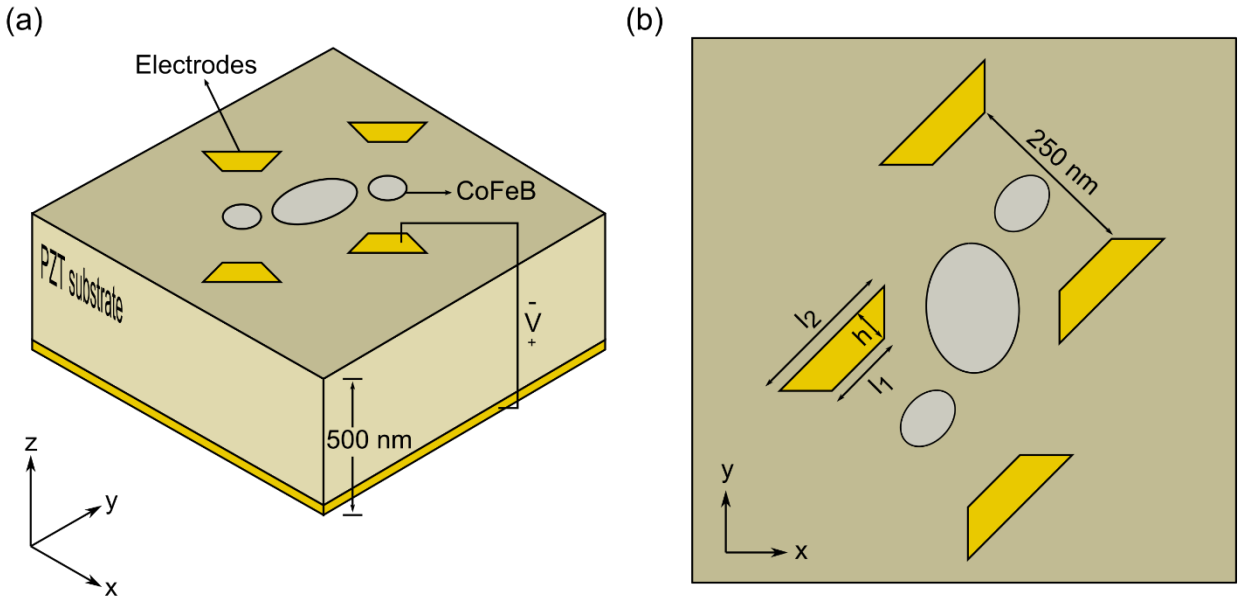

Figure 3.4 (a) Isometric view **(b)** Top view of three ellipse configuration and electrodes used in fully-coupled finite element simulations.

Low reflecting boundary conditions were applied to the four edges of the PZT substrate to simulate infinite width. This boundary condition eliminated wave reflections from the side walls of the substrate. The top of the substrate was free to displace in the z-direction. The displacements in the $x, y,$ and z-directions of the bottom surface were fixed, mathematically represented as $u_1 = u_2 = u_3 = 0$. This mechanical boundary condition allows for wave reflections in the z-direction which are representative of physical reflections in a thin film substrate. However, the effect of these reflections on the magnetization dynamics is predicted to be insignificant due to the demagnetization energy of each ellipse which causes magnetization dynamics to remain mostly in-plane. The bottom surface of the substrate was also the ground plane. Voltage was applied to the trapezoidal electrodes on the top surface. A tetrahedral mesh was used for the PZT substrate. The magnetic elements used a swept triangular mesh. The largest mesh size in the magnetic domain was set according to the exchange length of CoFeB which is 4.9 nm. The exchange length is given by $l_{ex} = \sqrt{\frac{2A_{ex}}{\mu_0 M_S^2}}$ [124]. Thus, the maximum mesh size used in the model was 5 nm to capture the exchange effects.

The magnetization in each ellipse was initially aligned in the positive y-direction and allowed to relax to steady state for 1ns. A static voltage of 7.3 V was then applied to all electrodes and the magnetization dynamics of the outer ellipses was analyzed to obtain an appropriate pulse width. The voltage was released when the y-component of magnetization was between -0.7 to -1.0 and the corresponding x-component of magnetization was between -0.2 and -0.5 to allow the highest possibility of 180^o in-plane switching. For the applied voltage of 7.3 V the appropriate pulse width was found to be 0.22 ns to produce switching of the outer ellipses. The simulation was then run with a series of 7.3 V pulses applied to each electrode. This voltage magnitude is well below the

breakdown electric field of 25 MV/m for PZT thin films[107]. The pulse of 0.22ns was applied at an interval of 4ns between each pulse to achieve 360^{o} rotation. The pulse produced an average tensile strain along the minor axis of 4,400ppm in the outer ellipses and 1,800ppm in the inner ellipse. Although previous devices using thin film PZT have been proposed using larger strains values, strains above 1,800ppm in thin film PZT are not possible to achieve[116]. Other piezoelectric substrates must be considered for fabrication and testing of this device. However, for a proof of concept of a deterministic magnetization rotation, we considered strains as high at 5,000 ppm. Figure 3.5 illustrates the input voltage pulse applied to the electrodes and the corresponding in-plane strain it produced in each ellipse.

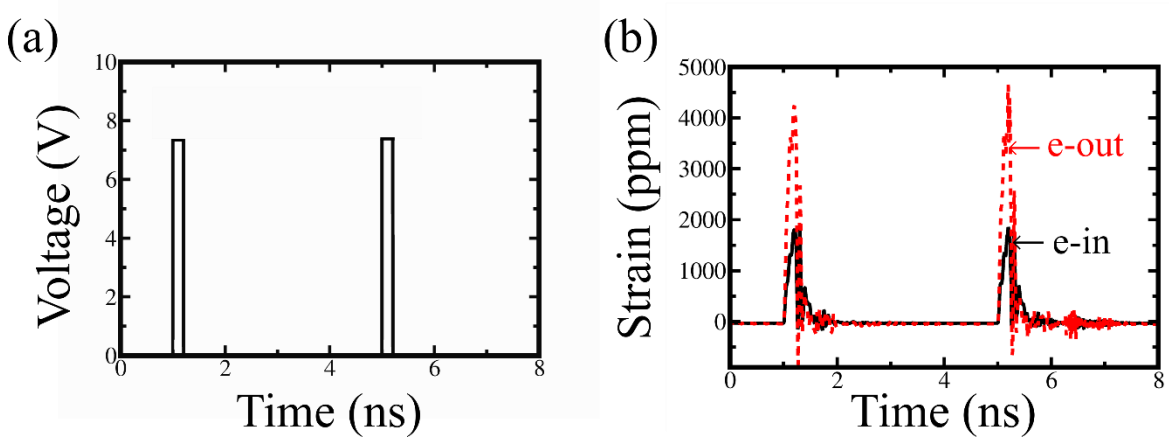

Figure 3.5 (a) Input voltage pulses **(b)** Voltage pulse induced average strain response of inner and outer ellipses.

3.3 Results and Discussion

The strain-induced magnetic response of the three ellipse heterostructure is discussed below. First, the temporal response predicted by the conventional micromagnetics formulation is given. Second, the results of the fully-coupled model are presented. The differences in the device behavior predicted by the two different modeling approaches is then discussed.

The conventional micromagnetics simulation did not produce 180º ballistic switching of the outer ellipses when they were subjected to a 1 ns duration change in magnetic anisotropy equivalent to that produced by the strain pulse in the fully-coupled model. Consequently, the magnetization of the inner ellipse could not be rotated 360º without reinitializing the magnetization in the outer ellipses. The magnetization of the outer ellipses rotated a maximum of 115º with respect to the horizontal x-axis in response to the anisotropy change while the inner ellipse's magnetization rotated 50º clockwise. For full 180º switching of the outer ellipses, the magnetization must rotate past 135º with the application of strain. These results indicate that uniaxial strain induced anisotropy changes could not overcome the dipole coupling between the three ellipses that favors parallel alignment of their magnetization.

In the fully-coupled model, 360º magnetization switching of the inner ellipse was achieved by two consecutive 180º ballistic switches of the two outer ellipses as seen in Figures 3.6a and 3.6b. The magnetization of the inner ellipse completed its first 180º switch (1 to -1) in 1.6 ns while the outer ellipses achieved 180º reorientation in 1.3 ns. Given a wave speed of approximately 4000m/s in PZT-5H, reorientation of the inner ellipse is expected to begin approximately 30 ps after the initial voltage is applied. Figure 3.6b indicates that the magnetization of the outer ellipses begin to rotate at t = 1.03 ns while the magnetization of the inner ellipse starts rotating at t = 1.08 ns. This difference indicates magnetic reorientation of the inner ellipse was driven by the effective field (i.e., dipole coupling) produced from the magnetization configuration of the outer ellipses. Hence, when the outer ellipses are switched ballistically, magnetic reorientation of the inner ellipse occurs in part due to the effective field of the side ellipses. This effective field is a result of the magnetization distribution within each ellipse. The internal magnetization and the effective magnetic field it produces is dependent on the aspect ratio of each ellipse. The effective field of

each ellipse element was approximated using the field of a magnetic dipole. By simplifying the three ellipse design to a three dipole system, the torque exerted by the outer ellipses results in counterclockwise rotation of the inner ellipse's magnetization.

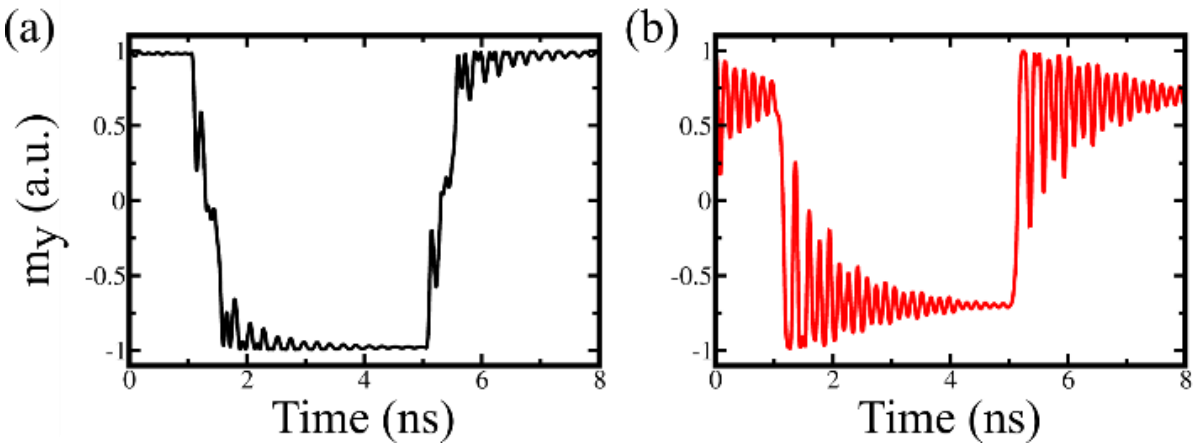

Figure 3.6 (a) m_y of the inner ellipse demonstrating 360º ballistic switching in fully-coupled model. **(b)** m_y of magnetization in one of the outer ellipses.

The difference in predicted behavior between the two models is due to non-uniform strain distributions that are captured only by the fully-coupled model. In the simplified micromagnetics model, the uniaxial anisotropy within the ellipses fails to capture these strain gradients. Consequently 360º magnetic switching of the inner ellipse is demonstrated by the fully-coupled model, but not found using the micromagnetics simulation. In the fully coupled model, all three ellipses are subjected to time dependent compressive and tensile strains. These findings are consistent with results of a micromagnetics model by Ostler, T. et al.[125] of Galfenol film on a piezoelectric substrate. Strain gradients applied to the film were successfully able to move and reverse the vortex core in Galfenol films which otherwise remained stationary with voltage inputs that produced no strain gradients. The non-uniform strain distribution is the result of the interaction of mechanical waves within the substrate that arise from having two pairs of electrodes actuated

simultaneously. The non-uniform distribution creates multiple hard and easy axes of magnetization inside the inner ellipse which makes rotations easier. This variation in strain helps drive magnetization rotation of the inner ellipse after reorientation in the smaller ellipses.

To confirm the magnetization reorientation is a result of the strain gradients and not solely the bidirectional magnetoelastic coupled model, a final simulation was run where the Young's Modulus, *E,* of the magnetic elements was reduced by a factor of 40 to minimize any bidirectional coupling effects. The simulation was set to run for 1 pulse to confirm magnetization switching is achievable. The results of this model are presented in Figure 3.7. Successful 180° reorientation of the y-component of magnetization is demonstrated in both the inner 3.7a and outer 3.7b ellipses.

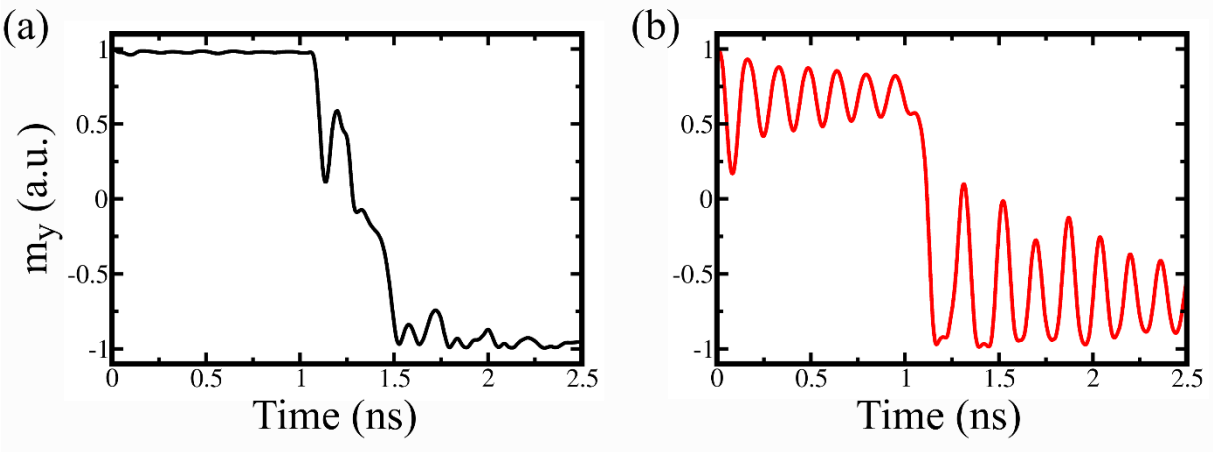

Figure 3.7 (a) m_y of the inner ellipse demonstrating in fully-coupled model for low *E*. **(b)** m_y of magnetization in one of the outer ellipses with low *E*.

The energy consumption for each electrode is evaluated as the energy stored in the PZT capacitor using a relative dielectric constant of $\varepsilon_r = 1704$. Each electrode in this design consumes approximately 4.52 fJ per pulse. With four electrodes in the design, the total energy consumed per switch it 18.1 fJ and the area energy consumption (the total energy divided by the total area of the

electrodes) is 0.8 J/m^2. This is approximately one order of magnitude lower than multiferroic heterostructures using $BiFeO_3$ films[107], [126]. With optimization of the geometry of the three ellipses and the electrode design, these energy requirements could be further reduced.

3.4 Conclusion and Outlook

A conventional micromagnetics simulation and a fully-coupled finite element model was used to simulate a three ellipse heterostructure capable of 360^o deterministic magnetization rotation in a new multiferroic heterostructure. The heterostructure was composed of three CoFeB nanoellipses layered on top of a PZT thin film. . In the micromagnetics model, the strain in each was simulated as a uniaxial anisotropy along the minor axis of each ellipse. The outer ellipses and larger ellipse were simulated with uniaxial strains of 5,000 ppm and 1,800 ppm strain respectively. In this simplified simulation, the magnetization within the three ellipses did not rotate 360^o. Instead, the magnetization stayed in its original configuration and no rotations were observed in the structure.

In the fully-coupled model, the magnetization of the larger ellipse underwent 360^o counterclockwise rotation after ballistic switching of the outer ellipses. The magnetization of the outer ellipses was switched using a 7.3 V pulse applied for 0.22 ns to cause 180^o rotation. Then an identical second pulse was applied to create full 360^o rotation. The voltage pulses produced a tensile strain along the minor axis of each ellipse. The larger and smaller ellipses experienced strains of approximately 1,800 ppm and 4,400 ppm respectively. This demonstrates the necessity of having a fully-coupled simulation to accurately predict the behavior of multiferroic heterostructures, especially in the dynamic regime. The strain gradients that occur in the physical device are not captured by the simplified approximation of the micromagnetics model. The fully-

coupled finite element model better predicts the magnetization dynamics in multiferroic heterostructures.

Although this proof of concept device can overcome some hurdles with strain-mediated multiferroic heterostructures, challenges still exist. As mentioned earlier, the high strain values needed to switch the outer ellipses is not achievable in PZT and different piezoelectric materials must be explored in hopes of implementing this model for device fabrication. Additionally, although deterministic switching is achieved by this three ellipse layout, the use of ballistic switching for the outer ellipses could still present challenges since the voltage pulse is highly dependent on the magnetization dynamics of the structure. The magnetization dynamics itself can be sensitive to external factors of the applied voltage and materials properties of the structure. Results of further studies are presented in Chapters 4 and 5 to address some of these concerns.

IV. Modeling the Effects of Strain Profiles and Defects on Precessional Magnetic Switching in Multiferroic Heterostructures

4.1 Introduction

The successful operation of memory, logic, and cell sorting devices depends on the control of individual magnetic islands within an array of magnets[127]. Individual in-plane magnetization control of 500 μm Ni disks was first demonstrated using the novel concept of patterned electrodes on a PZT substrate[66]. Substrate clamping was overcome using four patterned electrodes around a Ni magnet to allow for uniform localized strain on bulk film PZT to be applied to a thin-film Ni magnet in the center. A series of static voltages applied to this set of electrodes resulted in 180^{o} in-plane magnetization switching. The technique of patterned electrodes scales well for nanoscale devices and successful 180^{o} in-plane magnetization reorientation using four electrodes was also demonstrated for Co nanoellipses (~300 nm)[105]. Although the four electrode pattern achieves 180^{o} switching, there is a need for designs using less electrodes in order to increase the density of memory and cell sorting elements while simultaneously lowering the power consumption. One method to reduce the number of required electrodes relies on the magnetization dynamics (i.e., precessional motion) of the element's magnetization in which precisely timed strain pulses can cause 180^{o} magnetic reorientation.

This control method, which utilizes magnetization dynamics for magnetic reorientation, is termed ballistic switching. In this scheme the magnetization undergoes damped precession about the direction of an effective magnetic field which is generated from high frequency inputs of an applied strain pulse. For example, Li et al.[106] used ballistic switching in strain-mediated heterostructures and simulated successful magnetization reorientation 180^{o} out-of-plane through a

strain pulse. Ballistic switching was extended by Peng et al.[107] to in-plane 180° magnetization switching using two electrodes and a single short strain pulse. A finite element simulation was used to demonstrate strain-mediated ballistic switching in a single CoFeB nanoellipse on a PZT thin film. The magnetization in the ellipse was initially aligned along the positive x-axis ($m_x = 1$), parallel to the major axis of the ellipse. Two electrodes placed near the edge of the minor axis of the ellipse and located along the y-axis were actuated and produced approximately 1100 ppm in-plane tensile strain in the y-direction of the ellipse. The applied strain caused the y-axis to become the new magnetic easy axis for a CoFeB element resulting in magnetic precession about this axis. The voltage induced strain was released when m_x was between 0 and -1. After the strain was removed, the y-axis was no longer an easy axis and magnetization favored alignment along the negative x-direction resulting in a 180° switch.

Although simulation can provide important insight to device behavior, experimental results often differ from modeling predictions. For multiferroic heterostructures, this was evident in the experimentally measured behavior of an array of Ni rings patterned on top of a PMN-PT substrate. For this study, a coupled linear piezoelectric, micromagnetics, and elastodynamics finite element model (fully-coupled) predicts 360° magnetization rotation of a magnetic onion state[117]. However, experimentally, this rotation was only observed in a small number of the patterned rings[128]. Since the coupled models assume no imperfections in the nanostructures, it was suggested that geometric defects resulting from fabrication may have impeded the magnetic reorientation of the Ni rings. Other magnetic structures also have magnetization behavior that is affected by defects. Specifically, Nakatani et al.[129] used numerical modeling to demonstrate a higher magnetic domain wall velocity in a magnetic nanowire with rough edges/defects when compared to a perfectly smooth nanowire counterpart. Leliaert et al.[130] expanded on the study

of defects and magnetization behavior to demonstrate that in the presence of defects in a nanowire, the domain wall configuration itself changes. When no defects are present in a nanowire, a single domain wall with a vortex configuration will move and transform into a transverse domain wall under the application of an applied field or current. However, with defects present, the vortex configuration will remain in the presence of an applied field, hindering any transverse domain wall formation[130], [131].

This chapter explores the results of various strain application rates (ramps), strain amplitudes, and geometric defects on the voltage-induced, strain-driven magnetization dynamics of a single, amorphous CoFeB nanoellipse on a PZT thin film. This geometry was modelled using both a fully-coupled finite element code and a purely micromagnetics simulation. The fully-coupled finite element model refers to one which couples linear piezoelectric, micromagnetics, and elastodynamics equations in one code. Although the prospect of ballistic switching for magnetic device applications is promising, little information exists regarding how changes in the input voltage to the device can affect its magnetization dynamics. Fluctuations in input voltage, and resulting strain, may interfere with device performance which relies on magnetization behavior in response to input signals. Modeling of geometric defects within a magnetic element was also addressed to better understand how single domain magnetization dynamics may be affected by the presence of imperfections that can occur in the fabrication process. The results of these simulations provide a step toward predicting device behavior of multiferroic devices and provide further insight into the restrictions of modeling methods applied to the design of current multiferroic heterostructures.

4.2 Simulation Details

a. Micromagnetics Theory Overview

Micromagnetics theory is used to obtain the spatial distribution of magnetization within magnetic materials at submicron length-scales[108]. The motion of each magnetic moment, represented by the unit vector $\underline{m}$, is governed by the Landau-Lifshitz-Gilbert (LLG) Equation, given in Equation 4.1.

$$\frac{\partial \underline{m}}{\partial t} = -\mu_0 \gamma \left(\underline{m} \times \underline{H}_{eff}\right) + \alpha \left(\underline{m} \times \frac{\partial \underline{m}}{\partial t}\right) \tag{4.1}$$

Here, μ_0 is the permeability of free space, γ is the gyromagnetic ratio, α is the Gilbert damping constant and $\partial \underline{m}/\partial t$ represents the time (t) derivative of the unit magnetic moment vector, $\underline{m}$. The effective magnetic field ($\underline{H}_{eff}$) is the partial derivative of the total magnetization energy (E_{tot}) with respect to magnetic moment. The magnetization energy can be represented by the sum of the energies resulting from an externally applied field (E_{ext}), the exchange interaction (E_{ex}), demagnetization effects (E_d), elastic effects (E_{el}) and magnetocrystalline anisotropy (E_{mca}). The exchange term represents an interaction energy between neighboring magnetic moments that favors parallel alignment within a ferromagnetic material. This effect between neighboring moments acts over short distances denoted as the exchange length (l_{ex}) of the material. The demagnetization energy is associated with the shape of a magnetic element, where physically longer axes correspond to lower energy states. Mathematically, this demagnetization energy is determined from an effective demagnetization field ($\underline{H}_d$) using the magnetic scalar potential, φ, where $\underline{H}_d = -\nabla\varphi$. The elastic energy in the multiferroic heterostructure is associated with strain changes in the system. The magnetocrystalline anisotropy (MCA) energy is related to the crystal

structure of the material and determines which crystallographic directions are magnetically easy or hard[90]. For amorphous CoFeB thin films the magnetocrystalline contribution is negligible and is not included in the magnetic energy of the device[107], [109], [110]. Hence, the remaining energy equations are summarized in Equations 4.2-4.5.

$$E_{ext} = -\mu_0 M_s(\underline{m} \cdot \underline{H}_{ext}) \tag{4.2}$$

$$E_{ex} = A_{ex}\left(\nabla \underline{m}\right)^2 \tag{4.3}$$

$$E_d = -\frac{\mu_0 M_s}{2}(\underline{m} \cdot \underline{H}_d) \tag{4.4}$$

$$E_{el} = \frac{1}{2}\underline{\underline{\varepsilon}}^{el} : \underline{\underline{\underline{\underline{C}}}} : \underline{\underline{\varepsilon}}^{el} \tag{4.5}$$

A_{ex} is the exchange stiffness of the material, $\underline{\underline{\varepsilon}}^{el}$ is the elastic strain tensor, and $\underline{\underline{\underline{\underline{C}}}}$ is the elastic stiffness tensor of the material. As a result of coupling between the magnetic moments and displacements in a magnetoelastic material, the elastic strain tensor can be written as the difference of the total strain $\left(\underline{\underline{\varepsilon}}\right)$ and the magnetic strain $\left(\underline{\underline{\varepsilon}}^m\right)$ components such that $\underline{\underline{\varepsilon}}^{el} = \underline{\underline{\varepsilon}} - \underline{\underline{\varepsilon}}^m$. For isotropic materials, the magnetic strain components are given by Equation 4.6:

$$\left(\varepsilon_{ij}\right)^m = \begin{pmatrix} \frac{3}{2}\lambda_s\left(m_1^2 - \frac{1}{3}\right) & \frac{3}{2}\lambda_s m_1 m_2 & \frac{3}{2}\lambda_s m_1 m_3 \\ \frac{3}{2}\lambda_s m_1 m_2 & \frac{3}{2}\lambda_s\left(m_2^2 - \frac{1}{3}\right) & \frac{3}{2}\lambda_s m_2 m_3 \\ \frac{3}{2}\lambda_s m_1 m_3 & \frac{3}{2}\lambda_s m_2 m_3 & \frac{3}{2}\lambda_s\left(m_3^2 - \frac{1}{3}\right) \end{pmatrix} \tag{4.6}$$

where λ_s is the magnetostrictive coefficient of which is a property of the magnetostrictive material[132]. Here m_1, m_2, m_3 represent the three different components of the unit vector, $\underline{m}$, along the three different strain axes, 1,2, and 3, defined for the problem. These components are the

direction cosines of spontaneous magnetization with respect to the strain axes. Additionally, c_{11}, c_{12}, c_{44} are components of the elastic stiffness tensor of the magnetic material. Finally, the equation for the effective field, ($\underline{H}_{eff}$), used in Equation 4.1 is found by taking the partial derivatives of Equations 2-5 with respect to $\underline{m}$, as given in Equation 4.7a,

$$\underline{H}_{eff} = -\frac{1}{\mu_0 M_s}\left(\frac{\partial E_{tot}}{\partial \underline{m}}\right) \tag{4.7a}$$

$$= \underline{H}_{ext} + \underline{H}_{ex} + \underline{H}_{d} + \underline{H}_{me} \tag{4.7b}$$

$$E_{tot} = E_{ext} + E_{ex} + E_{d} + E_{me} \tag{4.7c}$$

where M_s is the saturation magnetization of the material. The derivatives for each energy term was expanded in Chapter 2 Section 3b.

b. Finite Element Model

A fully-coupled finite element model was developed by Liang et al.[108] in which the multiferroic heterostructure was modelled using three sets of equations to define device behavior: 1) linear piezoelectric, 2) elastodynamics and 3) micromagnetics. This coupled model has been used to design various multiferroic devices[69], [98], [106], [115], [117]. The geometry discussed here consists of a single CoFeB nanoellipse (100 nm x 80 nm x 6 nm) positioned between two Au trapezoidal ellipses with a short edge of 100 nm, a long edge of 200 nm, and a height of 80 nm. The shorter edge of the trapezoidal electrodes was positioned 100 nm above and below the edge of the ellipse, parallel to the major axis of the ellipse. The electrodes and ellipse were centered on an 800 nm x 800 nm x 500 nm PZT thin film substrate. The top view of the geometry used in the fully-coupled model is shown in Figure 4.1a.

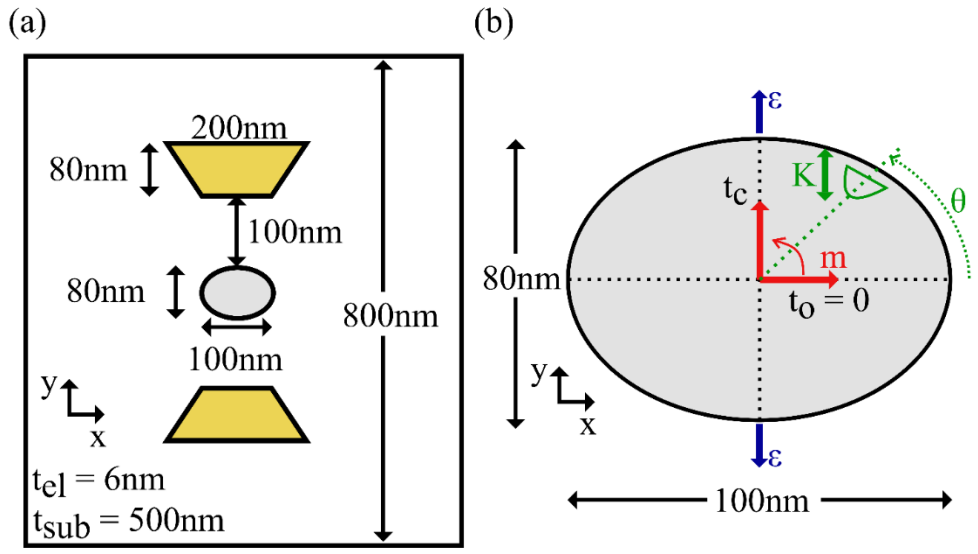

Figure 4.1 (a) Layout of ballistic switching system showing relative location of magnetic CoFeB element with respect to electrodes for fully-coupled model. **(b)** Diagram showing motion of ellipse magnetization in response to application of strain (uniform uniaxial magnetic anisotropy) in fully-coupled (micromagnetics) model from initial state at $\theta = 0^0$ when the time is t_o to when $\theta = 90^o$ at crossover time t_c.

Roller boundary conditions were applied to all side faces of the PZT substrate to simulate a substrate of infinite width. The top surface of the PZT substrate was mechanically free to displace in the x, y, and z- (out-of-plane) directions. Here the x, y, and z-axes represent the three different coordinate axes -- 1, 2, and 3. The bottom of the substrate was fixed, so that all displacements on this surface were set to zero. The bottom surface was also the ground plane of the applied voltage. Voltage was applied to the electrodes on the top surface. A tetrahedral mesh was used on the PZT substrate. The magnetic element was swept with a triangular mesh where each element was set to be a maximum of 5 nm. This upper limit was set using the exchange length, $l_{ex} = \sqrt{2A_{ex}/\mu_0 M_s^2}$, of the material which was found to be 4.9 nm[124]. The Gilbert damping constant, saturation magnetization, exchange constant, elastic constants, and magnetostrictive coefficient of CoFeB used in the model were: α = 0.01[118]–[120], M_s = 1e6 [A/m][107], A_{ex} = 1.5e-11 [J/m][107], c_{11}

= 2.8e11 [N/m^2][107], c_{12} = 1.4e11 [N/m^2][107], c_{44} = 0.7e11 [N/m^2][107], and λ_s = 110e-6[121], [122].

The magnetization of each ellipse was initially aligned along the positive x-direction and allowed to relax for 1 ns to reach an initial equilibrium state. In the fully-coupled model, applying a voltage to the electrodes patterned on a piezoelectric substrate results in biaxial strain within the ellipse-substrate interface such that principle tension and compression axes are directed along the y - and x-axes, respectively. When voltage is applied on the electrodes, the magnetoelastic effects allow the magnetization to rotate toward the y-axis (i.e., the minor axis of the ellipse) since CoFeB is negative magnetostrictive and will align along any axis of compression. Due to precessional motion of magnetization, the unit vectors will oscillate about the y-axis for few picoseconds before settling to the new equilibrium state. Since the ellipse is symmetric, clockwise (cw) or counterclockwise (ccw) motion are equally possible. Figure 4.1b illustrates ccw motion of the magnetization from its initial orientation when $\theta = 0^o$ at $t = 0$ to when $\theta = 90^o$ at $t = t_c$. Here, t_c, is the time required for the magnetization angle θ to first reach ±90^o after the voltage is first applied, which we label as the crossover time. Specifically, when we plot the x-component (m_x) of magnetization vs time, the crossover time is the first time when $m_x = 0$. The crossover time was used to compare the effect of different strain ramps, amplitudes and material defects on the nanoellipse. Table 4.1 summarizes the different voltage amplitudes and resulting strain generated in the substrate for the fully-coupled model.

Table 4.1 Voltage amplitudes and equivalent strain values tested.

Voltage Magnitude (V)	Equivalent Strain (ppm)
0.94	800
1.41	1200
1.88	1600
2.35	2000

A total of 12 simulations were conducted since the four different voltages were applied at three different ramp rates: 1e9 s^{-1}, 1e10 s^{-1}, and 1e11 s^{-1}. Here, the ramp rate refers to the time required to reach the maximum applied voltage. The ramp rate of 1e9 s^{-1} implies it takes 1 ns to reach the maximum voltage from the time the voltage is applied. 1e10 s^{-1} and 1e11 s^{-1} correspond to 0.1 ns and 0.01 ns respectively to reach the maximum applied voltage. Strain values up to 2000 ppm were tested since experimentally it is hard to achieve strain above 2000 ppm in thin film PZT. Figure 4.2a shows that the in-plane mechanical strain of the fully-coupled model, $\varepsilon_{yy} - \varepsilon_{xx}$, does not remain constant once the peak voltage is reached due to mechanical oscillations in the substrate. However, these small oscillations are neglected when modeling strain effects in the purely micromagnetics model as indicated in Figure 4.2b. This model is discussed next.

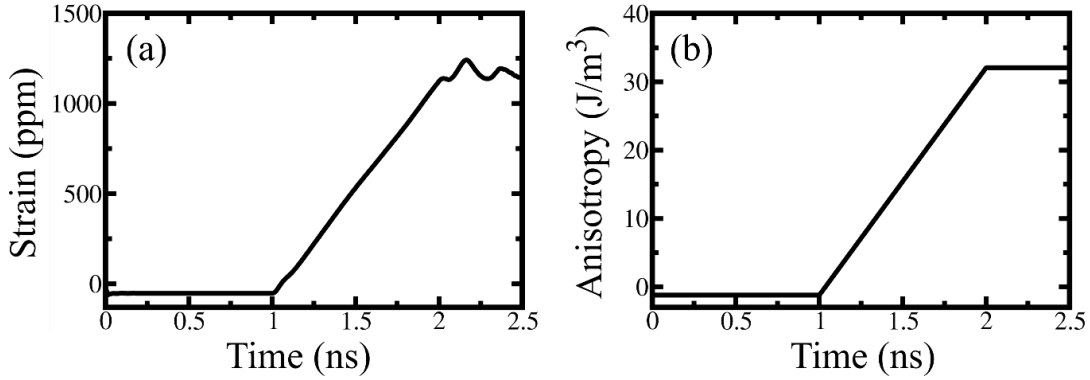

Figure 4.2 (a) Strain profile resulting from applied voltage pulse in fully-coupled model. **(b)** Uniaxial anisotropy pulse used in micromagnetics simulations for approximating the strain pulse of the fully-coupled model.

c. Micromagnetics Model

The micromagnetics model implemented in the open source MuMax3 software has a much faster run time in comparison to the fully-coupled finite element model. For this reason, a second set of simulations was conducted in MuMax3 to compare the predicted crossover times to see if it could be used as a possible design tool for future multiferroic heterostructures. Previous work indicates slight variations in behavior of multiferroic devices in the fully-coupled model and micromagnetics model where the fully-coupled model better predicts experimental results[82]. However, if the two models predict similar crossover time, it is more time efficient to use MuMax3 for device design.

In the purely micromagnetics model, small deformations and a constant uniform strain state in the CoFeB ellipse were assumed[82]. Subsequently, in the micromagnetics formulation, the magnetoelastic effective field was defined by $\underline{H}_{me} = 3\lambda_s Y(\varepsilon_{yy} - \varepsilon_{yy})/M_s$ where Y is the Young's modulus of CoFeB, found to be 160 GPa[115], and $(\varepsilon_{yy} - \varepsilon_{yy})$ is the in-plane strain in the ellipse. The magnetoelastic field, $\underline{H}_{me,}$ is represented by a uniform uniaxial magnetic anisotropy, K, defined as $K = \mu_o \underline{H}_{me} M_s/2$ [103]. Through this formulation, the strains in Table 4.1 were converted to equivalent uniaxial magnetic anisotropies within the CoFeB ellipse for the micromagnetics simulations.

In the micromagnetics model, a 1 nm cubic mesh was used within the magnetic domain since faster run times allowed for smaller meshes. All magnetic material properties remained the same as in the fully-coupled model. Similarly, the magnetization within the CoFeB ellipse was initialized along the positive x-direction and allowed to relax for 1 ns before the ramped uniaxial anisotropy was applied along the minor axis of the ellipse, (i.e. the y-axis). The strain profiles of the fully-

coupled model were represented in the micromagnetics formulation by defining the corresponding time varying uniaxial magnetic anisotropy as seen in Figure 4.2b. The oscillatory behavior of the mechanical strains in the fully coupled model were neglected in the micromagnetics formulation because their relative deviation is small compared to the magnitude of the strain. The crossover time was recorded for these simulations and compared to the fully-coupled model discussed in Section 4.3.

d. Simulation with Defects

One final set of simulations was studied to include geometric defects of the CoFeB ellipse. The simulated defect is illustrated in Figure 4.1b. Specifically, a semicircle 20 nm in radius is defined with the flat edge located 5 nm from the edge of the ellipse at 60^o ccw from the x-axis. In this small semicircular region, the magnetization is fixed in the positive y-direction to simulate the location of a pinned magnetization site arising from fabrication defects. In the fully-coupled model, a strong bias magnetic field of 26 kOe was defined in this region. A corresponding uniform uniaxial magnetic anisotropy was defined in this region in MuMax3. These large pinning field/anisotropy was selected to reflect experimental data in which defects cause magnetization to be completely pinned in a localized region. The geometric defect studies were conducted for the four different strain amplitudes listed in Table 4.1 at an application rate of 1e9 s^{-1}. Only the minimum strain rate was tested since the simulations indicated the largest deviation in crossover time occurred for the slowest ramp. All findings are presented next.

4.3 Results and Discussion

Figure 4.3a shows the strain-induced magnetization dynamics of a single CoFeB ellipse subjected to a maximum strain of 1200 ppm applied at a linear ramp rate of 1 GHz (i.e., 1e9 s^{-1} slope). The

magnetization is initialized along the positive x-direction and, for both models, is shown to be stable before strain is applied at $t = 1$ ns. The magnetization does not rotate instantaneously and begins to rotate after a delay time (t_d). This delay time corresponds to the first time when $m_x \neq 1$. The delay times are $t_d = 2.1$ ns and $t_d = 1.6$ ns for the fully-coupled and micromagnetics models, respectively. The x-component of magnetization for the ellipse reduces to $m_x = 0$ (i.e., 90º of rotation) at the crossover time (t_c). The crossover time is recorded after the voltage is first applied at 1 ns, consequently, if the time it takes $m_x = 0$ is n nanoseconds, the corresponding crossover time, t_c is $n - 1$ nanoseconds. The crossover times for the fully-coupled and micromagnetics models are $t_c = 1.18$ ns and $t_c = 0.8$ ns, respectively. The x-component of magnetization in the fully-coupled model is $m_x = -0.8$ which corresponds to a maximum rotation angle of 143º. The rotation angle is calculated from an initial position of 0º to a final angle calculated by $\tan^{-1}(m_y/m_x)$. Similarly, the micromagnetics model reaches a minimum of $m_x = -0.75$ corresponding to a maximum rotation angle of 138º. Although not shown on the plot, the x-component of magnetization in both models approaches $m_x = 0$ (i.e., 90º) for prolonged run time.

Figure 4.3b shows the crossover times of the fully-coupled and micromagnetics models for all strain rates and strain amplitudes studied. The plot legend distinguishes fully-coupled models with "c" and the micromagnetics studies with "m." The slope of the strain function ramp is denoted numerically. For example, "c9" identifies the results of the fully-coupled model for a strain function ramp with a slope of 1e9 s^{-1} (i.e., 1 GHz). As seen from Figure 4.3b, the crossover times decrease linearly with increasing strain amplitude and decrease with strain rate for the micromagnetics models. Similarly, this trend occurs for the fully-coupled models except for the 1e11 s^{-1} strain rate where t_c increases from 1600 ppm to 2000 ppm. In both models, the crossover

times at 1 GHz are significantly longer than the 10 GHz and 100 GHz strain rates. For the fully-coupled model, t_c at 1 GHz is reduced by 33% when strain is applied at 10 GHz or 100 GHz. For the micromagnetics model, t_c at 1 GHz is reduced by 75% and 79% when strain is applied at 10 GHz and 100 GHz, respectively. For both types of models, there is little difference in crossover times when the strain rate is increased from 10 GHz to 100 GHz, signifying a limiting value as strain rate is increased.

The magnetization dynamics of the CoFeB element are determined by magnetoelastic effects and the ferromagnetic resonance (FMR) frequency of the ellipse. Macroscopically, FMR of a magnetic material is defined as the frequency with which the magnetic spins in a sample will reorient in the direction of a bias magnetic field. Before strain is applied, shape anisotropy maintains the magnetization directed along the x-axis in the initialized positive direction. When strain is applied along the y-axis, an energy well is produced which results in a preferential magnetization direction along the minor axis of the ellipse. The magnetization of the ellipse does not respond instantaneously and this delay in rotation corresponds to the FMR frequency of the ellipse. Although the geometry and material choice are the same in the fully-coupled and micromagnetics models, a difference in FMR is expected because the strain distributions do not match identically. Specifically, time-varying and spatially non-uniform strain distributions are seen in the fully-coupled model while the micromagnetics simulation assumes a constant and spatially uniform strain distribution within the ellipse. Consequently, the delay and crossover times differ between the two models.

The effects of strain on the FMR response for the CoFeB ellipse explain the decreasing trends in crossover times of the fully-coupled and micromagnetics models. The FMR frequency of the ellipse can be approximated using Kittel's equation for a rectangular prism which indicates this

resonance frequency is proportional to the square root of applied strain. Consequently, the resonance frequency increases with strain amplitude and rate. This increase in resonance frequency corresponds to greater rotation rates of the element magnetization thereby decreasing the crossover times. Although the resonance frequency is proportional to the square root of applied strain, the range of strain values chosen is not large enough to show this dependence. Thus, a linear decrease of t_c is found. In contrast to the other strain amplitudes and rates, the 2000 ppm strain amplitude at 100 GHz strain rate case shows non-uniform magnetization states. This indicates incoherent magnetization precession within the ellipse resulting in spatially non-uniform magnetization rotation. Consequently, the ellipse magnetization rotates slower compared to the 1600 ppm at 100 GHz case because the rotation rate is volume averaged over the element. The incoherencies may result from reflections of waves within the element causing different regions of magnetization to rotate differently resulting in increased time for the total volume change of magnetization to rotate towards the y-axis.

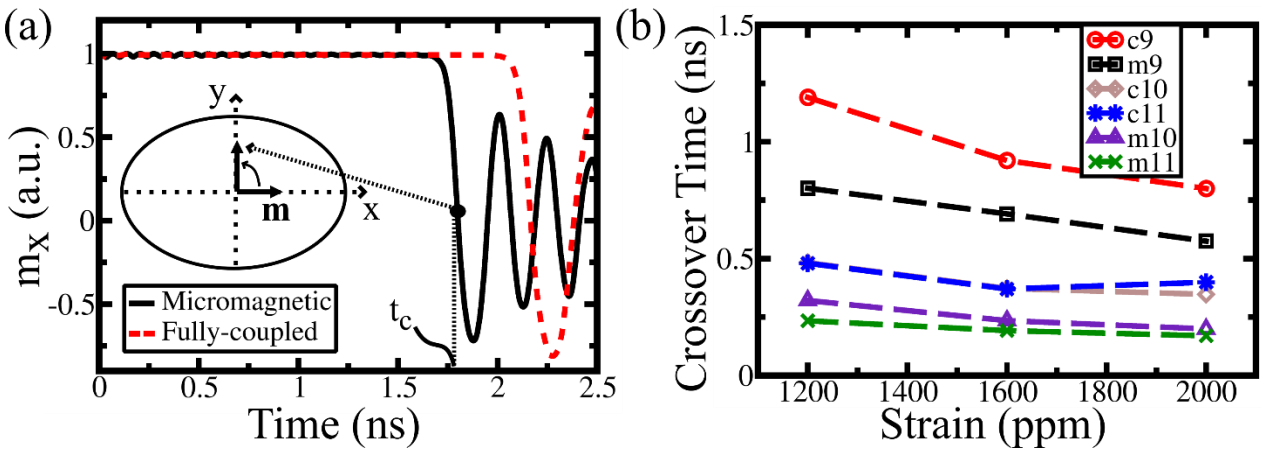

Figure 4.3 (a) x-component of the ellipse magnetization vs. time for an applied strain (anisotropy) at rate of 1e9 s^{-1} and amplitude of 1200 ppm (32 kJ/m^3). (b) Crossover times of the fully-coupled and micromagnetics models for slopes of 1e9 s^{-1}, 1e10 s^{-1}, and 1e11 s^{-1} at strain amplitudes of 1200 ppm, 1600 ppm, and 2000 ppm.

Figure 4.4a shows the strain-induced magnetization dynamics of a single CoFeB ellipse subjected to a maximum strain of 1200 ppm applied at a linear ramp rate of 1 GHz with a defect located at $\theta = 60^{o}$. The x-component of magnetization (m_x) is initialized along the positive x-direction and, for both models, oscillates about an average value below $m_x = 1$. This average value is $m_x = 0.78$ and $m_x = 0.90$ for the fully-coupled and micromagnetics models, respectively. Strain is applied to the ellipse along its minor axis at t = 1 ns. However, the magnetization does not rotate instantaneously and begins to rotate at a delay time $t_d = 1.2$ ns in the fully-coupled simulation. Similarly, m_x rotates at $t_d = 1.15$ ns for the micromagnetics model. The magnetization reaches 90° at $t = 1.7$ ns for the fully-coupled study which corresponds to a crossover time $t_c = 0.7$ ns. Similarly, m_x reaches 90° at $t = 1.4$ ns for the micromagnetics model corresponding to a crossover time t_c = 0.4 ns. The x-component of magnetization in the fully-coupled model reaches a minimum of $m_x = -0.2$ which corresponds to a maximum rotation angle of 100°. Similarly, the minimum value of the micromagnetics model is $m_x = -0.50$ corresponding to a rotation of 120°. Although not shown on the plot, the x-component of magnetization in both models approaches $m_x = 0$ (i.e., 90°) for $t > 2$ ns.

The decreases in crossover times for the ellipse with a defect relative to the ellipse without a defect are caused by changes in local magnetic anisotropy. Specifically, the defect region changes the anisotropy energy and direction in a local region, which has effects on the volume average magnetization through exchange interactions. In particular, the anisotropy within the defect region causes a preferential magnetization direction along the y-axis. As a result, the magnetization located near this area prefers a similar orientation. However, as distance away from the defect region is increased, less influence from the defect region is exerted on the ellipse magnetization. Consequently, the shape anisotropy of the ellipse dictates the magnetization direction at sufficient

distance from the defect area. In contrast, to the results shown in Figure 4.3a, the defect results in an initial equilibrium state with $m_x < 1$ indicating that the magnetization is orientated at a nonzero angle. Thus, a smaller rotation angle is needed for the magnetization to fully rotate to $m_x = 0$ (i.e., 90º). This would result in shorter crossover times for both the fully-coupled and micromagnetics simulations.

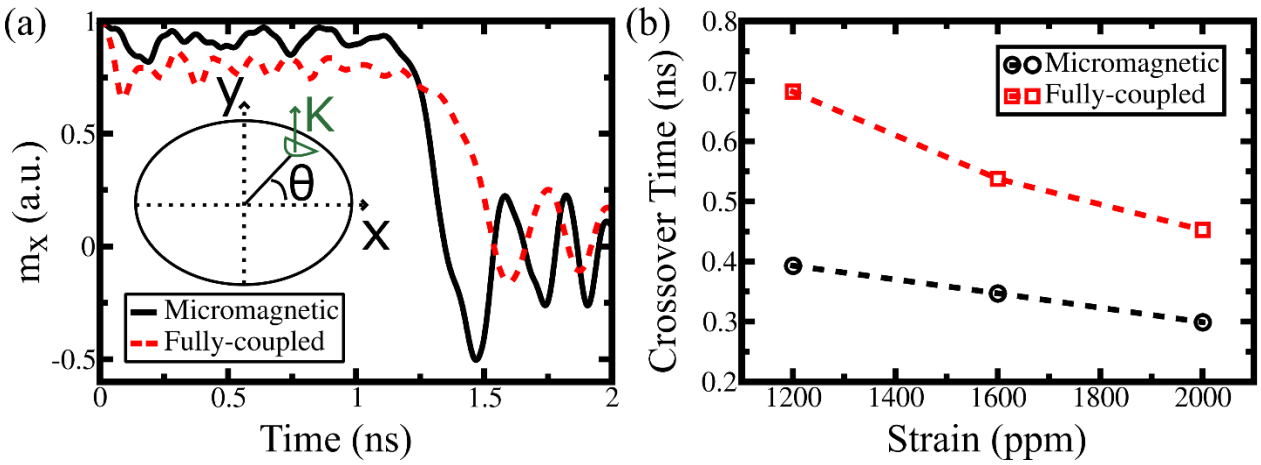

Figure 4.4 (a) x −component of the ellipse magnetization vs. time for an applied strain (anisotropy) at rate of 1e9 s^{-1} and amplitude of 1200 ppm (32 kJ/m^3) for ellipse with defect located at $\theta = 60º$. **(b)** t_c of the fully-coupled and micromagnetics models for slopes of 1e9 s^{-1}, 1e10 s^{-1}, and 1e11 s^{-1} at strain amplitudes of 1200 ppm, 1600 ppm, and 2000 ppm.

4.4 Conclusion and Outlook

In this study, a fully-coupled finite element model and micromagnetics model were used to investigate the effects of strain amplitude and strain rate on the dynamic magnetoelastic response of a CoFeB nanoellipse in a multiferroic heterostructure. The rate for magnetic reorientation of the ellipse was shown to increase with strain amplitude and rate. However, the time needed for the magnetization to rotate 90º at 10 GHz and 100 GHz strain rates varied only slightly, indicating an asymptotic increase in magnetization rotation rate. The presence of a semicircular defect located near the periphery of the ellipse increased the rotation speed and decreased the total rotation angle

as a result of local magnetic anisotropy changes. The results presented here can be used to guide strain-mediated nanomagnetic designs for applications in magnetic memory, nanomotors, or magnetic ratcheting devices.

Chapters 3 and 4 have compared the results of modeling a magnetoelastic material using a fully-coupled model which integrates linear piezoelectric equations with micromagnetics equations verses using a pure micromagnetics solver. Both chapters have indicated different predicted device behavior between the two models. To date, the fully-coupled model has been demonstrated to better predict experimental results of strain-mediated multiferroic materials[82], [83], [133]. Still, using a coupled model with linear piezoelectric equations often leads to optimistic predictions regarding the true device performance. Including material defects in the magnetic domain by using high magnetic anisotropy fields, as discussed in this chapter, is one method to improve current modeling methods of strain-mediated structures. Another approach is to replace the linear piezoelectric equations of the substrate to more realistically model the ferroelectric response of the substrate. This can be achieved through phase-field modeling techniques to capture polarization motion in the ferroelectric substrate and its corresponding effects on the magnetization dynamics. The development and results of this new model are discussed in Chapter 5.

V. Combined Ferroelectric and Micromagnetics Model of a Single Domain Magnetic Element

5.1 Introduction

Recent efforts towards creating nanoscale magnetic devices have propelled the development of strain-mediated multiferroic heterostructures[134]. These heterostructures have several potential applications including magnetic memory and particle manipulation for lab-on-chip technology[103], [106], [115], [117], [134]–[136]. Successful device implementation requires advanced computational modeling techniques that include interactions between ferroelectric and ferromagnetic materials to optimize its behavior. As such, a finite element model was developed that couples two phase field models with evolution of the order parameters governed by the Time-Dependent-Ginzburg-Landau (TDGL) Equation (polarization) and the Landau-Lifshitz-Gilbert (LLG) Equation (magnetization). This enables assessing how the magnetoelastic response of magnetic nanostructures is impacted by non-linear ferroelectric behavior driven by domain wall motion in mechanically-coupled multiferroic composites.

Past research efforts have resulted in a variety of multiferroic heterostructure designs based on the assumption of linear piezoelectric homogeneous strain within the substrate[47], [82], [103], [105], [117], [137]. In these heterostructures, strain generated in the ferroelectric substrate due to the applied voltage alters the magnetization of the ferromagnetic material through magnetostriction effects[138]. The magnetization response is affected by the heterostructure geometry, material properties and the substrate strain induced by the applied voltage[90]. In many experimental demonstration of strain-mediated multiferroic heterostructures, only a small fraction of the magnetic structures fabricated have displayed the predicted magnetization response[128], [139].

For these experimental demonstrations, the strain has often been produced by using relaxor ferroelectric single crystals of [011] cut PMN-xPT or PIN-PMN-PT to obtain an in-plane biaxial tensile-compressive strain state[117], [140]. Le Conte et al.[140] experimentally demonstrated that in these materials the strain response is inhomogeneous at the micron scale. As a result, the magnetization response in patterned Ni squares were heterogeneous across the substrate. Figure 5.1 exhibits the dissimilar strain behavior in the substrate and corresponding effects on the magnetization. This inhomogeneity may be the result of surface roughness, non-uniform charge distribution, or the focus of this chapter: domain structure in the ferroelectric material.

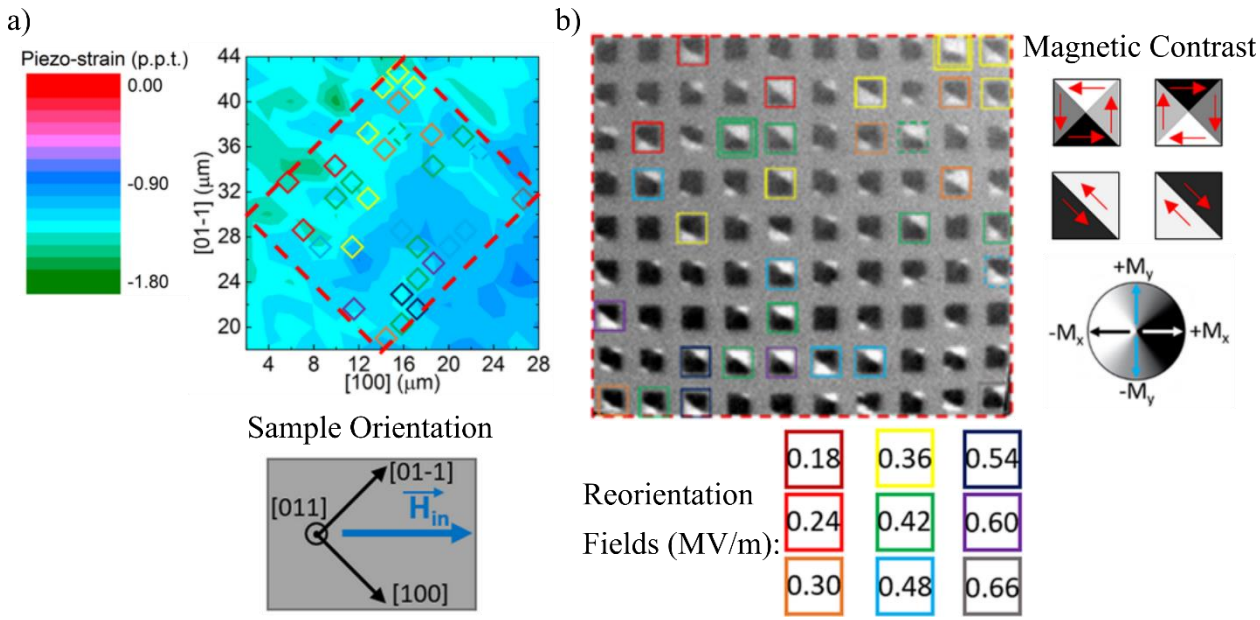

Figure 5.1 (a) the measured strain variation in [011] cut PMN-PT sample using XMCD-PEEM by Lo Conte et al.[140] The measured strain is the in-plane piezo-strain $\varepsilon_{[100]} - \varepsilon_{[01-1]}$ for an applied field of 0.66 MV/m and **(b)** the corresponding magnetization configuration of 1 μm Ni squares in response to the applied electric field. Initially all elements formed the vortex state but the final magnetization configuration is different on different parts of the sample. The color squared represent the field required to switch from the vortex state to the bi-domain magnetization state[140].

The domain structure of the ferroelectric material gives it enhanced piezoelectric properties. Similar to piezoelectric materials discussed in Chapter 1, all ferroelectric materials will

mechanically deform in the presence of an applied electric field. However, in this special class of piezoelectric materials, ferroelectrics have an intrinsic spontaneous electric polarization and associated spontaneous strain in the absence of any field. This intrinsic polarization implies that the change in polarization of the material is not linearly proportional to the applied electric field, instead the relationship is a nonlinear behavior, the difference in the Polarization (P) vs Electric Field (E) of a piezoelectric and ferroelectric material are shown in Figure 5.2.

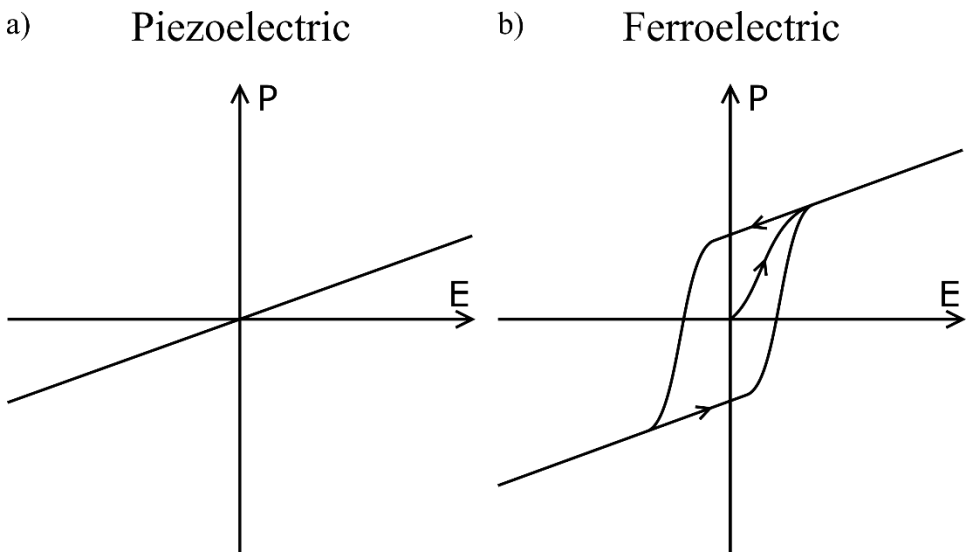

Figure 5.2 (a) the linear response of the polarization to the applied field in a piezoelectric material vs **(b)** the nonlinear response of polarization to an applied electric field.

This nonlinear behavior is a result of the polarization arrangement within the ferroelectric material. For each phase, there are multiple variants of polarization, each variant has its own unique spontaneous polarization and associated strain. With sufficiently high electric fields or stresses, the polarization can be switched to a different variant in the same phase or undergo a complete phase transformation. The mechanism of this change in polarization is through domain wall or phase boundary motion. This domain wall motion provides an increased electrical-mechanical coupling behavior which leads ferroelectric materials to having higher dielectric constants which produce a large strain response with an application of electric field[141]. The model developed

and presented in this chapter is used to assess the effect of ferroelectric domain wall (FDW) dynamics in the ferroelectric substrate on nanoscale magnetic structures. In these simulations, an electric field is applied in-plane to drive FDW motion in a rhombohedral crystal and study its interactions with single domain magnetic nanostructures for the first time. The introduction of strain inhomogeneity resulting from FDW motion offers additional insight on the magnetization response within multiferroic heterostructures as a result of the non-linear ferroelectric response of a substrate.

Many past research efforts have focused on modeling the response of ferroelectric or ferromagnetic films under the application of external fields[141]–[148]. There have been a smaller number of ferroelectric and ferromagnetic coupled models. Hu et al.[149], [150] presented a phenomenological model for the magnetization reorientation of different materials due to the strain response of homogenous ferroelectric substrates. Zhong et al.[151] studied the effects of CFO thin film grown on a linear homogeneous PMN-PT substrate under an applied out-of-plane electric field. Wang et al.[152] created a model to study the interactions of CFO and BiFeO films. Hu et al.[153] analyzed the out-of-plane magnetization response of CFO patterned rectangles on $BaTiO_3$ film. Liang et al.[68] developed a bi-directional model coupling linear piezoelectric, micromagnetics and elastodynamics equations using a finite element platform. This bi-directional model has been used to guide design of various devices with both in-plane and out-of-plane magnetization[83], [84], [98], [115], [154], [155] and has better predicted the behavior of the multiferroic heterostructures[82], [156]. The use of linear piezoelectric constitutive equations neglects the effects of any FDW motion within the substrate. Among the few efforts to couple the evolving domain structure of a ferroelectric to the magnetic behavior of a heterostructure, none have addressed the effects of a rhombohedral domain structure on a magnetostrictive material even

though this domain structure is most commonly used in strain-mediated multiferroic heterostructures.

In this chapter, results of simulations are presented that detail the effects of FDW motion within a ferroelectric rhombohedral single crystal substrate of $Pb(In_{1/2}Nb_{1/2})O_3$-$Pb(Mg_{1/3}Nb_{2/3})O_3$-$PbTiO_3$ (PIN-PMN-PT) on the in-plane magnetization dynamics of Ni disks. The strain change experienced by the Ni disk depends on whether the Ni is deposited away from a domain wall that subsequently sweeps under the entire disk or is deposited across an existing domain wall. In this work, the Ni disks modeled are assumed to have been deposited on a ferroelectric substrate with domains present. In the first case the Ni disk is deposited on one rhombohedral domain and a FDW then sweeps under the entire disk and strains it. In the second case, the Ni disk is deposited on a FDW and spans across two rhombohedral variants. As the FDW moves, only half of the disk is strained. The results are compared to the effect of linear piezoelectric strain induced in the substrate using the model developed by Liang et al. [68].

5.2 Simulation Details

a. Landau-Devonshire Theory for Ferroelectrics

Phenomenological thermodynamics based on Landau-Devonshire theory have been demonstrated to provide good predictions for the strain effects on the polarization behavior of a material, given that the thermodynamic potential function exists[73]. To include strain effects on the ferroelectric material, the free energy of the material is written in terms of the independent variables strain(ε_{ij}) and polarization$(P_i)$and provided in Equation 5.1.

$$dF = \sigma_{ij} d\varepsilon_{ij} + E_i dP_i \tag{5.1}$$

Here F is the Helmholtz-free energy for an isothermal system, σ_{ij} is the second-rank stress tensor and E_i is the component of the electric field. Using the Landau-Devonshire theory of ferroelectrics, the free energy in Equation 5.1 can be expanded to Equation 5.2 below:

$$F(\varepsilon, P) = \frac{1}{2}\alpha_{ij}P_iP_j + \frac{1}{3}\beta_{ijk}P_iP_jP_k + \frac{1}{4}\gamma_{ijkl}P_iP_jP_kP_l + \frac{1}{5}\delta_{ijklm}P_iP_jP_kP_lP_m + \frac{1}{6}\omega_{ijklmn}P_iP_jP_kP_lP_mP_n + \cdots + \frac{1}{2}c_{ijkl}\varepsilon_{ij}\varepsilon_{kl} - a_{ijk}\varepsilon_{ij}P_k - \frac{1}{2}q_{ijkl}\varepsilon_{ij}P_kP_l \quad (5.2)$$

Where α_{ij}, β_{ijk}, γ_{ijkl}, δ_{ijklm}, and ω_{ijklmn} are phenomenological expansion coefficients, c_{ijkl}, a_{ijk}, and q_{ijkl} are the elastic, piezoelectric and electrostrictive constant tensors, respectively. The coefficients are all constants with the exception of α_{ij} which is linearly proportional to the temperature. The electrostrictive constants tensor(q_{ijkl}) can be found from the electrostrictive coefficients(Q_{ijkl}) of a material measured from experiments using the elastic tensor and the relationship $q_{ijkl} = 2c_{ijmn}Q_{mnkl}$. When the material is centrosymmetric, as in the case of a ferroelectric material, the odd terms are dropped leading to a simplified form of the free energy given in Equation 5.3[73].

$$F(\varepsilon, P) = \frac{1}{2}\alpha_{ij}P_iP_j + \frac{1}{4}\gamma_{ijkl}P_iP_jP_kP_l + \frac{1}{6}\omega_{ijklmn}P_iP_jP_kP_lP_mP_n + \cdots + \frac{1}{2}c_{ijkl}\varepsilon_{ij}\varepsilon_{kl} - \frac{1}{2}q_{ijkl}\varepsilon_{ij}P_kP_l \quad (5.3)$$

This energy formulation is capable of capturing the nonlinear behavior of ferroelectric materials but must be derived for each phase of a ferroelectric material. Lv et al.[157] developed a unique 10th order energy expansion based on the Landau-Devonshire theory to capture the variant and phase transitions in rhombohedral single crystal $Pb(In_{1/2}Nb_{1/2})O_3$-$Pb(Mg_{1/3}Nb_{2/3})O_3$-$PbTiO_3$ (PIN-

PMN-PT) which is used to govern the ferroelectric substrate behavior in this combined model. For this particular phase, the three polarization components of the material can be reduced to two in-plane polarization components. This is a result of the polarization perpendicular to the applied field plane, in the [110] direction, is zero throughout the polarization switching process. The initial cubic coordinate system of the material is displayed in Figure 5.3a with the simplified two component coordinate system provided in Figure 5.3b. In Figure 5.3b, R1, R2, R3, and R4 indicate the different variants of polarization that can be expected in this rhombohedral phase.

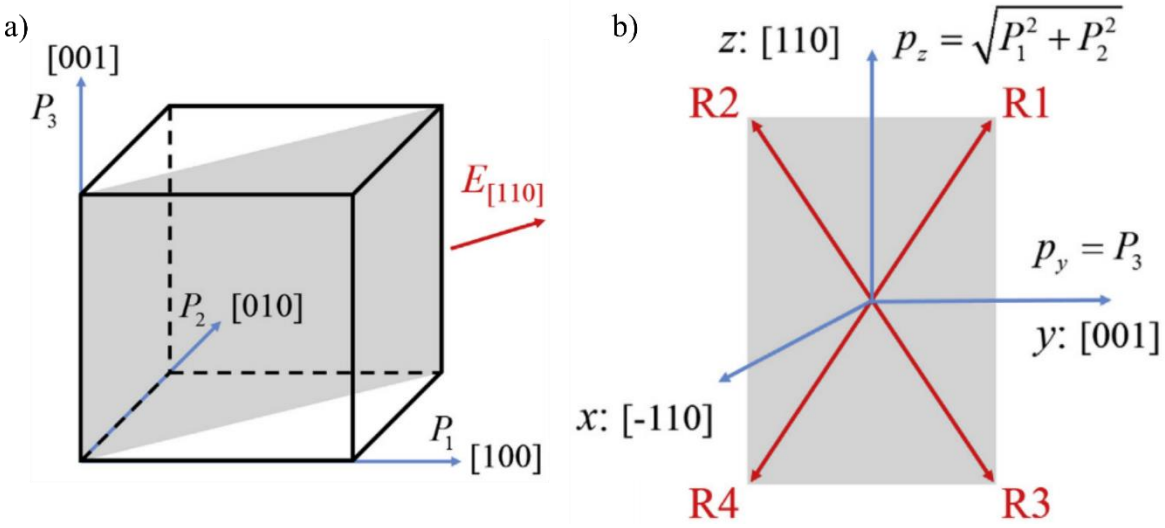

Figure 5.3 (a) Cubic coordinate system used to develop phase field model by Peng et al. **(b)** The simplified 2D coordinate system containing the four different variants of polarization, R1, R2, R3 and R4. This plane is the diagonal plane seen in (a) with the z-direction as the [110] direction.

The two component Landau-Devonshire energy developed by Lv et al.[157] for PIN-PMN-PT is provided Equation 5.4:

$$f_{LD} = \alpha_1\left(p_y^2 + p_z^2\right) + \frac{1}{2}\alpha_{11}\left(2p_y^4 + p_z^4\right) + \frac{1}{4}\alpha_{12}\left(4p_y^2p_z^2 + p_z^4\right) + \frac{1}{4}\alpha_{111}\left(4p_y^6 + p_z^6\right)$$
$$+ \frac{1}{4}\alpha_{112}\left(4p_y^4p_z^2 + p_z^6 + 2p_y^2p_z^2\right) + \frac{1}{4}\alpha_{123}p_y^2p_z^2 + \frac{1}{8}\alpha_{1111}\left(8p_y^8 + p_z^8\right)$$
$$+ \frac{1}{8}\alpha_{1112}\left(2p_y^2p_z^6 + p_z^8 + 8p_y^6p_z^2\right) + \frac{1}{16}\alpha_{1122}\left(8p_y^4p_z^4 + p_z^8\right)$$
$$+ \frac{1}{4}\alpha_{1123}\left(p_y^4p_z^4 + p_y^2p_z^6\right) + \frac{1}{16}\alpha_{11112}\left(2p_y^2p_z^8 + p_z^{10} + 16p_y^8p_z^2\right)$$
$$+ \frac{1}{16}\alpha_{11223}\left(4p_y^4p_z^6 + p_y^2p_z^8\right) + \frac{1}{8}\alpha_{11123}\left(2p_y^6p_z^4 + p_y^2p_z^8\right) \quad (5.4)$$

b. Ferroelectrics Phase-Field and Finite Element Model

The total free energy of this ferroelectric material is a combination of the 10th order Landau-Devonshire energy in Equation 5.4, the gradient energy, elastic energy, and the electric energy. The gradient energy is similar to the magnetic exchange energy discussed in Chapter 2 which prefers parallel alignment for neighboring electric dipoles. A higher energy is expected when parallel dipoles are misaligned. This energy affects the domain wall thickness in the material. The elastic energy is a result of the stress induced in the material and the electric energy is a direct effect of the electric field applied to the ferroelectric material. The equations for these energies as a function of the two polarization components, p_y and p_z are presented in Equations 5.5 – 5.8 [158].

$$f_{grad} = \frac{1}{2}G\left(p_{y,y}^2 + p_{z,z}^2 + p_{y,z}^2 + p_{z,y}^2\right) \quad (5.5)$$

$$f_{elas} = \frac{1}{2}C_{22}'\left(\varepsilon_{yy}^{el}\right)^2 + \frac{1}{2}C_{33}'(\varepsilon_{zz}^{el})^2 + C_{23}'\varepsilon_{yy}^{el}\varepsilon_{zz}^{el} + 2C_{44}'\left(\varepsilon_{yz}^{el}\right)^2 \quad (5.6)$$

$$f_{elec} = -E_y p_y - E_z p_z - \frac{1}{2}\kappa_0\left(E_y^2 + E_z^2\right) \tag{5.7}$$

Here, G is the gradient coefficient, C'_{22}, C'_{33}, C'_{23}, and C'_{44} are the transformed cubic elastic stiffness components, E_y, E_z, and κ_0 are the electric field components along each axis, y and z, and the permittivity of free space respectively. For further details of the development of this phase-field model, readers are encouraged to see references [157] and [158]. The phase field model was then implemented in a finite element platform to study ferroelectric material behavior in the presence of external stress and electric fields by Lv et al.[158].

The temporal response of polarization to external (stress or electric) fields is governed by the Time-Dependent-Ginzburg-Landau(TDGL) Equation. The 2D TDGL equation is given in Equation 5.8.

$$\beta \dot{p_y} = \left(\frac{\partial f}{\partial p_{y,y}}\right)_{,y} + \left(\frac{\partial f}{\partial p_{y,z}}\right)_{,z} - \frac{\partial f}{\partial p_y} \tag{5.8a}$$

$$\beta \dot{p_z} = \left(\frac{\partial f}{\partial p_{z,y}}\right)_{,y} + \left(\frac{\partial f}{\partial p_{z,z}}\right)_{,z} - \frac{\partial f}{\partial p_z} \tag{5.8b}$$

$$f = f_{LD} + f_{grad} + f_{elas} + f_{elec} \tag{5.9}$$

Here β is the inverse mobility constant and f is the total energy of the system, given in Equation 5.9, which is the sum of the Landau-Devonshire, gradient, elastic and electric energies. Using first variations techniques as in Chapter 2, the governing equation was converted to a weak form for use in a finite element platform. The model developed was demonstrated to successfully predict the behavior of polarization in rhombohedral PIN-PMN-PT. Various polarization dynamics were observed in PIN-PMN-PT film, including the formation of 71° and 109° domain walls from an

initially randomized polarization state. In addition, the model predicts polarization switching behavior at sufficiently high fields when 71° FDWs were present but no corresponding FDW motion. FDW propagation was observed for substrates with 109° domain wall presents which would subsequently sweep across the substrate rotating the polarization direction to be energetically favorable with the applied field orientation[158]. The 109° domain wall was used to study the effects of FDW motion on magnetic nanoelements in a new finite element model to better understand magnetization response in strain-mediated multiferroic heterostructures.

Due to limitations of computer memory, the simulated heterostructure must be on the order of 500 nm. As a result, the geometry for the ferroelectric substrate modeled was a 2D, 500 nm x 240 nm substrate with [011] cut PIN-PMN-PT properties[158]. Since ferroelectric domains can vary in size between 100's of nanometers to few microns[159], a single 109° FDW was artificially initiated at the center of this substrate. To set a FDW at a specific location, the polarization on the left and right of the FDW were defined. The polarization had components P_x and P_y on the left of the FDW and components P_x and $-P_y$ on the right of the FDW as illustrated in Figure 5.4b. Once these initial conditions were applied, the system relaxed to form the desired equilibrium FDW governed by TDGL. The boundary conditions developed by Lv et al.[158] included periodic boundary conditions to imitate an infinite substrate and allow for expansion and contraction of the boundaries without producing any additional strain. These boundary conditions are presented in Figure 5.4a.

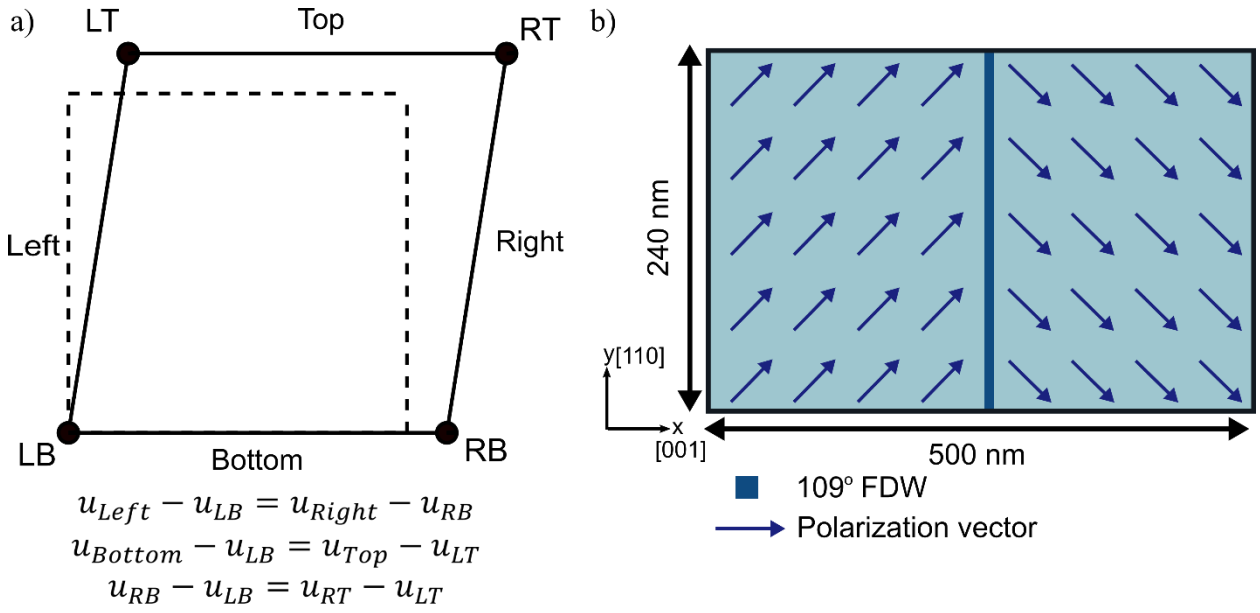

Figure 5.4 (a) The boundary conditions implemented by Lv et al.[158] in the finite element model for PIN-PMN-PT where u represents the displacements in the x-direction. An additional set of three equations (not shown) are prescribed for the displacements in the y-direction. **(b)** The PIN-PMN-PT substrate used in the model to represent strain-mediated multiferroic heterostructure. To initiate the FDW at a specific location, the polarization vectors on the left and right of the domain wall must be prescribed as shown.

After the formation of the FDW, an electric field on 0.46 MV/m was applied in the [110] direction causing FDW propagation to the right. The magnitudes of the polarization components were $P_x = 0.271 \left[\frac{C}{m^2}\right]$ and $P_y = 0.384 \left[\frac{C}{m^2}\right]$ [158] and the applied electric field was 0.46 MV/m. After a mesh convergence study, it was determined that the minimum size mesh to use for the propagation of the FDW was a 6 nm triangular mesh.

c. Coupled Ferroelectrics and Micromagnetics Model

In the phase field model with magnetization as the order parameter, the evolution of magnetization is governed by the LLG Equation, Equation 5.10:

$$\dot{\boldsymbol{m}} = -\mu_0\gamma\left(\boldsymbol{m} \times \boldsymbol{H}_{eff}\right) + \alpha(\boldsymbol{m} \times \dot{\boldsymbol{m}}) \tag{5.10}$$

where, $\boldsymbol{m}$ is the normalized magnetic moment vector and the over dot represents the time derivative, μ_0 is the permeability of free space, γ is the gyromagnetic ratio, α is the damping constant, and $\boldsymbol{H}_{eff}$ is the effective magnetic field. The total free energy for the magnetic domain, $E_{total} = E_{zeeman} + E_{ex} + E_{mca} + E_{demag} + E_{elas}$, is the sum of the Zeeman, magnetic exchange, magnetocrystalline, demagnetization and elastic energies[90]. Details of finding each energy term are discussed in Chapter 2. $\boldsymbol{H}_{eff}$ is found by taking the partial derivative of the total free energy with respect to magnetization: $\boldsymbol{H}_{eff} = -(1/\mu_0 M_s)\,(\partial E_{total}/\partial \boldsymbol{m})$ where M_s is the saturation magnetization[68].

To study individual magnetic reorientations on different parts on a ferroelectric substrate, a Ni disk was positioned at two different locations on the substrate to observe magnetization dynamics due to the motion of different FDW configurations as seen in Figure 5.5a and 5.5b. In the first simulation, the Ni disk was positioned so the FDW starts to the left of disk and then the FDW propagated through the substrate travelling across the entire bottom surface of the Ni disk. This is referred to as "Left" disk since the FDW was initialized on the left of the disk. In the second simulation, the Ni disk was positioned such that the FDW bisects the disk. The FDW propagates across half of the Ni disk when the ferroelectric is excited. This is referred to as "Middle" disk since the FDW was initialized in the middle of the disk.

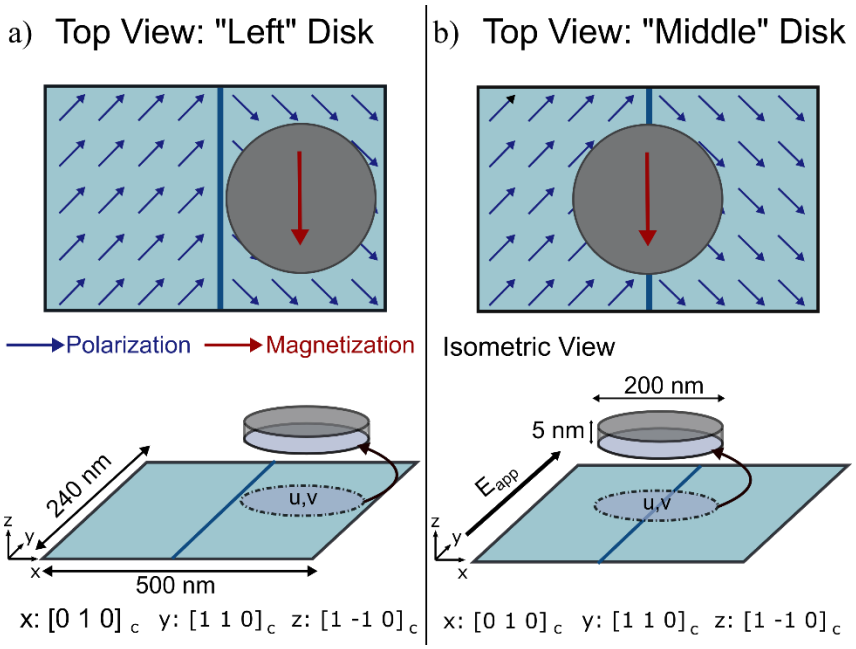

Figure 5.5 (a) the initial polarization (blue arrows) and magnetization (red arrows) configuration of the "Left" Ni disk where the FDW sits entirely on the left side of the magnetic element. The bottom panel indicates that displacements are directly transferred from the ferroelectric surface to the magnetic domain. **(b)** The initial polarization and magnetization configuration for the "Middle" Ni disk where the FDW sits directly underneath the magnetic domain. The bottom panel indicates the direction of the applied field E which will cause the FDW to propagate to the right in the positive x-direction. The coordinate axis are labelled for reference.

The displacements in the x- and y- directions from the 2D surface of the ferroelectric substrate were transferred onto the bottom surface of the disk. When an amorphous magnetic material is deposited on a ferroelectric substrate, the strain in the magnetic material is zero even when there are eigenstrains in the ferroelectric substrate associated with polarization. To account for this zero initial strain in the disk, the transferred displacements were normalized with respect to the displacement generated from the FDW formation. The disk itself was mechanically constrained to suppress rigid body rotation by fixing the displacements at the left edge of the disk. To capture the effects of magnetostrictive behavior of the material, the influence of the magnetization induced strain on the Ni disk was represented as a body force derived from the magnetostrictive strain, $\varepsilon_{ij}{}^{m}$

(Equation 5.11)[90], the elastic constitutive relationship between stress (${\sigma_{ij}}^{m}$) and strain, (Equation 5.12)[160], and mechanical equilibrium equation (Equation 5.13)[160].

$$ {\varepsilon_{ij}}^{m} = \frac{3}{2}\lambda_s\left(m_i m_j - \frac{1}{3}\right) \tag{5.11} $$

$$ {\sigma_{ij}}^{m} = \lambda {\varepsilon_{kk}}^{m} + 2\mu {\varepsilon_{ij}}^{m} \tag{5.12} $$

$$ {\sigma_{ij,i}}^{m} + f_j^m = \rho u_{j,tt} \tag{5.13} $$

Where λ_s is the magnetostrictive constant, λ and μ are the first and second Lame's elastic constants, ρ is the density of the magnetic element, and $u_{j,tt}$ is the second time derivative of the displacements. Substitution of Equation 5.12 into Equation 5.13 yields the three different force components listed in Equation 5.14.

$$ f_1 = \rho u_{1,tt} - \lambda_s\left(\varepsilon_{kk,1} - 2\mu\varepsilon_{i1,i}\right) \tag{5.14a} $$

$$ f_2 = \rho u_{2,tt} - \lambda_s\left(\varepsilon_{kk,2} - 2\mu\varepsilon_{i2,i}\right) \tag{5.14b} $$

$$ f_3 = \rho u_{3,tt} - \lambda_s\left(\varepsilon_{kk,3} - 2\mu\varepsilon_{i3,i}\right) \tag{5.14c} $$

Next, the divergence of Equation 5.11 is found in Equation 5.15 and substituted into Equation 5.14 to find the equivalent body force due only to magnetization changes within the material.

$$ \varepsilon_{ij,j} = \frac{3}{2}\lambda_s\left(m_{i,i}m_j + m_i m_{j,i}\right) \tag{5.15a} $$

$$ \delta_{ij}\varepsilon_{kk,i} = \ \varepsilon_{kk,j} = \frac{3}{2}\lambda_s\left(m_{k,j}m_k + m_k m_{k,j}\right) = 3\lambda_s\left(m_{k,j}m_k\right) \tag{5.15b} $$

Plugging Equation 5.15a and 5.15b into the three force components yields the final form of the body force included in the finite element model:

$$f_1 = \rho u_{1,tt} - 3\lambda_s \Big[\lambda\big(m_{1,1}m_1 + m_{2,1}m_2 + m_{3,1}m_3\big) + \mu\Big(\big(m_{1,1} + m_{2,2} + m_{3,3}\big)m_1 + m_1 m_{1,1} + m_2 m_{1,2} + m_3 m_{1,3}\Big)\Big] \quad (5.16a)$$

$$f_2 = \rho u_{2,tt} - 3\lambda_s \Big[\lambda\big(m_{1,2}m_1 + m_{2,2}m_2 + m_{3,2}m_3\big) + \mu\Big(\big(m_{1,1} + m_{2,2} + m_{3,3}\big)m_2 + m_1 m_{2,1} + m_2 m_{2,2} + m_3 m_{2,3}\Big)\Big] \quad (5.16b)$$

$$f_3 = \rho u_{3,tt} - 3\lambda_s \Big[\lambda\big(m_{1,3}m_1 + m_{2,3}m_2 + m_{3,3}m_3\big) + \mu\Big(\big(m_{1,1} + m_{2,2} + m_{3,3}\big)m_3 + m_1 m_{3,1} + m_2 m_{3,2} + m_3 m_{3,3}\Big)\Big] \quad (5.16c)$$

The magnetic material properties and geometry used in these studies were those of a nanometer scale polycrystalline Ni disk (i.e. isotropic) with diameter of 200 nm and thickness of 5 nm. The exchange constant, saturation magnetization, damping constant, Young's Modulus, magnetostrictive constant, and the two magnetoelastic coupling coefficients were: $A = 1.05e-11\ [J/m]$,[90] $M_s = 4.85e5\ [A/m]$,[90] $\alpha = 0.038$,[161] $Y = 200\ [GPa]$,[90] $\lambda_s = -34e-6$,[90] $B_1 = 6.2e6\ [N/m^2]$,[90] and $B_2 = 4.3e6\ [N/m^2]$,[90] respectively.

d. Coupled Ferroelectrics and Micromagnetics Model Results

With the field applied in the [110] direction, the FDW propagates to the right beneath the Ni disk to the edge of the substrate as seen in the lower panel images of Figure 5.6a and 5.6b. The lower panel demonstrates the final polarization configuration (arrows) in the substrate after full propagation of the FDW. The upper panel of Figure 5.6a shows the final magnetic configuration

(arrows) and biaxial in-plane principal strain, $\varepsilon_1 - \varepsilon_2$ (color bar) for the "Left" disk. The resulting in-plane biaxial strain difference and magnetization configuration within the "Middle" disk is visible in the upper panel of Figure 5.6b.

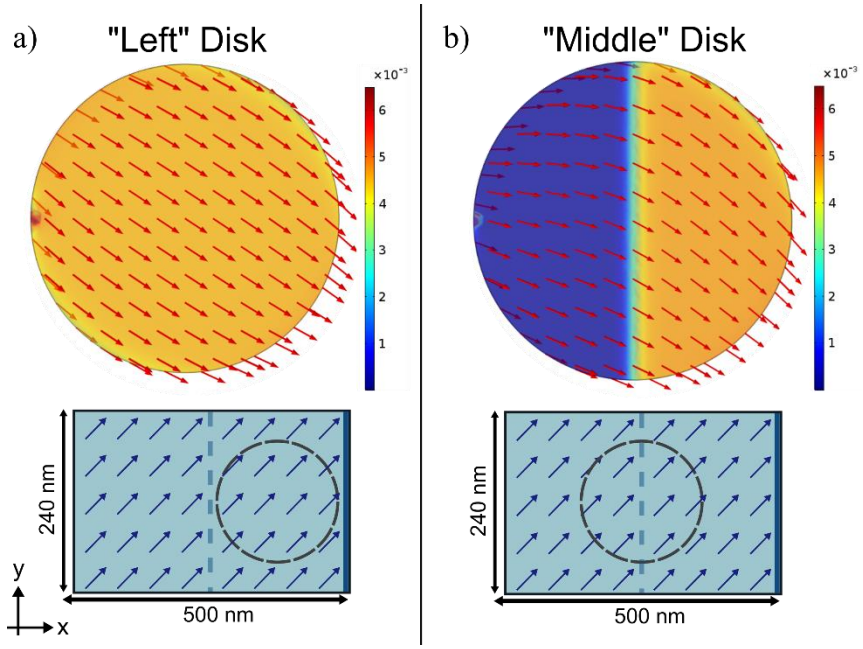

Figure 5.6 (a) (Upper panel) The final magnetization (arrows) and average in-plane principal strain difference, $\varepsilon_1 - \varepsilon_2$, (color bar) and (Lower panel) the final polarization configuration (arrows) after full propagation of the FDW within the 200 nm **(a)** "Left" disk and **(b)** "Middle" disk.

In Figure 5.7a the average principal strain difference across the bottom surface of the "Left" disk is plotted as Δ_{Left}. The initial strain in the nickel element was set to zero to approximate a system where the disk was deposited after FDW relaxation. As time increased, a continuous growth of the in-plane principal strain difference was observed as the upward polarization domain increased in size and stretched the substrate in the y-direction while compressing in the x-direction. As the FDW propagated through the disk, a 0.48% strain difference was generated in its path of motion.

Similar strain behavior is evident in the "Middle" Ni disk case where the FDW was located at the center of the disk. The bottom surface principal strain difference behavior is captured in the Δ_{Middle} curve of Figure 5.7a. As the FDW propagated, the change in the in-plane strain continuously increased in magnitude as well. However, the time of propagation for the FDW across the bottom surface of the disk was shorter. As the FDW moved across the bottom surface of the disk, it also generated a strain of 0.48% in the region of FDW propagation. Since the strain was generated on only half the surface of the disk, the average strain for the disk measured was 0.24%. This value is expected since the region with no FDW motion recorded a strain of approximately 0%. In the left region with no FDW motion, a local region of 1.4% compressive strain oriented along the x-direction was observed resulting from the mechanical boundary condition to suppress rigid body rotation. Experimentally, one would expect pinning sites due to defects in the magnetic disk which would produce similar localized regions of high magnetic anisotropy as discussed in Chapter 4. The strain responses of the different FDW configurations resulted in two unique final magnetic configurations.

For the "Left" disk, the average magnetization angle settled at $\theta_m = -35^o$as evident in Figure 5.7b from the $Left$ curve. The increase in θ_m between t = 1.1 and 1.95 ns corresponds to the ramping of the electric field within this time interval. The slight overshoot and then drop off the angle at the end of the ramp when the field was held constant results for low damping of Ni, $\alpha = 0.038$. The total magnetization change was $\Delta\theta_m = 45^o$ due to the FDW propagation in the "Left" disk.

In the "Middle" disk, the average magnetization settled at $\theta_m = -25^o$. However, the magnetization was not uniform within the domain. The magnetization in the region where the

FDW did not propagate (left of the FDW), was measured to be $\theta_m = -11^o$ and $\theta_m = -37^o$ in the propagation region (right of the FDW). The tendency of the magnetization to align along the x-direction in the left region is a result of the strain produced from the mechanical boundary condition creating an artificial easy axis of magnetization causing small pinning effects. With approximately zero strain in the surrounding region to overcome this effect, the magnetization prefers horizontal alignment in the region left of the FDW despite 0% strain in the region. However, the average magnetization in the right of the disk is uniform and closely matches the magnetization direction obtained for "Left" disk. The total magnetization change predicted from the model was $\Delta\theta_m = 55^o$ due to the FDW propagation in the "Middle" disk.

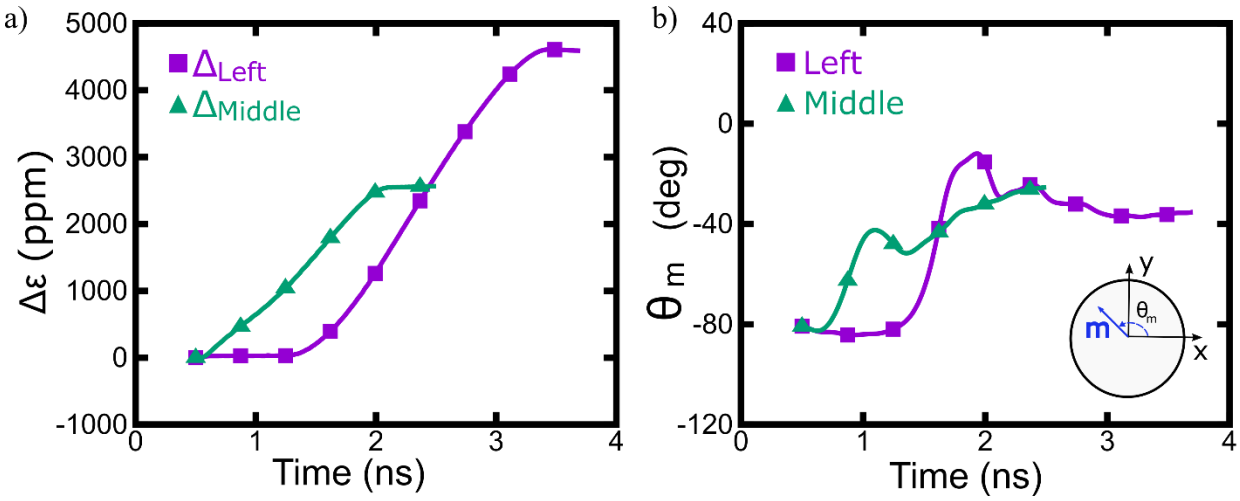

Figure 5.7 (a) the in-plane biaxial principal strain difference, Δ, of the "Left" and "Middle" disks and **(b)** the volume average magnetization angle, θ_m, of these simulations.

5.3 Comparison with Linear Piezoelectric Model

a. PIN-PMN-PT Coordinate Transformation

The results of the new ferroelectric and micromagnetics model were then compared to the linear piezoelectric model developed by Liang et al.[68]. In this model, properties of [110] crystal cut of

PIN-PMN-PT[162] were used to predict the magnetization response due to the linear piezoelectric substrate alone, assuming no FDWs present in the substrate. The piezoelectric coefficients provided in reference [43] from experimental results were defined for PIN-PMN-PT such that [011] is along the z- axis, and [0-11] and [100] were along the x- and y- axis respectively. In order to ensure the linear model was directly comparable to the ferroelectric model discussed in Section 5.2, a transformation of coordinates was necessary such that the [011] access was aligned in-plane and voltage applied along the same direction. For ease of calculation, the x- and z- axis were switched making the [011] direction the x-axis in the linear model. Pictorially, this transformation is given in Figure 5.8.

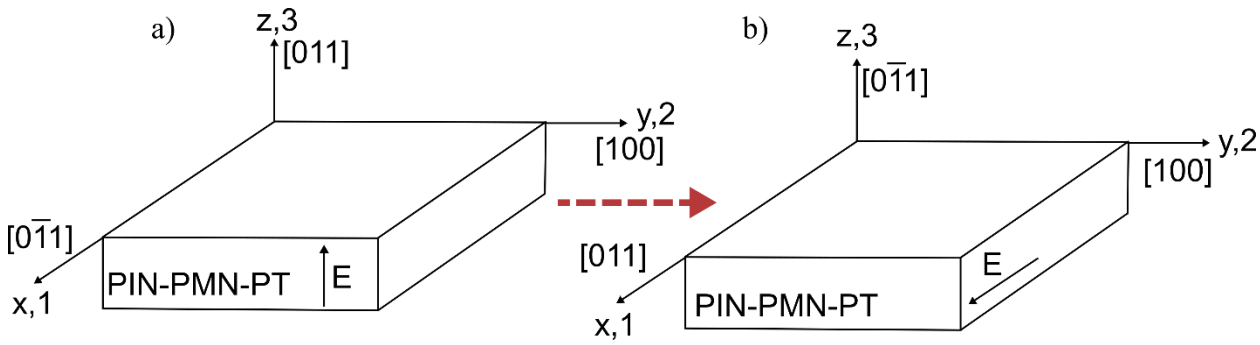

Figure 5.8 (a) The transformation of the out-of-plane [011] direction to the **(b)** in-plane direction to directly compare the nonlinear ferroelectric model in section 5.2 to the currently used linear piezoelectric finite element model.

Several modeling checks were conducted to ensure the results of the linear piezoelectric model. In the first validation test, a finite element model, let's call it *Model A*, was created in which the coordinate axis and material properties referenced by Sun et al.[162] were set-up as in Figure 5.8a. The out-of-plane electric field was varied from 0 to 0.8 MV/m and the strain components of the [0 1 -1] and [1 0 0] directions were measured at each field value. These values were then compared to experimental results of PMN-PT (similar material properties) to ensure the model set-up was capable of predicting experimentally measured strain values expected in the ferroelectric substrate

used in strain-mediated multiferroic heterostructures. The results of this modeling test are shown in Figure 5.9a with the corresponding experimental data of [011] cut PMN-PT provided in Figure 5.9b demonstrating good agreement. *Model A* can thus be used as a reference model to compare the results of a transformed coordinate system discussed next.

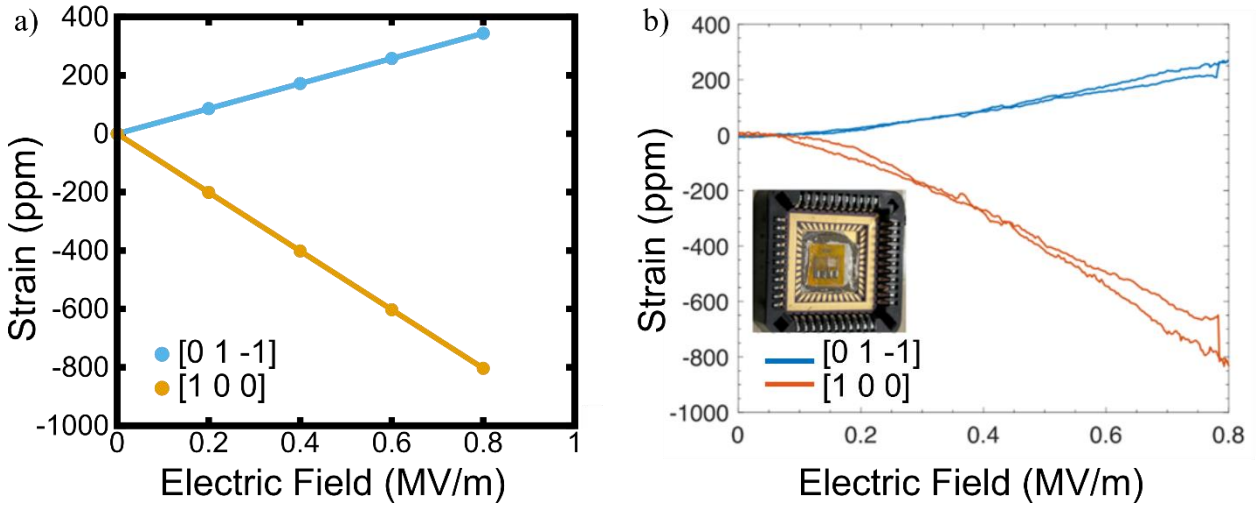

Figure 5.9 (a) The [01-1] and [100] strain components predicted from the linear piezoelectric finite element model when varying the applied field in the [011] direction between 0 and 0.8MV/m and **(b)** the experimental data obtained for the same strain components in a sample of PMN-PT measured by Xiao et al.[163]

A second validation test was conducted to check that the transformation of the coordinates were successful. In a second model, *Model B*, the coordinate axis and material properties from Sun et al.[162] were transformed according to Figure 5.8b, where the x- and z- axes were interchanged. In this model, the electric field was applied for one value only, 0.46 MV/m, to match the electric field used in Section 5.2. The corresponding strain difference between, ε_{22} and ε_{11} was found. This result of *Model B* was then compared to the strain difference between ε_{33} and ε_{22} of *Model A*. Note that the strain on the plane parallel to the applied field was computed for each model to mimic the configuration implemented in the model of Section 5.2. Finally, the strain values obtained were compared to the theoretical value predicted using linear piezoelectric equations. All values are

summarized in Table 5.1 with the percent error being calculated with respect to the transformed coordinate system in *Model B* since this was used for the linear piezoelectric model to compare with the results of Section 5.2d.

Table 5.1 Strain value comparison to validate modeling results of linear piezoelectric model

	Strain (ppm)
Model A	799.81
Model B	806.30
Theoretical	891.5
% Error	9.5

b. Linear Model Simulation Set-up and Results

To simulate the strain-mediated multiferroic heterostructure, a 200nm Ni disk was placed on an 800 nm x 800 nm PIN-PMN-PT substrate with a 0.46 MV/m electric field applied in the x-direction. The initial magnetization within the magnet was set with the magnetization angle at negative 90º. This initial set-up is depicted in Figure 5.10a. The final magnetization configuration of the 200nm Ni assuming linear piezoelectric strain generated in the substrate due to the lack of FDW motion is seen in Figure 5.10b. The color bar plots the in-plane principal strain difference generated in the magnetic disk.

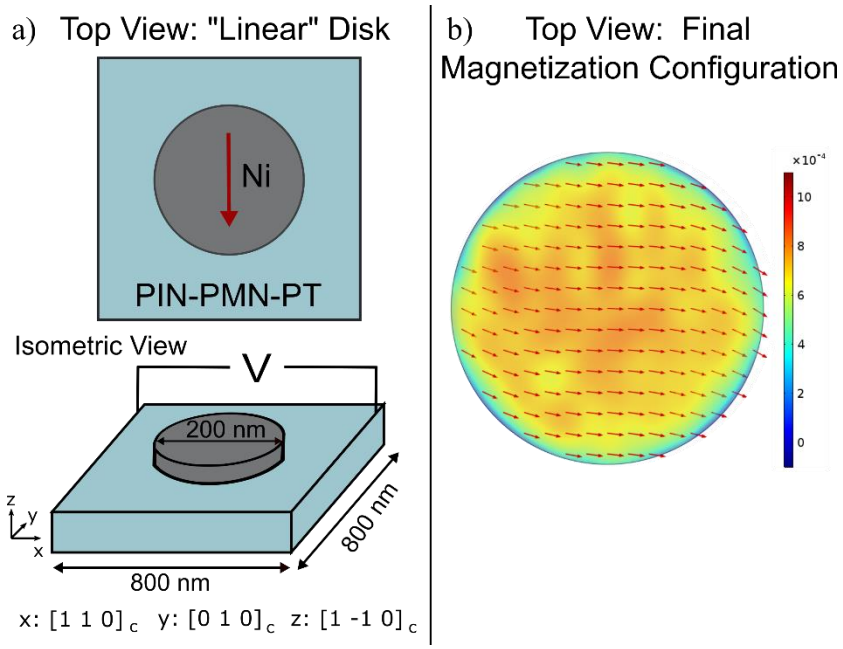

Figure 5.10 (a) The model set-up for the linear piezoelectric model for a similar device structure with no polarization domains or FDWs present. **(b)** The final magnetization configuration (arrows) and average in-plane principal strain difference, $\varepsilon_1 - \varepsilon_2$, (color bar) predicted from the linear piezoelectric model

When no FDW propagates through the substrate, the strain values are derived from the electromechanical coupling coefficients and not the quadratic relationship between the strain and polarization. As a result, the in-plane biaxial strain was calculated to be approximately 0.065%. This is lower than the predicted strain values found in Table 5.1 and may be a result of the thin Ni disk experiencing some clamping effects on the linear substrate. Additionally, with no motion of domains, the strain eventually settled to this value since no domain growth occurs. The linear model predicted that with just the small biaxial strain difference, the largest change in magnetization angle would occur with $\Delta\theta_m = 90^o$. Past simulations using this linear piezoelectric model have all predicted similar large magnetization rotations with small applied fields. However, the new TDGL and LLG simulations indicate the motion of FDW within the substrate may impede the ideal magnetization behavior expected from linear models. The strain and magnetization

response of the linear piezoelectric model are plotted on the same plots shown in Figure 5.7 to directly compare the linear model with the new nonlinear ferroelectric model in Figure 5.11.

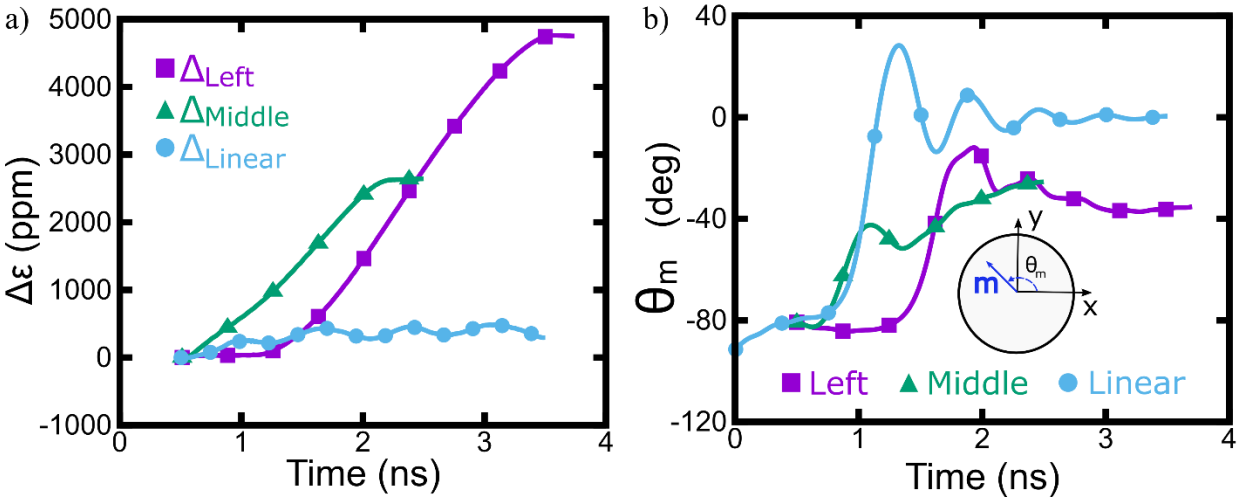

Figure 5.11 (a) the in-plane biaxial principal strain difference, Δ, of the "Left", "Middle", and "Linear" disks and **(b)** the volume average magnetization angle, θ_m, of these three simulations.

5.4 Conclusion and Outlook

In this work, the rhombohedral symmetry phase field model of PIN-PMN-PT substrate was combined with LLG and elastodynamics equations to study the effects of inhomogeneous strain in strain-mediated multiferroic heterostructures. The previous models used to predict the behavior of single domain magnetic islands on a ferroelectric substrate could only account for linear behavior of the substrate. In these simplified models, linear actuation of the substrate resulted in large changes in magnetization, even at small input strains. However, as this new model indicates, strain inhomogeneity arising from the nonlinear effects of the ferroelectric material, can drastically diminish the degree of magnetization reorientation. This model serves as a stepping stone towards understanding why arrays of otherwise identical magnetic islands experience disparate switching behavior in experiments conducted at identical input voltages across a single ferroelectric substrate. Theoretically, this simulation framework can better guide the design of future

multiferroic nanostructures to account for the nonlinear ferroelectric responses at or near domain walls.

Work still remains in expanding the 2D ferroelectric phase-field model to a full 3D finite element model. The current framework for the ferroelectric model allows for a fully 3D model of FDWs in the ferroelectric substrate. However, to implement this ferroelectric model with the 3D micromagnetics equations requires large computational time and memory which makes this model a challenge as a practical design tool. Future improvements for this model will explore methods to lessen the run time. However, with the development of faster solver techniques the methods discussed in this chapter can be used to better design and understand magnetic structure behavior in multiferroic composite structures. As Chapters 3-5 have indicated, the non-uniform strain response in these multiferroic structures greatly impacts the magnetization behavior when magnetization lies in-plane of the magnetic domain. However, this presents a problem with the repeatability of device behavior across an array of patterned devices. One alternative is to consider out of plane magnetization to capture and manipulate magnetic beads for cell sorting devices. This pathway towards multiferroic cell sorting devices is discussed in Chapter 6.

VI. Modeling Interactions between Magnetic Beads and Perpendicular Magnetic Anisotropy Disks

6.1 Introduction

In order to effectively use multiferroic structures as magnetic bead based cell sorting techniques, the magnetic field gradients from the multiferroic structure must be large enough to effectively trap magnetic beads. These large field gradients are typically created by using large external permanent magnets, which scale inefficiently to the nanoscale. Current research efforts are geared towards the micron- and nano-scaled devices for higher density, targeted cell sorting applications[6], [164]. One proposed solution to produce these gradients at the smaller scale is to use an array of patterned soft magnetic material on a substrate. In this solution, the necessary magnetic field gradients are produced by magnetizing each patterned element using an external magnet[165]–[169]. However, this solution still includes the use of a permanent magnetic for successful operation.

To achieve magnetization of patterned magnetic elements in a substrate without the use of an external magnet, the perpendicular magnetic anisotropy (PMA) effect can be utilized. PMA is when the magnetization components of a material align completely out-of-plane of the material. This effect is a result of either geometry of the material or the interface properties in a material[170], [171]. Specifically, PMA will occur in a ferromagnetic material below a critical thickness or in a magnetic multilayer system. To generate stronger magnetic field gradients, it is beneficial to use a multilayer system to produce the PMA effect. Using a multilayer allows more control of the magnetic field gradients without being limited by the critical thickness required when PMA is simply a result of the geometry. When magnetic field gradients arise from pure

geometry effects, it is beneficial to have a larger volume of magnetic material. Purely geometry related PMA effect is less desirable since it is limited by the critical thickness of the material, resulting in a smaller volume magnet.

We proposed a method of using patterned disks composed of alternating layers of Cobalt (Co) and Nickel (Ni) as a method to trap magnetic beads without the use of an external magnet. Co/Ni multilayers were desired because of their demonstrated capability of larger PMA when compared to other combinations of Co multilayers, such as Co and Silver (Ag) and Co and Copper (Cu)[172], [173]. Additionally, the magnetic field gradients can be further tuned by adjusting the relative thickness of the Co and Ni layers. This is achieved since the resulting magnetic saturation (M_s) is changed when the thicknesses of the layers are altered. Using PMA based sorting methods can increase the density of cell sorting devices and may be the solution necessary to overcome the strain inhomogeneity challenges arising for in-plane magnetic structures discussed in previous chapters. A simple finite element model is used to observe the interactions of the magnetic beads and a Co/Ni disk with PMA in order to predict the feasibility of future multiferroic cell sorting devices using PMA instead of in-plane magnetization.

6.2 Simulation Details

A finite element software was used to simulate the force interactions between the Co/Ni disk and the magnetic bead used for magnetic cell sorting applications. The Co/Ni multilayer was simplified as a single disk with thickness of 4 nm to match the thickness of the fabricated Co/Ni multilayers. The magnetic beads used for cell sorting applications are typically made of superparamagnetic nanoparticles enclosed in a polymer coating. This complex structure was reduced to one solid magnetic sphere, which we term the magnetic core. A gap was added between the bottom surface of the magnetic core and the top surface of the magnetic disk to represent the thickness of the

polymer coating. It should be noted that these simplifications could affect the magnitude of the resulting interaction forces, thus the simulations were mainly used as a design tool to understand general trends of interaction forces between the magnetic core and the Co/Ni multilayer disk. The layout of the model is seen in Figure 6.1. The image represents the side view of the disk and magnetic bead where the z-axis is in the vertical direction, the x-axis is in the horizontal direction, and the y-axis (not shown) is out of plane.

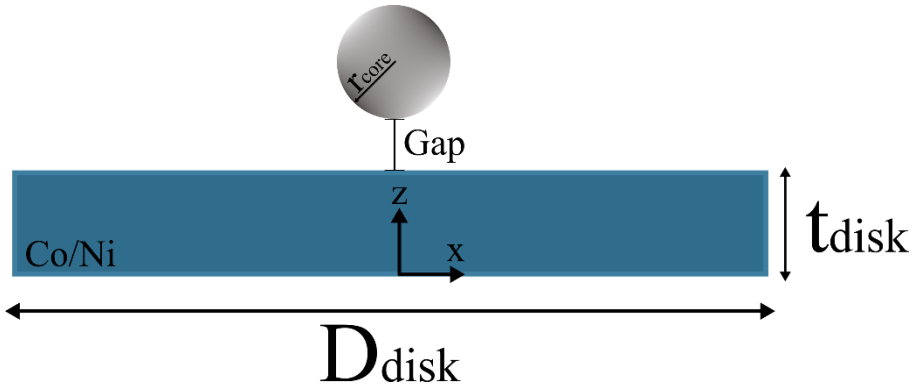

Figure 6.1 Side view of model layout where the top circle represents the magnetic bead and the bottom rectangle displays the Co/Ni multilayer disk. The "Gap" between the bottom surface of the bead and the top surface of the disk is representative of the polymer coating.

Several parameters were varied to study how different factors would influence the force interactions between the Co/Ni disk and the magnetic bead. These factors included the diameter of the Co/Ni disk as well as the magnetic saturation, M_s, of the disk. In addition, the magnetic bead size was varied to account mimic commercially available magnetic beads which could be used for experimental verification. Additional simulations analyzed how varying polymer thickness of the magnetic bead might affect the capture forces. The set-up of the different simulations are described next.

The first set of simulations analyzed how changing bead diameter alone might affect the interaction forces between the magnetic bead and disk. In these simulations, the Co/Ni disk diameter was held

constant at 4 μm. Bead diameters between 400 nm and 4 μm were tested. For many of the available magnetic beads used in cell sorting technologies, the polymer coating to magnetic core ratio is approximately 2:1. This constant ratio was applied to the simulations to determine the appropriate gap size.

Next, the effect of changing the disk diameter was studied. In this simulation, M_s was held constant at 1000 emu/cc and tested for two different bead diameters of 1 μm and 2 μm using the constant ratio of polymer thickness to magnetic core as being 2:1 to determine the gap size. The disk diameters tested were {2, 4, 6, 8} μm. Additional simulations were conducted to observe any changes in force interactions due to changing gap size only. In these simulations two magnetic core sizes were tested, a 500 nm magnetic core diameter and a 1000 nm magnetic core diameter. These diameters are representative of a 1 μm and 2 μm magnetic bead respectively with a variable thickness of polymer coating. The polymer thickness/gap sizes simulated varied between 200 and 500 nm.

One last set of simulations was done to observe the changes in force interactions due to changing M_s. In these simulations, the Co/Ni disk diameter was held constant at 4 μm. Five different M_s values were tested, {600, 700, 800, 900, 1000} emu/cc. These values fall within the range of M_s values of Co and Ni which are 487 and 1400 emu/cc[174], [175], respectively. As mentioned in Section 6.1, the M_s values of the Co/Ni disks can be tuned by adjusting the different thicknesses of the Co and Ni during the fabrication of the layered structure. For each of the five M_s values, four different magnetic bead diameters were tested, {0.2, 0.4, 0.6, 0.8} μm. These bead diameters were selected since smaller bead diameters provide higher spatial resolution during image analysis. A constant polymer to magnetic core ratio of 2:1 was used.

For all simulations, the magnetization in the Co/Ni disk was set to be out-of-plane, directed along the positive z-axis. The relative permeability of the magnetic core was equal to the relative permeability of the commercially available magnetic beads found to be 11.3[176]. A triangular mesh of 40 nm was swept through the thickness of the magnetic disk. A 20 nm tetrahedral mesh was used for the magnetic core. The interaction force between the magnetic core and Co/Ni disk was then calculated by varying the x-position of the magnetic core while keeping the z-position constant. The z-position was varied from the left of the disk, where x values of position are negative, and moved in positive 50 nm increments towards the center of the disk when $x = 0$. The corresponding force components (F_x, F_y, F_z) on the magnetic bead at each location was calculated. These results of all the studies are summarized next.

6.3 Simulation Results and Discussion

First we consider the effects of changing bead diameters with constant disk diameter of 4 μm and M_s value of 1000 emu/cc. The smallest bead diameter to disk diameter ratio was 1:10 while the largest ratio simulated was 1:1. The five total bead diameters tested were {400, 1000, 2000, 2800, 4000} nm. Figure 6.2 summarizes these results. In Figure 6.2a, the x-componenet of the force is provided as the bead location is swept from $x = -3$ μm to $x = 0$ μm where 0 μm represents the center of the disk. Due to symmetry of the Co/Ni disk, it is sufficient to end force calculations at the center of the disk in order to determine overall trends in the force profile. Note that the initial location of the bead is to the left of the disk, where the disk edge is located at $x = -2$ μm. The location of the disk is displayed by the blue rectangle in the bottom on the plot. In Figure 6.2b the z-component of the force is plotted. Both force components are seen to increase with increasing bead diameter suggesting larger beads will produce stronger interaction forces with the Co/Ni disk. However, as the bead diameter approaches the disk diameter, there is a shift in the location of the

maximum z-component force. With smaller bead diameters, the location of maximum force is close to the edge of the disk around $x = -2\ \mu$m, however, this peak shifts towards the center of the disk as the bead diameter increases. These results are consistent with findings by Rapport et al.[21] who studied the interaction of magnetic beads with magnetic domain walls. In these findings, she demonstrated in smaller bead to domain wall width ratios, the trapping forces are higher along the edges of the domain wall. As this ratio increases, such that the bead diameter is equal to or much greater than the domain wall width, the attractive force between the two objects is localized in the center of the domain wall. For localized trapping of beads then, it is important to consider both the size of the bead and the disk to determine the location of capture to properly design the structure used for cell sorting.

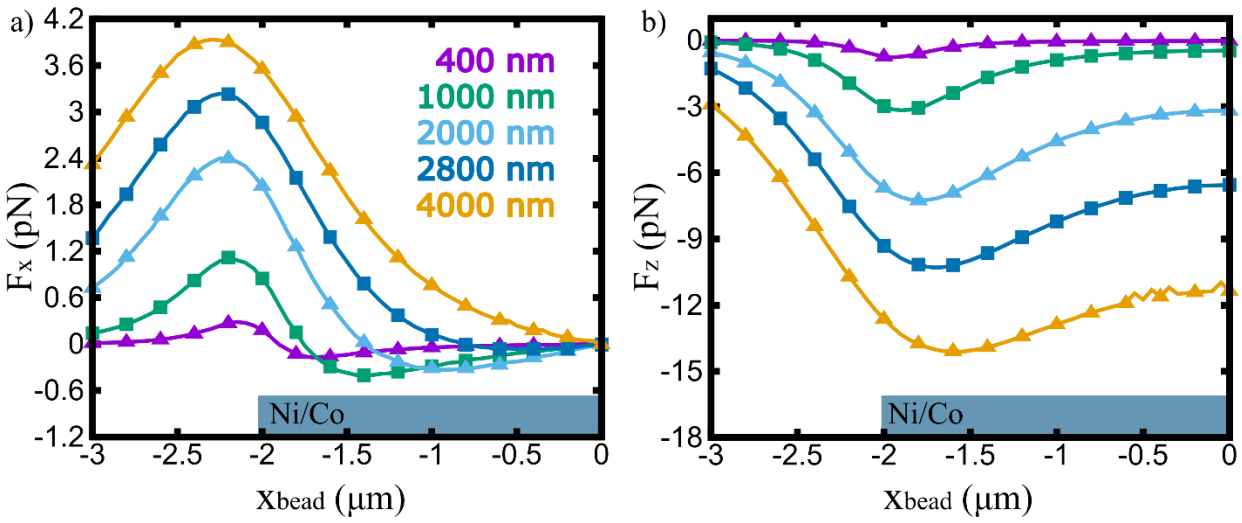

Figure 6.2 (a) The x-component of the force interactions between the a 4 μm Ni/Co disk positioned with the edge at $x_{bead} = -2\ \mu$m and centered at 0 μm for bead diameters varying between 400 nm and 4000 nm and **(b)** the corresponding z-components of force.

Figure 6.3a summarizes the effects of a changing disk diameter on the effects of the maximum force interaction. Here the maximum force value is found by taking the norm of all the force components, $F = \sqrt{F_x^2 + F_y^2 + F_z^2}$ at all x-positions and then finding the maximum value from

these values. In these simulations, the bead size was held fixed at 1 and 2 μm. The results indicate that the maximum force will be higher for the smaller disk diameters. As the disk size increases, the maximum interaction force will reach an asymptotic value. Thus, there is a limiting maximum force value between the Co/Ni disks and the magnetic beads. Higher forces are predicted when the bead size is larger, consistent with the results of the previous simulation. For increased force interactions, larger bead sizes may be desired. In these studies the gap was based on the constant polymer thickness to magnetic core ratio of 2:1. In the next set of simulations, the gap size was varied and the resulting maximum force variations are presented in Figure 6.3b. For this simulation, the Co/Ni disk was held fixed at 4 μm and the gap was varied. A similar trend is observed for the 1 μm and 2 μm bead, which indicates as the gap sizes increase, the maximum capture force decreases and tends towards an asymptotic value. Larger forces are again predicted for the larger beads. Thus, minimum gap sizes are desired and magnetic beads with a lower polymer thickness to magnetic core ratio may be considered for future implementation of strain-mediated multiferroic cell sorting applications.

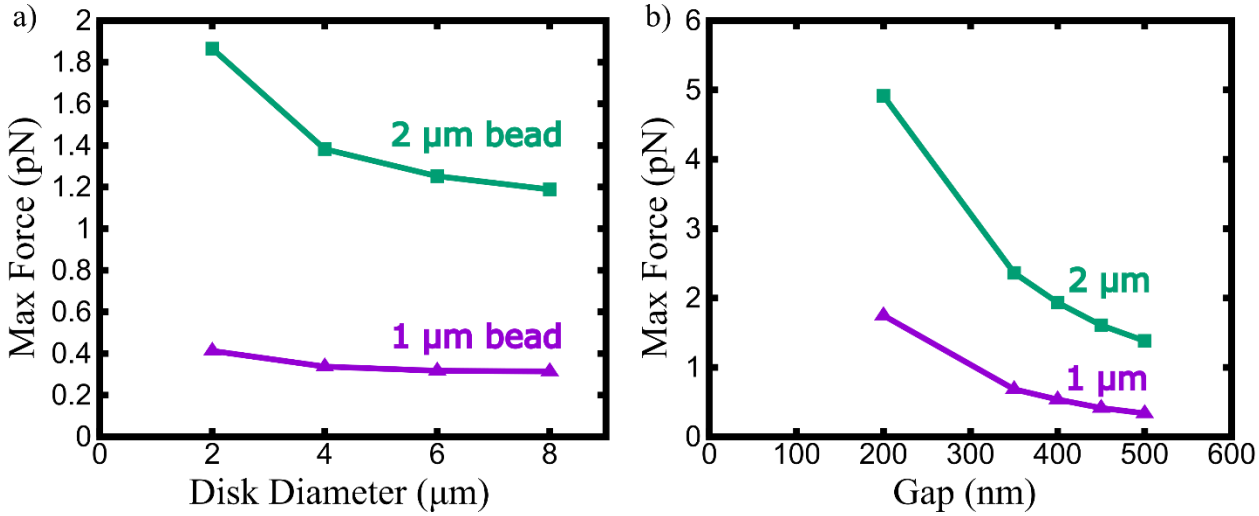

Figure 6.3 (a) Maximum Force vs Disk Diameter is plotted for 1 μm and 2 μm magnetic beads and **(b)** the maximum force vs the gap size is plotted for the same sized magnetic beads at a constant disk diameter of 4 μm.

In the last study, the effect of M_s and bead diameter were observed for the interaction force between the Co/Ni disk and the magnetic core. The results are shown in Figure 6.4. Here, the maximum value of the force magnitude, $\sqrt{F_x^2 + F_y^2 + F_z^2}$, was plotted for varying bead diameter and the five different M_s values. The results of these study show a small increase in the maximum capture force with increasing bead diameter for a constant M_s value. However, the maximum capture force increases significantly with increasing values of M_s. In fact, the capture force nearly doubles from 0.1 pN to 0.2 pN when the M_s value changes from 700 emu/cc to 1000 emu/cc for a constant bead diameter of 0.4 μm. This indicates it is beneficial to tune the M_s of the Co/Ni multilayers to be as high as possible to obtain the largest possible capture forces.

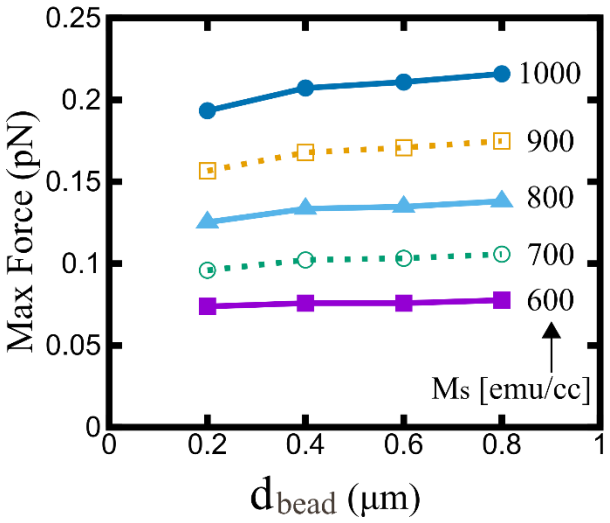

Figure 6.4 Maximum force vs the bead diameter for different M_s values.

These modeling results were used as a design tool for fabrication and testing of magnetic bead capture on Co/Ni multilayer disks. Since the models predicted highest capture forces with an increased M_s value, the fabricated Co/Ni films were created with an M_s of 800 emu/cc. To study a range of diameters, Co/Ni disks were fabricated with diameters of 4-7 μm. A variety of bead sizes were used for the microfluidic channel testing, including magnetic beads ranging from 200-2800 nm. Details of the fabrications and experimental steps are beyond the scope of this

dissertation as they were conducted in collaboration with other graduate students, Yu-Ching Hsiao and Reem Khojah, however experimental results are provided in Figure 6.5 to compare with modeling predictions made in this chapter. Figure 6.5a shows the fluorescent microscope image of magnetic beads captured on 7 μm Co/Ni multilayered disks. This image indicates that the beads preferentially stay along the perimeter of the disks as predicted by the models. Additionally, Figure 6.5b depicts a normalized intensity map providing numerical evidence of highest bead trapping along the edges of the disk.

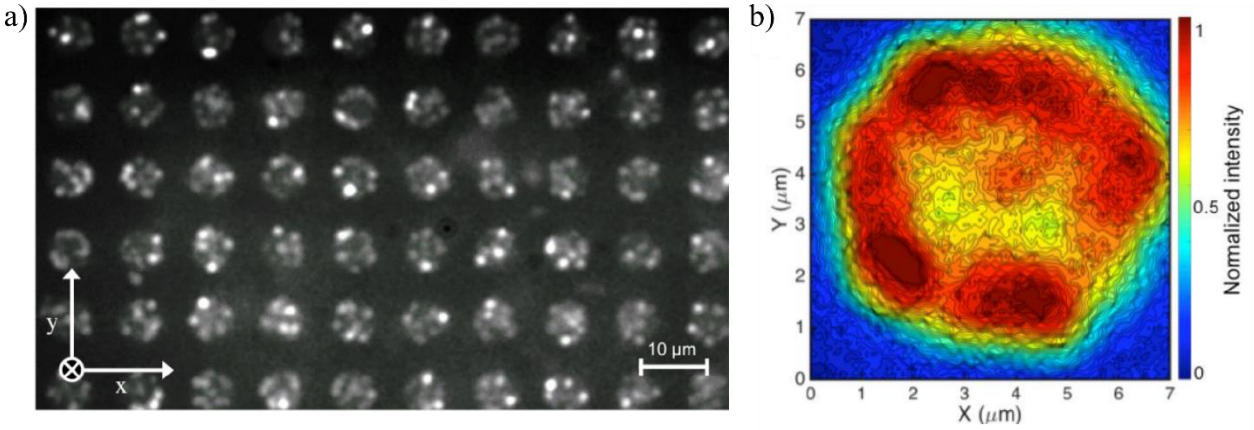

Figure 6.5 (a) Fluorescent microscope image of nanomagnetic capture and build-up on 7 µm Co/Ni multilayer disks. (b) Normalized intensity map of the image overlay shows high magnetic trapping region on the perimeter of Co/Ni multilayer disks[177].

6.4 Conclusion and Outlook

In this chapter, the force interactions of FeO_3 magnetic beads with a Ni/Co multilayer disk were simulated. Different parameters were varied to understand how geometry and material properties might affect these interactions to better understand the ability of this system to be integrated into a magnetic cell sorting devices. These simulations suggest the geometry of the disk and bead will affect the location of capture of the magnetic beads on the magnetic disk. When the ratio of the magnetic bead to the magnetic disk is smaller, the beads are likely to be captured along the

perimeter of the disk. However, as this ratio is increased, the magnetic beads are likely to be captured towards the center of the Co/Ni disk. The simulations predict a limiting force value when the bead size is held fixed and the disk diameter is increased. Additionally, simulation results indicate that stronger forces are expected for higher M_s values of the Co/Ni multilayer systems which can be adjusted by changing the thickness of the Co and Ni layers. This chapter serves as a stepping stone towards realizing the feasibility of magnetic cell sorting using multiferroic composite structures. Although this simplified model does not integrate the linear piezoelectric or ferroelectric equations used in the previous chapters, this model can be integrated with existing models to better understand the behavior of multiferroic structures for cell sorting applications. Past work by Li et al.[106] and Wang et al.[115] have demonstrated successful modeling of 180^o PMA switching behavior in strain-mediated composite structures. Integrating the 180^o switching model with the force model discussed in this chapter will allow for a better predictive tool of magnetic bead interactions with strain-mediated multiferroic structures. Since the experimental results are conducted in a microfluidic channel, an added refinement of this model will include drag forces from the fluid. These improvements to the model will help create a platform for better modeling strain-mediated multiferroic structures with PMA for cell capture and release.

VII. Conclusion

This dissertation has addressed some key issues for implementing future multiferroic cell sorting devices. Magnetic cell sorting is desirable for its simple and fast sorting mechanism but scaling magnetic cell sorting techniques has been a challenge due to the inability to control magnetism at the nanoscale. Multiferroic composite structures offer one potential solution for overcoming these scaling challenges. This work offered some potential solutions for integrating multiferroic structures to be used in cell sorting devices for a scalable sorting mechanism in the future.

In Chapter I, the motivation for multiferroic cell sorting capabilities was discussed. The research in current multiferroic composite structures and cell sorting technologies were reviewed. Some desired characteristics of cell sorting were addressed and current limitations of designing multiferroic structures for use in cell sorting were considered. Chapter II reviewed the key concepts for understanding the dynamics of magnetization in multiferroic composite structures. Additionally, the current state of the art modeling techniques used for multiferroic heterostructures were reviewed.

Chapter III of the dissertation introduced a new three ellipse design for implementing 360^{o} magnetization rotation for future cell sorting devices. This model employs magnetization dynamics to successfully switch a magnetic element 360^{o} using two voltage pulses. This design offers a simplified control mechanism and less intricate geometry over the currently available multiferroic devices which are capable of this similar magnetization rotation. However, the high strain values needed for the desired magnetization rotation cannot be achieved with linear piezoelectric materials and nonlinear ferroelectric materials must be considered for future fabrication of the device.

In Chapter IV, the sensitives of dynamic magnetization switching were analyzed. Since the dynamics of magnetization switching is a result of the input voltage, different voltage amplitudes and ramps were used to observe changes in a single domain magnetic ellipse. Results indicated that the small changes in the voltage magnitude change the time response of magnetization which ultimately affected the ballistic switching of the magnet. Additionally, the presence of defects in the structure were modelled demonstrating a resulting change in magnetization behavior which would affected the final magnetic configuration of the device.

Chapter V implements a new finite element model capable of capturing the nonlinear response of the substrate and corresponding effects on magnetization. Currently available modeling tools can only predict the magnetization dynamics of a single domain element on a linear substrate. In this chapter, an already developed phase-field model of polarization in a rhombohedral symmetry substrate was integrated with mechanics and micromagnetics. The results of the model demonstrated how the same input voltage can drastically change the magnetization response of the magnetic element which may be deposited on different domain configurations of the ferroelectric substrate. This model can be used to better understand why inhomogeneous magnetization switching is observed in magnetic elements patterned across a ferroelectric substrate and guide the design of future multiferroic cell sorting devices.

In Chapter VI, perpendicular magnetic anisotropy (PMA) was considered for cell capture in sorting devices. A simplified model was developed to understand the force interactions between the magnetic bead and Co/Ni multilayer disks with PMA. Results of these simulations indicated that the capture forces change with geometry and material properties for the disk and bead. These simulations demonstrated the highest trapping forces occurred along the perimeter of Co/Ni disks which were verified with microfluidic experiments matching this prediction.

The projects presented in this dissertation offer more insight on the future of multiferroic composites for use in cell sorting. Multiferroic cell sorting would be beneficial for use in more compact table top sorting devices. These ideas can also be extended to sorting of viruses and DNA chains, much smaller in size than cells, since multiferroic structures can be efficiently operated at the nanoscale. The work conducted herein offers a pathway towards novel diagnostic devices to be explored in the future.

Dissertation References

[1] L. A. Herzenberg, R. G. Sweet, L. A. Herzenberg, L. A. Herzenberg, R. G. Sweet, and L. A. Herzenberg, "Fluorescence-activated Cell Sorting," *Sci. Am.*, vol. 234, no. 3, pp. 108–118, 1976.

[2] C. Krista, "Kyoto Prize awarded to inventor of cell sorter," *Standford Report*, 2006. [Online]. Available: https://news.stanford.edu/news/2006/june14/med-herzenberg-061406.html.

[3] R. Tirouvanziam, C. J. Davidson, J. S. Lipsick, and L. A. Herzenberg, "Fluorescence-activated cell sorting (FACS) of Drosophila hemocytes reveals important functional similarities to mammalian leukocytes," *PNAS*, vol. 101, no. 0, 2004.

[4] L. A. Herzenberg, S. C. De Rosa, L. A. Herzenberg, L. Herzenberg, D. Rosa, and L. Herzenberg, "Monoclonal antibodies and the immunobiology and medicine," *Immunol. Today*, vol. 21, no. 8, pp. 383–390, 2000.

[5] L. A. Herzenberg, D. Parks, B. Sahaf, O. Perez, M. Roederer, and L. A. Herzenberg, "The History and Future of the Fluorescence Activated Cell Sorter and Flow Cytometry : A View from Stanford," *Clin. Chem.*, vol. 48, no. 10, pp. 1819–1827, 2002.

[6] C. W. S. Iv, D. Reyes, and G. P. López, "Microfluidic cell sorting: a review of the advances in the sepeartion of cells from debulking to rare cell isolation," *Lab a Chip*, vol. 15, pp. 1230–1249, 2015.

[7] D. Mattanovich and N. Borth, "Applications of cell sorting in biotechnology," *Microb. Cell Fact.*, vol. 11, pp. 1–11, 2006.

[8] W. A. Bonner, H. R. Hulett, R. . Sweet, and L. A. Herzenberg, “Fluorescence Activated Cell Sorting,” *Rev. Sci. Instrum.*, vol. 43, no. 3, 1972.

[9] D. R. Gossett *et al.*, “Label-free cell separation and sorting in microfluidic systems,” *Anal Bioanal Chem*, vol. 397, pp. 3249–3267, 2010.

[10] M. Piyasena and S. Graves, “The intersection of flow cytometry with microfluidics and microfabrication,” *Lab Chip*, vol. 14, pp. 1044–1059, 2014.

[11] A. Lenshof and T. Laurell, “From microfluidic application to nanofluidic phenomena issue Reviewing the latest advances in microfluidic and nanofluidic,” *Chem. Soc. Rev.*, vol. 39, pp. 1203–1217, 2010.

[12] A. Lenshof and T. Laurell, “Lab on a Chip Acoustofluidics 8 : Applications of acoustophoresis in continuous flow microsystems,” *Lab Chip*, vol. 12, pp. 1210–1223, 2012.

[13] M. A. Burguillos *et al.*, “Microchannel Acoustophoresis does not Impact Survival or Function of Microglia , Leukocytes or Tumor Cells,” *PLoS One*, vol. 8, no. 5, pp. 1–11, 2013.

[14] T. Laurell, F. Petersson, A. Nilsson, and F. Petersson, “Chip integrated strategies for acoustic separation and manipulation of cells and particles resulted in several national,” *Chem. Soc. Rev.*, vol. 36, pp. 492–506, 2007.

[15] S. Miltenyi, W. Muller, W. Weichel, and A. Radbruch, “High Gradient Magnetic Cell Separation With MACS,” *Cytometry*, vol. 11, pp. 231–238, 1990.

[16] N. Pamme and C. Wilhelm, “Continuous sorting of magnetic cells via on-chip free-flow

magnetophoresis," *Lab Chip*, vol. 6, pp. 974–980, 2006.

[17] N. Xia *et al.*, "Combined microfluidic-micromagnetic separation of living cells in continuous flow," *Biomed Microdevices*, vol. 8, pp. 299–308, 2006.

[18] J. J. Lai, K. E. Nelson, M. A. Nash, A. S. Hoffman, P. Yager, and P. S. Stayton, "Dynamic bioprocessing and microfludic transport control with smart magnetic nanoparticles in laminar-flow devices," *Lab Chip*, vol. 9, pp. 1997–2002, 2008.

[19] J. D. Adams, U. Kim, and H. T. Soh, "Multitarget magnetic activated cell sorter," *PNAS*, vol. 105, no. 47, pp. 18165–18170, 2008.

[20] C. Carr, M. Espy, P. Nath, S. L. Martin, M. D. Ward, and J. Martin, "Design , fabrication and demonstration of a magnetophoresis chamber with 25 output fractions," *J. Magn. Magn. Mater.*, vol. 321, pp. 1440–1445, 2009.

[21] E. A. Rapoport, "Magnetic Domain Walls for On-Chip Transport and Detection of Superparamagnetic Beads," Massachusetts Institute of Technology, 2014.

[22] K. Gunnarsson *et al.*, "Programmable Motion and Separation of Single Magnetic Particles on Patterned Magnetic Surfaces," *Adv. Mater.*, vol. 17, pp. 1730–1734, 2005.

[23] A. Chen, T. Byvank, G. B. Vieira, R. Sooryakumar, and A. Substrates, "Magnetic Microstructures for Control of Brownian Motion and Microparticle Transport," *IEEE Trans. Magn.*, vol. 49, no. 2, pp. 300–308, 2013.

[24] M. Donolato *et al.*, "Magnetic domain wall conduits for single cell applications," *L. a Chip*, vol. 11, pp. 2976–2983, 2011.

[25] E. Rapoport and G. S. D. Beach, "Transport dynamics of superparamagnetic microbeads

trapped by mobile magnetic domain walls," *Phys. Rev. B*, vol. 87, no. February, pp. 174426-1–9, 2013.

[26] E. Rapoport, D. Montana, and G. S. D. Beach, "Integrated capture, transport, and magneto-mechanical resonant sensing of superparamagnetic microbeads using magnetic domain walls," *Lab Chip*, vol. 12, pp. 4433–4440, 2012.

[27] E. Rapoport and G. Beach, "Magneto-mechanical resonance of a single superparamagnetic microbead trapped by a magnetic domain wall," *J. Appl. Phys.*, vol. 111, 2012.

[28] E. Rapoport and G. Beach, "Dynamics of superparamagnetic microbead transport along magnetic nanotracks by magnetic domain walls," *Appl. Phys. Lett.*, vol. 100, 2012.

[29] W. Eerenstein, N. D. Mathur, and J. F. Scott, "Multiferroic and magnetoelectric materials," *Nature*, vol. 442, no. August, pp. 759–765, 2006.

[30] D. N. Astrov, "Magnetoelectric Effect in Chromium Oxide," *Sov. Phys. JETP*, vol. 13, no. 4, 1961.

[31] C. W. Nan, M. I. Bichurin, S. Dong, D. Viehland, and G. Srinivasan, "Multiferroic magnetoelectric composites : Historical perspective , status , and future directions," *J. Appl. Phys.*, vol. 103, p. 031101 1-35, 2008.

[32] N. A. Hill, "Why Are There so Few Magnetic Ferroelectrics ?," *J. Phys. Chem. B*, vol. 104, pp. 6694–6709, 2000.

[33] T. Kimura, T. Goto, H. Shintani, K. Ishizaka, T. Arima, and Y. Tokura, "Magnetic control of ferroelectric polarization," *Nature*, vol. 426, pp. 55–58, 2003.

[34] J. Wang *et al.*, “Epitaxial BiFeO 3 Multiferroic Thin Film Heterostructures,” *Science (80-.).*, vol. 299, pp. 1719–1723, 2003.

[35] M. Fiebig, T. Lottermoser, D. Frohlich, A. V. Goltsev, and R. V. Pisarev, “Observation of coupled magnetic and electric domains,” *Nature*, vol. 419, pp. 818–820, 2002.

[36] N. Hur, S. Park, P. A. Sharma, J. S. Ahn, S. Guha, and S. Cheong, “Electric polarization reversal and memory in a multiferroic material induced by magnetic fields,” *Nature*, vol. 429, pp. 392–395, 2004.

[37] W. Prellier, M. P. Singh, and P. Murugavel, “The single-phase multiferroic oxides : from bulk to thin film,” *J. Phys. Condens. Matter*, vol. 17, pp. 803–832, 2005.

[38] J. Suchtelen, “Product Properties: A New Application of Composite Materials,” *Philips Res. Repts*, vol. 27, pp. 28–37, 1972.

[39] J. Curie and P. Curie, “Piezoelectric and allied phenomena in Rochelle Salt,” *Comput Rend Acad Sci Paris*, vol. 91, pp. 294–297, 1880.

[40] J. Van Den Boomgaard, A. M. J. G. Van Run, and J. Van Suchtelen, “Magnetoelectricity in piezoelectric- magnetostrictive composites,” *Ferroelectrics*, vol. 10, pp. 295–298, 1976.

[41] J. Van Den Boomgaard and R. A. Born, “A sintered magnetoelectric composite material BaTiO3-Ni (Co . Mn) Fe204,” *J. Mater. Sci.*, vol. 13, pp. 1538–1548, 1978.

[42] J. Van Den Boomgaard, D. R. Terrell, R. A. Born, and H. F. J. . Giller, “An in situ grown eutectic magnetoelectric composite material Part l Composition and unidirectional solidification,” *J. Magn. Magn. Mater.*, vol. 9, pp. 1705–1709, 1974.

[43] A. M. J. G. Run, D. R. Terrell, and J. H. Scholing, “An in situ grown eutectic

magnetoelectric composite material," *J. MAt*, vol. 9, pp. 1710–1714, 1974.

[44] Y. Zhou and F. G. Shin, "Magnetoelectric effect of mildly conducting magnetostrictive / piezoelectric particulate composites," *J. Appl. Phys.*, vol. 100, 2006.

[45] C. W. Nan and M. Li, "Calculations of giant magnetoelectric effects in ferroic composites of rare-earth – iron alloys and ferroelectric polymers," *Phys. Rev. B*, vol. 63, pp. 144415-1–9, 2001.

[46] C. W. Nan, M. Li, X. Feng, and S. Yu, "Possible giant magnetoelectric effect of ferromagnetic rare-earth-iron-alloys-filled ferroelectric polymers," *Appl. Phys. Lett.*, vol. 78, no. 17, 2001.

[47] J. Ryu, S. Priya, K. Uchino, and H. Kim, "Magnetoelectric Effect in Composites of Magnetostrictive and Piezoelectric Materials," pp. 107–119, 2002.

[48] J. Ryu, A. V. Carazo, K. Uchino, and H. Kim, "Magnetoelectric Properties in Piezoelectric and Magnetostrictive Laminate Composites," *Jpn. J. Appl. Phys.*, vol. 40, pp. 4948–4951, 2001.

[49] J. Ryu, S. Priya, A. V. Carazo, and K. Uchino, "Effect of the Magnetostrictive Layer on Magnetoelectric Properties in Lead Zirconate Titanate / Terfenol-D Laminate Composites," *J. Am. Ceram. Soc.*, vol. 84, no. 12, pp. 2905–2908, 2001.

[50] K. Mori and M. Wuttig, "Magnetoelectric coupling in Terfenol-D / polyvinylidenedifluoride composites," *Appl. Phys. Lett.*, vol. 81, pp. 100–101, 2010.

[51] J. Zhai, S. Dong, Z. Xiang, L. Li, and D. Viehland, "Giant magnetoelectric effect in Metglas / polyvinylidene-fluoride laminates," *Appl. Phys. Lett.*, vol. 89, 2006.

[52] S. Dong, J. Zhai, J. F. Li, D. Viehland, and M. I. Bichurin, “Magnetoelectric gyration effect in laminated composites at the electromechanical resonance,” *Appl. Phys. Lett.*, vol. 89, 2006.

[53] S. Dong, J. Zhai, J. Li, and D. Viehland, “Near-ideal magnetoelectricity in high-permeability magnetostrictive / piezofiber laminates with a (2-1) connectivity,” *Appl. Phys. Lett.*, vol. 89, 2006.

[54] W. Eerenstein, M. Wiora, J. L. Prieto, J. F. Scott, and N. D. Mathur, “Giant sharp and persistent converse magnetoelectric effects in multiferroic epitaxial heterostructures,” *Nat. Mater.*, vol. 6, 2007.

[55] C. Thiele, K. Dorr, O. Bilani, J. Rodel, and L. Schultz, “Influence of strain on the magnetization and magnetoelectric effect in La0.7A0.3MnO3/PMN-PT(001) (A=Sr,Ca),” *Phys. Rev. B*, vol. 75, 2007.

[56] B. M. Liu *et al.*, “Giant Electric Field Tuning of Magnetic Properties in Multiferroic Ferrite / Ferroelectric Heterostructures,” *Adv. Funct. Mater.*, vol. 19, pp. 1826–1831, 2009.

[57] J. J. Yang *et al.*, “Electric field manipulation of magnetization at room temperature in multiferroic CoFe2O4/Pb(Mg1/3Nb2/3)0.7Ti03.O3 heterostructures,” *Appl. Phys. Lett.*, vol. 94, 2009.

[58] A. Brandlmaier, S. Geprägs, M. Weiler, A. Boger, and M. Opel, “In situ manipulation of magnetic anisotropy in magnetite thin films,” *Phys. Rev. B*, vol. 77, 2008.

[59] N. Mathur, “A desirable wind up,” *Nature*, vol. 454, 2008.

[60] P. Borisov, A. Hochstrat, X. Chen, W. Kleemann, and C. Binek, “Magnetoelectric Switching of Exchange Bias,” *Phys. Rev. Lett.*, vol. 94, 2005.

[61] D. Hrabovsky *et al.*, “Electric-Field Control of Exchange Bias in Multiferroic Epitaxial Heterostructures,” *Phys. Rev. Lett.*, vol. 97, 2006.

[62] Y. Chu *et al.*, “Electric-field control of local ferromagnetism using a magnetoelectric multiferroic,” *Nat. Mater.*, vol. 7, 2008.

[63] H. Bea *et al.*, “Combining half-metals and multiferroics into epitaxial heterostructures for spintronics,” *Appl. Phys. A Mater. Sci. Process.*, vol. 88, 2006.

[64] E. Y. Tsymbal and H. Kohlstedt, “Tunneling Across a Ferroelectric,” *Science (80-.).*, vol. 313, no. July, pp. 181–184, 2006.

[65] M. Buzzi *et al.*, “Single domain spin manipulation by electric fields in strain coupled artificial multiferroic nanostructures,” *Phys. Rev. Lett.*, vol. 111, no. 2, pp. 1–5, 2013.

[66] J. Cui *et al.*, “A method to control magnetism in individual strain-mediated magnetoelectric islands A method to control magnetism in individual strain-mediated magnetoelectric islands,” *Appl. Phys. Lett.*, vol. 232905, no. 2013, 2013.

[67] J. L. Hockel, “Deterministic Magnetization Control by Magnetoelastic Anisotropy and its Dependence on Geometry and Scale,” University of California Los Angeles, 2013.

[68] C. Y. Liang *et al.*, “Modeling of magnetoelastic nanostructures with a fully coupled mechanical-micromagnetic model,” *Nanotechnology*, vol. 25, no. 43, 2014.

[69] C. Y. Liang *et al.*, “Electrical control of a single magnetoelastic domain structure on a clamped piezoelectric thin film - Analysis,” *J. Appl. Phys.*, vol. 116, no. 12, pp. 0–9, 2014.

[70] C. Nan, “Magnetoelectric effect in composites of piezeoelectric and piezomagnetic phases,” *Phys. Rev. B*, vol. 50, no. 9, 1994.

[71] C. Nan, G. Liu, and Y. Lin, “Magnetic-Field-Induced Electric Polarization in Multiferroic Nanostructures,” *Phys. Rev. Lett.*, vol. 94, 2005.

[72] V. M. Petrov, G. Srinivasan, M. I. Bichurin, and A. Gupta, “Theory of magnetoelectric effects in ferrite piezoelectric nanocomposites,” *Phys. Rev. B*, pp. 1–6, 2007.

[73] L. Chen, “Phase-Field Method of Phase Transitions/Domain Structures in Ferroelectric Thin Films: A Review,” *J. Am. Ceram. Soc.*, vol. 91, pp. 1835–1844, 2008.

[74] J. X. Zhang *et al.*, “Phase-field model for epitaxial ferroelectric and magnetic nanocomposite thin films,” *Appl. Phys. Lett.*, vol. 90, 2007.

[75] K. Yamauchi, S. Biplad, and S. Picozzi, “Interface effects at a half-metal / ferroelectric junction,” *Apllied Phys. Lett.*, vol. 91, 2010.

[76] M. K. Niranjan, J. P. Velev, C. Duan, S. S. Jaswal, and E. Y. Tsymbal, “Magnetoelectric effect at the Fe 3 O 4 / BaTiO 3 (001) interface : A first-principles study,” *Phys. Rev. B*, vol. 78, 2008.

[77] J. M. Rondinelli, M. Stengel, and N. A. Spaldin, “Carrier-mediated magnetoelectricity in complex oxide heterostructures,” *Nat. Nanotechnol.*, vol. 3, 2008.

[78] C. Duan *et al.*, “Surface Magnetoelectric Effect in Ferromagnetic Metal Films,” *Phys. Rev. Lett.*, vol. 101, 2008.

[79] C. Duan, C. Nan, S. S. Jaswal, and E. Y. Tsymbal, “Universality of the surface magnetoelectric effect in half-metals,” *Phys. Rev. B*, vol. 79, 2009.

[80] N. A. Pertsev, “Giant magnetoelectric effect via strain-induced spin reorientation transitions in ferromagnetic films,” *Phys. Rev. B*, vol. 78, 2008.

[81] A. Lisfi *et al.*, “Reorientation of magnetic anisotropy in epitaxial cobalt ferrite thin films,” *Phys. Rev. B*, vol. 76, 2007.

[82] I. Gilbert *et al.*, “Magnetic microscopy and simulation of strain-mediated control of magnetization in PMN-PT / Ni nanostructures,” *Appl. Phys. Lett.*, vol. 162404, no. 2016, pp. 0–5, 2016.

[83] A. A. Kundu, A. C. Chavez, S. M. Keller, G. P. Carman, and C. S. Lynch, “360° Deterministic Magnetization Rotation in a Three-Ellipse Magnetoelectric Heterostructure,” *J. Appl. Phys.*, vol. 123, no. 10, 2018.

[84] H. Sohn *et al.*, “Electrically driven magnetic domain wall rotation in multiferroic heterostructures to manipulate suspended on-chip magnetic particles,” *ACS Nano*, vol. 9, no. 5, pp. 4814–4826, 2015.

[85] Z. Xiao, R. Khojah, M. Chooljian, R. Lo Conte, and J. D. Schneider, “Cytocompatible magnetostrictive microstructures for nano- and microparticle manipulation on linear strain response piezoelectrics Cytocompatible magnetostrictive microstructures for nano- and microparticle manipulation on linear strain response piezoelect,” *Multifunct. Mater.*, vol. 1, 2018.

[86] G. P. Carman, N. Sun, and G. Editors, “Strain-mediated magnetoelectrics : Turning science fiction into reality,” *MRS Bulletin*, pp. 822–828, 2018.

[87] J. Domann, T. Wu, T. K. Chung, and G. Carman, “Strain-mediated magnetoelectric

storage , transmission , and processing : Putting the squeeze on data," *MRS Bulletin*, no. November, 2018.

[88] J. P. Domann and G. P. Carman, "Strain powered antennas," *J. Appl. Phys.*, vol. 121, 2017.

[89] D. Massimiliano, "Nonlinear Magnetization Dynamics in Thin-Films and Nanoparticles," University of Napoli, 2004.

[90] R. C. O'Handley, *Modern magnetic materials*. Wiley, 2000.

[91] S. Chikazumi, *Physics of Magnetism*. John Wiley & Sons, Inc., 1964.

[92] X. Li, "Nanomagnet Applications in Multiferroic Heterostructures," University of California, Los Angeles, 2017.

[93] W. F. Brown, "Thermal Fluctuations of Fine Ferromagnetic Particles," *IEEE Trans. Magn.*, vol. 15, no. 5, pp. 1196–1208, 1979.

[94] L. D. Landau and E. M. Lifshitz, "On the theory of the dispersio nof magnetic permeability in ferromagnetic bodies," *Phys. Z. Sowaj.*, vol. 8, 1935.

[95] T. L. Gilbert, "A Lagrangian formulation of the gyromagnetic equation of the magnetization field," *Phys. Rev.*, vol. 100, 1955.

[96] Q. H. Qin, *Advanced Mechanics of Piezoelectricity*. Springer Science & Business Media, 2013.

[97] Moheimani and Fleming, *Piezoelectric Transducers for Vibration Control & Damping*. .

[98] C. Liang *et al.*, "Strain-mediated deterministic control of 360 domain wall motion in

magnetoelastic nanorings," *J. Appl. Phys.*, vol. 174101, no. 2015, 2015.

[99] J. J. Wang, J. M. Hu, J. Ma, J. X. Zhang, L. Q. Chen, and C. W. Nan, "Full 180° magnetization reversal with electric fields.," *Sci. Rep.*, vol. 4, p. 7507, 2014.

[100] S. Cherepov *et al.*, "Electric-field-induced spin wave generation using multiferroic magnetoelectric cells," *Phys. Rev. Lett.*, vol. 082403, no. 2014, 2014.

[101] J. Hu *et al.*, "Electric-field control of strain-mediated magnetoelectric random access memory," *J. Appl. Phys.*, vol. 093912, no. 2010, pp. 0–10, 2010.

[102] K. Roy, S. Bandyopadhyay, and J. Atulasimha, "Hybrid spintronics and straintronics : A magnetic technology for ultra low energy computing and signal processing," *Appl. Phys. Lett.*, vol. 063108, no. 2011, pp. 97–100, 2011.

[103] M. Buzzi *et al.*, "Single Domain Spin Manipulation by Electric Fields in Strain Coupled Artificial Multiferroic Nanostructures," *Phys. Rev. Lett.*, vol. 027204, no. July, pp. 1–5, 2013.

[104] J. Cui, S. M. Keller, C. Liang, and G. P. Carman, "Nanoscale magnetic ratchets based on shape anisotropy," *Nanotechnology*, 2017.

[105] A. K. Biswas, H. Ahmad, J. Atulasimha, and S. Bandyopadhyay, "Experimental Demonstration of Complete 180 ° Reversal of Magnetization in Isolated Co Nanomagnets on a PMN − PT Substrate with Voltage Generated Strain," *NanoLetters*, vol. 17, no. 2017, pp. 1–7, 2017.

[106] X. Li *et al.*, "Strain-mediated 180o perpendicular magnetization switching of a single domain multiferroic structure," *J. Appl. Phys.*, vol. 014101, no. 2015, 2015.

[107] R.-C. Peng, J.-M. Hu, K. Momeni, J.-J. Wang, L.-Q. Chen, and C.-W. Nan, “Fast 180° magnetization switching in a strain-mediated multiferroic heterostructure driven by a voltage,” *Sci. Rep.*, vol. 6, no. February, p. 27561, 2016.

[108] C. Liang, S. M. Keller, A. E. Sepulveda, and A. Bur, “Modeling of magnetoelastic nanostructures with a fully coupled mechanical- micromagnetic model,” *J. Appl. Phys.*, 2014.

[109] S. Zhang *et al.*, “Electric-Field Control of Nonvolatile Magnetization in Co4Fe40B20/Pb(Mg1/3Nb2/3)0.7Ti0.3O3 Structure at Room Temperature,” *Phys. Rev. Lett.*, vol. 137203, no. March, pp. 1–5, 2012.

[110] S. Ikeda *et al.*, “A perpendicular-anisotropy CoFeB – MgO magnetic tunnel junction,” *Nat. Mater.*, vol. 9, no. 9, pp. 721–724, 2010.

[111] C. S. Desai and T. Kundu, *Introductory to Finite Element*. CRC Press, 2001.

[112] L. Leem, J. S. Harris, L. Leem, and J. S. Harris, “Magnetic coupled spin-torque devices for nonvolatile logic applications Magnetic coupled spin-torque devices for nonvolatile logic applications,” *J. Appl. Phys.*, vol. 105, no. 2009, 2009.

[113] L. E. Ocola and A. Stein, “Effect of cold development on improvement in electron-beam nanopatterning resolution and line roughness,” *J. Vac. Sci. Technol. B Microelectron. Nanom. Struct. Process. Meas. Phenom.*, vol. 3061, no. 2006, 2006.

[114] W. W. Hu, K. Sarveswaran, M. Lieberman, G. H. Bernstein, and W. W. Hu, “Sub-10 nm electron beam lithography using cold development of poly(methylmethacrylate),” *J. Vac. Sci. Technol. B Microelectron. Nanom. Struct. Process. Meas. Phenom.*, vol. 1711, no.

2004, 2004.

[115] Q. Wang *et al.*, “Strain-mediated 180 switching in CoFeB and Terfenol-D nanodots with perpendicular magnetic anisotropy,” *Appl. Phys. Lett.*, vol. 102903, no. 110, pp. 1–6, 2017.

[116] J. Hu *et al.*, “Purely Electric-Field-Driven Perpendicular Magnetization Reversal,” *NanoLetters*, vol. 15, no. 2015, pp. 616–622, 2015.

[117] H. Sohn *et al.*, “Electrically Driven Wall Magnetic Domain Wall Rotation in Multiferroic Heterostructures to Manipulate Suspended On-Chip Magnetic Particles,” *ACS Nano*, vol. 9, no. 5, pp. 4814–4826, 2015.

[118] S. Iihama, S. Mizukami, H. Naganuma, M. Oogane, Y. Ando, and T. Miyazaki, “Gilbert damping constants of Ta / CoFeB / MgO (Ta) thin films measured by optical detection of precessional magnetization dynamics,” *Phys. Rev. B - Condens. Matter Mater. Phys.*, vol. 174416, no. 89, pp. 1–6, 2014.

[119] H. Lee, L. Wen, M. Haertinger, and C. H. Back, “Magnetic Damping in Ferromagnetic Thin Films,” *Jpn. J. Appl. Phys.*, vol. 3889, no. 45, pp. 3–6, 2006.

[120] G. Malinowski, K. C. Kuiper, R. Lavrijsen, H. J. M. Swagten, and B. Koopmans, “Magnetization dynamics and Gilbert damping in ultrathin Co 48 Fe 32 B 20 films with out-of-plane anisotropy,” *Appl. Phys. Lett.*, vol. 102501, no. 94, 2013.

[121] G. A. Lebedev, B. Viala, T. Lafont, D. I. Zakharov, O. Cugat, and J. Delamare, “Converse magnetoelectric effect dependence with CoFeB composition in ferromagnetic / piezoelectric composites,” *J. Appl. Phys.*, vol. 07C725, no. 111, 2012.

[122] T. Lafont, L. Gimeno, J. Delamare, and G. A. Lebedev, “Magnetostrictive – piezoelectric composite strucures for energy harvesting,” *J. Micromechanics Microengineering*, vol. 094009, no. 22, 2012.

[123] M. J. Madou, *Fundamentals of microfabrication: the science of miniturization.* CRC Press, 2002.

[124] G. S. Abo, Y. Hong, J. Park, J. Lee, W. Lee, and B. Choi, “Definition of Magnetic Exchange Length,” *IEEE Trans. Magn.*, vol. 49, no. 8, pp. 4937–4939, 2013.

[125] T. A. Ostler, R. Cuadrado, R. W. Chantrell, A. W. Rushforth, and S. A. Cavill, “Strain Induced Vortex Core Switching in Planar Magnetostrictive Nanostructures,” *Phys. Rev. Lett.*, vol. 067202, no. August, pp. 1–5, 2015.

[126] J. T. Heron *et al.*, “Deterministic switching of ferromagnetism at room temperature using an electric field,” *Nature*, vol. 516, no. 2014, 2014.

[127] J. Hu, Z. Li, L. Chen, and C. Nan, “High-density magnetoresistive random access memory operating at ultralow voltage at room temperature,” *Nat. Commun.*, vol. 2, no. November, pp. 553–558, 2011.

[128] H. Sohn, “Deterministic control of magnetism by the mutlferroric magnetoelastic effect at the nano and macro-scale,” UCLA, 2017.

[129] Y. Nakatani, A. Thiaville, and J. Miltat, “Faster magnetic walls in rough wires,” *Nat. Mater.*, vol. 2, pp. 521–523, 2003.

[130] J. Leliaert, B. Van De Wiele, A. Vansteenkiste, L. Laurson, G. Durin, and L. Dupr, “Influence of material defects on current-driven vortex domain wall mobility,” *Phys. Rev.*

B, vol. 064419, no. 89, pp. 1–5, 2014.

[131] J. Leliaert, A. Vansteenkiste, L. Laurson, G. Durin, and B. Van Waeyenberge, "A numerical approach to incorporate intrinsic material defects in micromagnetic A numerical approach to incorporate intrinsic material defects in micromagnetic simulations," *J. Appl. Phys.*, vol. 102, no. 115, 2014.

[132] K. M. Krishnan, *Fundamentals and Applications of Magnetic Materials*, First Edit. Oxford University Press, 2016.

[133] A. C. Chavez, "Voltage Control of Magnetism in Nanoscale Artificial Multiferroics," University of California, Los Angeles, 2018.

[134] K. Roy, S. Bandyopadhyay, and J. Atulasimha, "Hybrid spintronics and straintronics : A magnetic technology for ultra low energy computing and signal processing," *Appl. Phys. Lett.*, vol. 99, 2011.

[135] K. Roy, S. Bandyopadhyay, and J. Atulasimha, "Switching dynamics of a magnetostrictive single-domain nanomagnet subjected to stress," *Phys. Rev. B - Condens. Matter Mater. Phys.*, vol. 83, no. 22, pp. 1–15, 2011.

[136] N. D'Souza, J. Atulasimha, and S. Bandyopadhyay, "Four-state nanomagnetic logic using multiferroics," *J. Phys. D Appl. Phys*, vol. 44, pp. 265001–7, 2011.

[137] J. Cui *et al.*, "A method to control magnetism in individual strain-mediated magnetoelectric islands," *Appl. Phys. Lett.*, vol. 103, no. 23, 2013.

[138] J. Ryu, S. Priya, K. Uchino, and H. E. Kim, "Magnetoelectric effect in composites of magnetostrictive and piezoelectric materials," *J. Electroceramics*, vol. 8, no. 2, pp. 107–

119, 2002.

[139] K. P. Wetzlar, “Leveraging Anisotropy to Enhance Multiferroic Tansduction,” UCLA, 2015.

[140] R. Lo Conte *et al.*, “Influence of Nonuniform Micron-Scale Strain Distributions on the Electrical Reorientation of Magnetic Microstructures in a Composite Multiferroic Heterostructure,” *Nano Lett.*, vol. 18, no. 3, pp. 1952–1961, 2018.

[141] W. Dong, “Characterization , Modeling , and Energy Harvesting of Phase Transformations in Ferroelectric Materials,” UCLA, 2015.

[142] J. A. Gallagher, “Field-Induced Phase Transformations in Relaxor Ferroelectric Single Crystals,” UCLA, 2014.

[143] Y. L. Li, S. Y. Hu, and L. Q. Chen, “Ferroelectric domain morphologies of (001) PbZr 1 − x Ti x O 3 epitaxial thin films,” *J. Appl. Phys.*, vol. 97, no. 034112, pp. 1–7, 2005.

[144] J. X. Zhang *et al.*, “Three-dimensional phase-field simulation of domain structures in ferroelectric islands Three-dimensional phase-field simulation of domain structures in ferroelectric islands,” vol. 122906, pp. 2006–2009, 2008.

[145] Y. L. Li and L. Q. Chen, “Temperature-strain phase diagram for BaTiO3 thin films,” *Appl. Phys. Lett.*, vol. 88, no. 072905, pp. 1–3, 2006.

[146] Y. Tong *et al.*, “The effect of strain on the domain switching of ferroelectric polycrystals,” *J. Appl. Phys.*, vol. 074102, no. 117, 2015.

[147] J. X. Zhang and L. Q. Chen, “Phase-field model for ferromagnetic shape- memory alloys,” *Philos. Mag. Lett.*, vol. 85, no. 10, pp. 533–541, 2005.

[148] J. Hu, G. Sheng, J. X. Zhang, C. W. Nan, and L. Q. Chen, “Phase-field simulation of strain-induced domain switching in magnetic thin films,” *Appl. Phys. Lett.*, vol. 98, no. 112505, pp. 2–5, 2011.

[149] J. M. Hu and C. W. Nan, “Electric-field-induced magnetic easy-axis reorientation in ferromagnetic/ferroelectric layered heterostructures,” *Phys. Rev. B - Condens. Matter Mater. Phys.*, vol. 80, no. 22, pp. 1–11, 2009.

[150] J. Hu, G. Sheng, J. X. Zhang, C. W. Nan, and L. Q. Chen, “Phase-field simulation of electric-field-induced in-plane magnetic domain switching in magnetic / ferroelectric layered heterostructures,” *J. Appl. Phys.*, vol. 109, no. 123917, pp. 1–6, 2011.

[151] C. G. Zhong, X. M. Ji, Y. L. Zhao, P. X. Zhou, H. X. Cao, and Z. C. Dong, “Electric field induced magnetization of multiferroic horizontal heterostructures,” *J. Appl. Phys.*, vol. 108, no. 8, 2010.

[152] J. J. Wang *et al.*, “Effect of strain on voltage-controlled magnetism in BiFeO 3 -based heterostructures,” *Sci. Rep.*, vol. 4:4553, no. 10:1038, pp. 1–6, 2014.

[153] J. Hu *et al.*, “Voltage-driven perpendicular magnetic domain switching in multiferroic nanoislands,” *J. Appl. Phys.*, vol. 194301, no. 113, 2013.

[154] X. Li *et al.*, “Strain-mediated 180° perpendicular magnetization switching of a single domain multiferroic structure,” *J. Appl. Phys.*, vol. 118, no. 1, 2015.

[155] J. Cui, S. M. Keller, C. Liang, G. P. Carman, and C. S. Lynch, “Nanoscale magnetic ratchets based on shape anisotropy,” *Nanotechnology*, vol. 28, no. 08LT01, pp. 1–8, 2017.

[156] Z. Xiao *et al.*, “Bi-directional coupling in strain-mediated multiferroic heterostructures

with magnetic domains and domain wall motion," *Sci. Rep.*, vol. 8, no. 1, pp. 1–10, 2018.

[157] P. Lv, L. Wang, and C. S. Lynch, "A phenomenological thermodynamic energy function for PIN-PMN-PT relaxor ferroelectric single crystals," *Acta Mater.*, vol. 137, pp. 93–102, 2017.

[158] P. Lv and C. S. Lynch, "Phase- field simulation of domain walls in rhombohedral ferroelectric single crystals," *Acta Mater.*, vol. 155, pp. 245–252, 2018.

[159] E. Sun and W. Cao, "Relaxor-based ferroelectric single crystals: Growth, domain engineering, characterization and applications," *Prog. Mater. Sci.*, vol. 65, pp. 124–210, 2014.

[160] T. Kundu, *Fundamentals of Fracture Mechanics*, 1st Editio. Boca Raton: Taylor & Francis Group, 2008.

[161] J. Walowski, M. D. Kaufmann, B. Lenk, C. Hamann, J. McCord, and M. Münzenberg, "Intrinsic and non-local Gilbert damping in polycrystalline nickel studied by Ti : SSSapphire laser fs spectroscopy," *J. Phys. D. Appl. Phys.*, vol. 41, no. 16, 2008.

[162] E. Sun, S. Zhang, J. Luo, T. R. Shrout, and W. Cao, "Elastic , dielectric , and piezoelectric constants of Pb(In1/2Nb1/2)O3-Pb(Mg1/3Nb2/3)O3-PbTiO3 single crystal poled along [011]," *Appl. Phys. Lett.*, vol. 97, no. 032902, pp. 1–3, 2010.

[163] Z. Xiao *et al.*, "Enhanced magnetoelectric coupling in a composite multiferroic system via interposing a thin film polymer," *AIP Adv.*, vol. 8, no. 5, 2018.

[164] H. Wu, J. Zhu, Y. Huang, D. Wu, and J. Sun, "Microfluidic-Based Single-Cell Study: Current Status and Future Perspective," *Molecules*, vol. 23, no. 2347, 2018.

[165] T. B. Christensen, K. Smistrup, A. Wolff, M. F. Hansen, and M. Bu, “Characterization of a microfluidic magnetic bead separator for high-throughput applications,” *Sensors Actuators A Phys.*, vol. 145–146, pp. 430–436, 2007.

[166] O. Osman *et al.*, “Microfluidic immunomagnetic cell separation using integrated permanent micromagnets,” *Biomicrofluidics*, vol. 7, no. 5, 2013.

[167] F. Y. Yang *et al.*, “Manipulation of Magnetically Labeled and Unlabeled Cells with Mobile Magnetic Traps,” *Biophys. J.*, vol. 98, no. 3, pp. 412–417, 2010.

[168] N. Minc *et al.*, “Microfluidic sorting and multimodal typing of cancer cells in self-assembled magnetic arrays,” *Proc. Natl. Acad. Sci.*, vol. 107, no. 33, pp. 14524–14529, 2010.

[169] J. Pivetal *et al.*, “Micro-magnet arrays for specific single bacterial cell positioning,” *J. Magn. Magn. Mater.*, vol. 380, pp. 72–77, 2015.

[170] G. Bochi *et al.*, “Perpendicular magnetic anisotropy, domains, and misfit strain in epitaxial Ni/CuNi/Cu/Si(001) thin films,” *Phys. Rev. B*, vol. 52, no. 10, 1995.

[171] J. M. L. Beaujour, W. Chen, K. Krycka, C. C. Kao, J. Z. Sun, and A. D. Kent, “Ferromagnetic resonance study of sputtered Co|Ni multilayers,” *Eur. Phys. J. B*, vol. 59, no. 4, pp. 475–483, 2007.

[172] R. Sbiaa, H. Meng, and S. N. Piramanayagam, “Materials with perpendicular magnetic anisotropy for magnetic random access memory,” *Phys. Status Solidi - Rapid Res. Lett.*, vol. 5, no. 12, pp. 413–419, 2011.

[173] M. Johnson, P. Bloemen, F. den Broeder, and J. de Vries, “Magnetic anisotropy in

metallic multilayers," *Rep. Prog. Phys.*, vol. 59, pp. 1409–1458, 1996.

[174] R. Hawig, E. F. K. Member, and R. Hawig, "The Exchange-Spring Magnet:," *IEEE Trans. Magn.*, vol. 27, no. 4, pp. 3588–3600, 1991.

[175] J. Crangle and G. M. Goodman, "The Magnetization of Pure Iron and Nickel," *Proc. R. Soc. A Math. Phys. Eng. Sci.*, vol. 321, pp. 477–491, 1971.

[176] H. Suzuki, "Development of a Chaotic Micro-Mixer Using Magnetic Beads," University of California, Los Angeles, 2003.

[177] Y. Hsiao *et al.*, "Capturing Magnetic Bead-based Arrays Using Perpendicular Magnetic Anisotropy (PMA)," Under review.